Experimental and Theoretical Studies of Highly-Excited Diatomic Molecules at a Wide Range of Internuclear Distances

by

Jeffrey N. Philippson

A thesis submitted to the
Department of Physics, Engineering Physics and Astronomy
in conformity with the requirements for
the degree of Doctor of Philosophy

Queen's University
Kingston, Ontario, Canada
January 2012

Abstract

Experimental and theoretical investigations of highly-excited molecules are presented that advance the current state of knowledge of intramolecular interactions in highly-excited molecular states.

A quantitative analysis of intramolecular interactions in excited hydrogen fluoride is presented, in which the rotational levels of the $B\,^1\Sigma^+$, $v = 29$ vibronic level are shown to mix with the corresponding e-parity components of the $C\,^1\Pi$, $v = 0$ level. Extrapolating the experimentally-derived mixing parameter to the unperturbed limit reveals an unperturbed value of the a_F hyperfine parameter of 4132(25) MHz.

Coupling energies between the ion-pair curve and long-range asymptotes of covalent states are calculated for a large number of alkali–alkali collision channels, revealing the dependence on the internuclear distance at which the crossing takes place and forming a foundational step for the calculation of cross-sections and rate coefficients for different charge-exchange and other processes.

To advance the experimental investigation of these systems, optical instrumentation and associated control systems have been designed and constructed for cooling and trapping lithium in preparation for experimental studies of cold-collisions that will be informed by, and ultimately a test of, some of these calculated ionic–covalent coupling energies. A novel scheme for systematic optimization of peak-locking has

been developed and implemented, providing a rigorous assessment of the optimal experimental parameters. A side-of-filter offset-locking scheme was implemented, characterizing and correcting for a previously unexplained offset in the error-signal.

A novel calibrated polarimetry scheme is demonstrated, correcting for the primary sources of uncertainty relating to manufacturing tolerances and experimental errors. The calibrated set of polarization measurements is used to examine the purity of the optical polarization state in the light sources to be used for trapping lithium.

Acknowledgments

All of the research presented herein was undertaken in the Optical Physics Group at Trent University under the guidance of Prof. Ralph Shiell, whose knowledge and enthusiasm have been a driving force behind my development as a physicist. I shall be eternally grateful for the breadth and depth of knowledge and understanding you passed on to me in many areas of physics and experimental techniques, and for showing me the joy of scientific enquiry.

Experimental physics is a collaborative undertaking and the research presented in this thesis is no exception. Particular thanks are due to Prof. Wim Ubachs and Elmar Reinhold at the Laser Centre of the Vrije Universiteit in Amsterdam, The Netherlands, for obtaining the high-quality spectra on which the analysis in chapter 3 is based, in addition to further discussions and assistance in the preparation of the associated publication. Prof. William van Wijngaarden of York University provided invaluable advice on alkali Rydberg-state wave functions used in the calculations of ionic–covalent coupling energies presented in chapter 4 in addition to generously loaning a tapered amplifier controller and other research equipment. The calculations in chapter 4 build on earlier work by Robert Collister, a fellow graduate student in the Optical Physics Group at Trent University. The assembly and optimization of the experimental apparatus described in chapter 6 included collaborative work with

fellow graduate students, Robert Collister, Matthew Romerein and Lisa Ugray. The polarization measurement and control project descibed in chapter 7 was a joint project with Matthew Romerein, extending previous work by Prof. Robert L. Brooks of the University of Guelph.

Additional thanks are due to Dr. Frederik Fatemi of the US Naval Research Laboratory and Klaus Bescherer of Queen's University for invaluable information on the use of single-mode optical fibers, Samuel Pollock of Imperial College, London for helpful discussions on the topic of laser frequency offset locking, and Prof. Dennis Tokaryk of the University of New Brunswick for stimulating discussions on the minutiae of diatomic molecular spectroscopy.

I wish to thank Prof. James Fraser of Queen's University for his assistance in matters large and small during my time in Kingston and for remaining an important point of contact during my time at Trent.

My time as a researcher at Trent has been made immeasurably better through my interactions with the faculty, staff, graduate students and undergraduate researchers of the Department of Physics and Astronomy at Trent University.

Last but not least, I would like to to thank my partner April Steele for all her love, support and encouragement during the completion of this work. Your confidence in me kept me motivated and inspired throughout this long journey.

Publications

The following publications are based on material from this thesis:

Chapter 3

Observation of molecular hyperfine structure in the extreme ultraviolet: The HF C–X spectrum
J. N. Philippson, R. C. Shiell, E. Reinhold and W. Ubachs
Journal of Chemical Physics **129** (17) 174310 [6 pages] (2008)

Chapter 7

A calibrated rotating quarter-wave plate method for determining polarization over a wide range of wavelengths
M. Romerein, **J. N. Philippson** and R. C. Shiell
Applied Optics **50** (28) 5382–5389 (2011)

Table of Contents

List of Tables

List of Figures

Chapter 1

Introduction

The intersection of atomic and molecular physics provides fertile territory for studying the dynamics and interactions of quantum systems. The remarkable level of control afforded by the techniques of atomic physics, combined with the range of possible interactions within and between molecules is helping to overcome some of the limitations historically associated with each sub-field. In particular these include the limited range of interactions between essentially spherical atoms, and the difficulty of precisely controlling the internal quantum states of molecules.

The potential of ultracold atoms to open up completely new areas of physics was demonstrated with the realization of Bose–Einstein condensation in ultracold sodium [1] and lithium [2], commencing a decade of discovery touching on some of the great unanswered questions in physics. Bose-Einstein condensates in an optical lattice have been used to simulate many-body phenomena familiar to condensed-matter physicists, such as the superconductor-Mott insulator transition [3], while application of the same cooling techniques to fermionic species have yielded experimental demonstrations of the Fermi-pressure required to satisfy the Pauli-exclusion principle [4].

Such advances are now being extended into the realm of molecular physics with the realization of ultracold molecules through the photoassociation of laser-cooled atoms [5], giving rise to the novel field of ultracold chemistry [6].

As exciting as these developments are, they have tended to remain focused on ground-state interactions. This trend has left open significant opportunities for discovery in the study of highly-excited molecules, treating the intramolecular interactions as a tool through which insight into the underlying physics can be obtained.

1.1 Research goals

The primary goal of the research undertaken for this thesis is to obtain insight into the properties and interactions of highly-excited diatomic molecules, with particular emphasis placed on ionic molecular states of the form $A^+\cdots B^-$ (ion-pairs) with their long-range attractive potential and relatively simple structure.

Much of the work is focused on lithium, which, while somewhat challenging to work with experimentally due to its highly-reactive nature and low vapour pressure, is a light atom amenable to theoretical calculations, has a laser-cooling transition accessible to available diode-laser systems, and has transitions to molecular Rydberg-states in the near-UV accessible to conventional dye-laser systems. Figure 1.1 illustrates the relationships between the atomic energy levels of Li and the potential energy curves of various states of Li_2, while also showcasing some of the many interesting features available for study.

A key experimental goal is the development and optimization of instrumentation and procedures for the laser-cooling of ^{7}Li. A stable source of laser-cooled atoms at $\sim$300 μK, trapped at densities approaching 10^{10} cm^{-3} [9] will provide an ideal

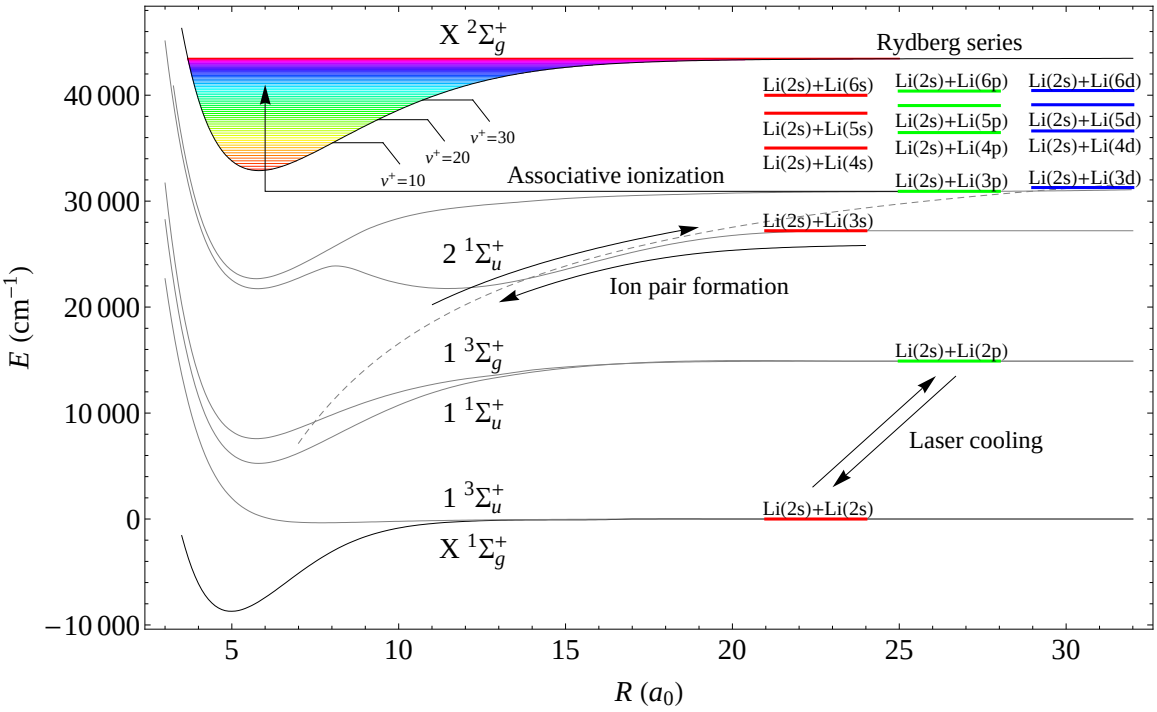

Figure 1.1: Some Li_2 potential-energy curves together with atomic asymptotes of such curves. An illustration of the many features of interest in the simple Li+Li system: including laser-cooling on the 2s→2p transition, example collisional ion-pair formation from the 2s+3s channel, example associative ionization forming Li_2^+ from the 2s+3p channel, and the Rydberg atomic and molecular states. The horizontal positions of the atomic levels are unrelated to the internuclear distance (R) axis [7, 8].

controlled setting for future high-resolution spectroscopy and dynamics experiments.

A particular class of intended experiments, the efficient collisional formation of ion-pairs, depends on finding those inbound atomic collision channels that couple optimally to the ion-pair curve, represented by the dashed line in figure 1.1. In preparation for such experiments, off-diagonal matrix elements between the ion-pair curve and the atomic asymptotes have been calculated for Li_2 and other alkali-alkali dimers, allowing identification of the most promising channels for investigation.

The formation of *bound* ion-pair systems is of particular interest due to their

large size, simple hydrogen-like structure, and large reduced mass. An illuminating analogy is that of a hydrogen atom with a heavy electron, with mass comparable to the proton; dynamical phenomena, such as the evolution of radial and angular wave-packets, occur on a dramatically lengthened time-scale, giving excellent temporal resolution for precision tests of theoretical models.

Each atomic Rydberg series shown in figure 1.1 can be viewed as a set of long-range asymptotes of molecular Rydberg states, where the high density of states gives rise to rich dynamics with multiple avoided crossings as a Rydberg–ground-state atom-pair approach along a potential energy surface. Disentangling the various interactions can shed light on the underlying molecular states, and is of particular interest as improvements in laser technology provide new opportunities for precision measurement and control in this highly-excited energy region.

1.2 Outline of the thesis

A review of the relevant literature is presented in chapter 2, including the study of highly-excited molecules, with a particular focus on ion-pair states of molecules. Additional topics include background of, and perspectives on, experimental work with atoms and molecules in the ultracold regime, along with discussion of relevant instrumentation and techniques, and potential areas of study using the experimental apparatus developed.

In chapter 3, an in-depth study of highly-excited states of hydrogen fluoride (HF) is presented, demonstrating the subtlety of the intramolecular interactions in a system as apparently simple as HF. A particular hyperfine constant is obtained for the C $^1\Pi$-Rydberg state, along with quantitative details of interaction between the C-state and

the highly-ionic $B\,^1\Sigma^+$-state.

The focus shifts to alkali-metals in chapter 4, with a theoretical analysis of coupling between the ionic potential energy curve and asymptotes of the many short-range covalent curves over a broad range of internuclear distances. These calculated results can be used for determination of cross-sections for ion-pair formation in future experimental work, and an example of such a calculation is included at the end of this chapter.

Chapter 5 describes the theoretical basis for the magneto-optical trap (MOT), while chapter 6 describes its experimental implementation, including extensive details of the instrumentation, procedures and physical parameters used in the MOT apparatus.

Finally, chapter 7 details the development and application of a calibrated polarimetry technique used to optimize polarization in the MOT optics in addition to correcting for experimental uncertainty and manufacturing tolerances in all other polarization dependent measurements taken in the laboratory.

Chapter 2

Literature Review

The work presented in this thesis includes experimental and theoretical studies focused on highly-excited states of diatomic molecules. The following sections provide an overview of the relevant literature, covering atomic and molecular theory, experimental techniques for the production of ultracold atoms and molecules, and details of some of the optical instrumentation used in such experiments.

2.1 Highly-excited states of atoms and molecules

Many of the interesting properties of highly-excited electronic states of atoms and molecules can be qualitatively understood through the simple *Bohr model* of the hydrogen atom. A fundamentally classical model with an electron in a circular orbit and quantization added phenomenologically though discrete orbits with electronic angular momentum, $L = n\hbar$ ($n \in \mathbb{Z}^{>0}$), the orbital radii increase as n^2, and hence the total energy, with a $-1/r$ dependence, increases like $-1/n^2$. This is the basis for the existence of Rydberg series in atoms and molecules, a converging series of energy

levels with ever increasing density-of-states as the spacing falls off like $1/n^3$.

A comprehensive treatise on Rydberg atoms, covering both theoretical and experimental considerations, is the work by Gallagher [10], which updates and expands upon the earlier work by Koch [11].

High angular momentum Rydberg states known as *circular states*, with $|m_\ell| = \ell = n - 1$ can provide a link to the simple, classical view embodied by the Bohr model, with a localized wave-packet travelling on a circular orbit [12]. Such a possibility was conceived in the early days of quantum mechanics in a thought experiment by Schrödinger [13], however the attempt to construct long-lasting localized atomic wave-packets similar to coherent states of the harmonic oscillator seemed doomed due to the decoherence resulting from uneven atomic level spacings. For very high n states the level spacing is approximately constant over a short range and the localized wave-packet can be observed over multiple orbital periods.

The large dipole moments exhibited by atoms in high-n states in the presence of a modest electric field opens up the possibility of inducing entanglement via the strong dipole–dipole interactions between proximate Rydberg atoms [14]. Recent advances include demonstration of entanglement between two individual atoms trapped in separate optical dipole traps [15].

Recent studies on highly-excited rubidium revealed a novel mechanism for the formation of diatomic molecules at extremely large bond-lengths based on low-energy scattering of a Rydberg electron off a ground-state atom [16], demonstrating the continuing interest in potential energies and interaction in highly-excited states. An observed mechanism for producing exotic polar-molecules known as *heavy-Rydberg states* involves collisional charge exchange between a Rydberg state of potassium and

various molecular targets [17].

Similar polar-molecules have been produced in a very different way through direct optical excitation of ground-state molecular hydrogen to a state that at short-range has the characteristics of a conventional molecular Rydberg-state, while at long-range corresponds to an ion-pair with a pure $-1/R$ potential energy curve [18],

$$\text{[Short-range]} \qquad \mathrm{H}_2^+ + e^- \longleftrightarrow \mathrm{H}^+ + \mathrm{H}^- \qquad \text{[Long-range]}. \tag{2.1}$$

Even in more conventional molecular Rydberg-states there are numerous interesting features, including breakdown [19] or even inversion [20] of the Born–Oppenheimer approximation, autoionization due to coupling of discrete levels to the electronic continuum [21], and intramolecular perturbations [22]. These are just some of the many features that make highly-excited molecules an excellent laboratory for investigating the details of quantum mechanics.

2.2 Atoms and molecules in the ultracold regime

The development of techniques for cooling atoms to temperatures close to absolute zero has proved to be revolutionary for experimental physics in many senses. Low thermal kinetic energies provide significant advantages for precision spectroscopy [23] and coherent control [24], essentially eliminating Doppler- and collisional-broadening, and dramatically increasing the dephasing time. Ultracold samples can be confined in shallow traps such as the optical dipole trap [25] and magnetic quadrupole trap [26], and perhaps more significantly, low temperatures can reveal quantum mechanical effects such as Bose-Einstein condensation [27], otherwise swamped by kinetic energies

many orders of magnitude larger than the spacing of quantized energy levels.

Optical cooling techniques, both through the original Doppler-cooling scheme [28] and with the addition of polarization-gradient cooling [29] have proved very successful for certain classes of atoms, cooling samples to ~mK temperatures, while subsequent evaporative cooling can achieve temperatures as low as 0.5 nK, at the expense of losing a large fraction of the sample [30].

An extension of the simple concept of the optical dipole trap is the optical lattice, creating a 1D, 2D or 3D lattice of shallow attractive potentials formed at the intersection of orthogonal continuous-wave (CW) laser beams, analogous to the periodic potential experienced by electrons in a crystal [31]. Ultracold atoms placed in the lattice exhibit the classic characteristics of Bloch waves, with discrete allowed energy bands separated by forbidden band-gaps [32].

The ability to tune the interaction strength by varying the well depths [33], or using an applied magnetic field to to tune the atom–atom scattering lengths around a Feshbach resonance [34], gives experimental control over an important parameter that is difficult or impossible to control in more traditional condensed matter systems. The flexibility and control afforded by cold atoms in an optical lattice has given rise to the rapidly expanding field of condensed matter simulations [35, 36].

Obtaining ultracold *molecular* samples has proved much more challenging and is generally achieved through photoassociation of ultracold atoms [37]. Other promising techniques include Stark deceleration [38] and buffer-gas cooling [39], while some attempts have been made to apply laser-cooling to simple molecules [40].

With the realization of ultracold molecules comes the advent of ultracold chemistry [6]. In this regime the role of barriers on potential energy surfaces can change

dramatically as tunnelling becomes the dominant pathway for chemical reactions. Many-body and cavity effects can influence reaction dynamics due to the increase in de Broglie wavelengths at low temperatures [41].

2.3 Optical measurement and control instrumentation

The type of light source discussed in section 6.1 constitutes one of a variety of designs for an *external cavity diode laser* (ECDL). The common feature of the designs is a diffraction grating used to delineate an external cavity, with diffracted light from the grating fed back into the diode to seed additional gain within a spectral range defined by the angle of the grating.

The Littrow configuration describes a geometry in the application of a diffraction grating for which diffracted light at a particular wavelength and diffraction order travels back along the incident path [42]. Littrow configuration ECDLs can use either a reflection [43, 44] or transmission [45] grating; the transmission-type can use a simpler geometry but requires a very high quality grating to get sufficient feedback and hence the reflection-type is more common. Further details of a reflection-type, Littrow configuration ECDL are discussed in section 6.1.1.

Another class of ECDLs uses a reflection diffraction grating at grazing incidence ($\theta_{\text{incident}} \rightarrow 90°$) such that the incident beam covers a large area of the grating, increasing the spectral resolution of the grating [46], and hence reducing the output linewidth at the expense of the diffraction efficiency. The canonical example of such a system is the Littman–Metcalf design [47], originally conceived for use with high

gain, pulsed dye lasers, for which the low diffraction efficiency is of little concern, but later applied to diode lasers [48] and used for cooling alkali atoms [49].

Previous works have provided limited analyses of the uncertainties in determining the polarization-state of a light source. Williams [50] analyzed various sources of polarimetry errors due to misalignment of optics, finite polarizer extinction ratio, and uncertainty in laser wavelength, using the method of Jones matrix eigenanalysis. In most cases no particular calibration approach was suggested.

Focusing on uncertainty in the azimuthal orientations of the two optics in a rotating quarter-wave plate polarimeter, Flueraru *et al.* looked for consistency between Stokes parameters calculated via the conventional, Fourier analysis scheme and those obtained through inversion of a linear system constructed from a set of up to ten intensity measurements at arbitrary azimuthal angles of the quarter-wave plate. A scheme for correcting for a *known* deviation of the wave plate from quarter-wave retardance was proposed [51].

The effects of finite polarizer extinction ratio, spatially varying wave plate retardance, and variation of retardance with incident angle were analyzed by Tyo and Wei for imaging polarimeters, constructing a 'data reduction matrix' from a set of measured Stokes vectors and solving a linear system of equations using the known input Stokes vector. The resulting solutions were compared with mathematical models and used to optimize experimental parameters [52].

Chapter 3

Molecular Rydberg State Perturbations – An Example

Molecules, like atoms, have electronic Rydberg series with levels generally corresponding to different configurations of electrons in molecular orbitals, with a density of states that increases with increasing energy up to the first ionization limit (the precise configuration depends on bond lengths and angles). The standard approach for the calculation of molecular eigenenergies is based on the Born–Oppenheimer approximation assuming the separability of the nuclear and electronic motions. Under this assumption the different configurations of electrons can be associated with potential energy surfaces which vary as a function of the bond lengths and angles [53].

Various interactions can couple the different electronic states leading to inter-state perturbations that produce a set of eigenstates formed from linear combinations of electronic configurations with characteristics determined by the parent states [54]. Often the parentage of a particular eigenstate is dominated by one configuration and it can be useful to use the quantum numbers describing this parent state to label the

coupled eigenstate, although this is of course only an approximation.

The large excitation energies required for Rydberg state spectroscopy make this a challenging energetic region to explore using many of the standard spectroscopic techniques. In particular, the difficulty of producing laser systems at very short wavelengths makes laser spectroscopy, one of the workhorses of high resolution molecular spectroscopy, unfeasible in this spectral region for most tunable laser systems.

The nascency of the work described in this chapter can be traced to an earlier lower-resolution spectroscopic investigation of hydrogen-fluoride (HF) [55], and the more recent development of a narrow-bandwidth extreme-ultraviolet (XUV) laser system by the group of Prof. Wim Ubachs[1] [56]. The spectra were obtained by Prof. Ubachs' group, resulting in the first observation of hyperfine structure in molecular Rydberg states through direct optical excitation. The subsequent fitting, analysis and determination of molecular constants were all performed by the author under the supervision of Prof. Shiell in the Optical Physics Group at Trent University [57].

3.1 Magnetic hyperfine structure

Hyperfine structure refers to the contribution to the internal energy of atoms and molecules due to the nuclear electric and magnetic multipole moments (excluding the electric monopole) in the presence of internally generated electric and magnetic fields. Typically the leading term in the hyperfine Hamiltonian represents the energy of the nuclear magnetic dipole moments in the magnetic field generated by both the orbital motions of the electrons and the spin magnetic dipoles, commonly referred to as the magnetic hyperfine Hamiltonian.

[1]Laser Centre of the Vrije Universiteit (LCVU), Amsterdam, The Netherlands.

The presence of a 2^q-pole moment ($q \in \mathbb{Z}^{\geq 0}$) requires a nuclear spin, $I \geq q/2$ [2], with the result that any nucleus with non-zero nuclear spin, $I \geq 1/2$, has an associated magnetic dipole moment given by

$$\boldsymbol{\mu}_I = g_I \mu_\mathrm{N} \mathbf{I}, \tag{3.1}$$

where g_I is the nuclear g-factor specific to each nucleus, $\mu_\mathrm{N} = e\hbar/(2m_\mathrm{p})$ is the nuclear magneton and $\mathbf{I}$ is the vector nuclear angular momentum in units of $\hbar$.

The magnetic hyperfine Hamiltonian represents the energy associated with this dipole moment in the presence of a magnetic field, $\mathbf{B}$,

$$\hat{\mathcal{H}}_\mathrm{hfs} = -\boldsymbol{\mu}_I \cdot \mathbf{B}, \tag{3.2}$$

where the magnetic field derives from both the orbital and spin angular momentum of the electrons,

$$\mathbf{B} = \mathbf{B}_\ell + \mathbf{B}_s. \tag{3.3}$$

The orbital component at a nucleus, $\mathbf{B}_\ell$, can be calculated from the form of the Biot–Savart law [59] for the magnetic field due to a point charge q, moving with velocity $\mathbf{v}$ [3], and recognizing that the position of the nucleus relative to the electron is $-\mathbf{r}$,

$$\mathbf{B}_\ell = \frac{\mu_0}{4\pi} \frac{q\mathbf{v} \times (-\mathbf{r})}{r^3}. \tag{3.4}$$

[2] See reference [58], page 577.

[3] Strictly, a retarded potential is required to account for finite propagation-time effects, however for a molecule such as HF with light nuclei, $v \ll c$ even for core-penetrating states.

Written in terms of the Bohr magneton, $\mu_{\rm B} = e\hbar/(2m_e)$, we have

$$\mathbf{B}_\ell = -2\mu_{\rm B}\frac{\mu_0}{4\pi r^3}\frac{\mathbf{r}\times m_e\mathbf{v}}{\hbar}, \tag{3.5}$$

which includes the orbital angular momentum in units of $\hbar$, $\boldsymbol{\ell} = (\mathbf{r}\times m_e\mathbf{v})/\hbar$,

$$\mathbf{B}_\ell = -2\mu_{\rm B}\frac{\mu_0}{4\pi r^3}\boldsymbol{\ell}. \tag{3.6}$$

For the case of multiple unpaired electrons a summation over each orbital angular momentum vector is required. In order to work in the coupled basis using the total angular momentum, $\mathbf{L}$, the projection operator, $\hat{\phi}_i^\ell$, must be used, for which $\sum_i \boldsymbol{\ell}_i = \sum_i \hat{\phi}_i^\ell \mathbf{L}$ [53]. For cases with a well defined projection of orbital angular momentum onto the internuclear axis, $\Lambda = \sum_i \langle \hat{\ell}_{zi}\rangle$, the projection operator can be written as $\hat{\phi}_i^\ell = \hat{\ell}_{zi}/\Lambda$, giving

$$\mathbf{B}_\ell = -2\mu_{\rm B}\frac{\mu_0}{4\pi\Lambda}\sum_i \frac{\hat{\ell}_{zi}}{r_i^3}\mathbf{L}. \tag{3.7}$$

The resulting orbital component of the magnetic hyperfine Hamiltonian is given by

$$\hat{\mathcal{H}}_{\rm hfs}^\ell = 2g_I\mu_{\rm N}\mu_{\rm B}\frac{\mu_0}{4\pi\Lambda}\sum_i \frac{\hat{\ell}_{zi}}{r_i^3}\hat{\mathbf{I}}\cdot\hat{\mathbf{L}} \tag{3.8}$$

$$= \hat{a}\hat{\mathbf{I}}\cdot\hat{\mathbf{L}}. \tag{3.9}$$

The electron spin components of this Hamiltonian come from inserting the standard form for the magnetic field due to a magnetic dipole moment[4] for $\mathbf{B}_s$, leading to the form commonly used for states with well defined projections, Λ and $\Sigma = \sum_i \langle \hat{s}_{zi}\rangle$,

[4]See reference [60], equation 5.64.

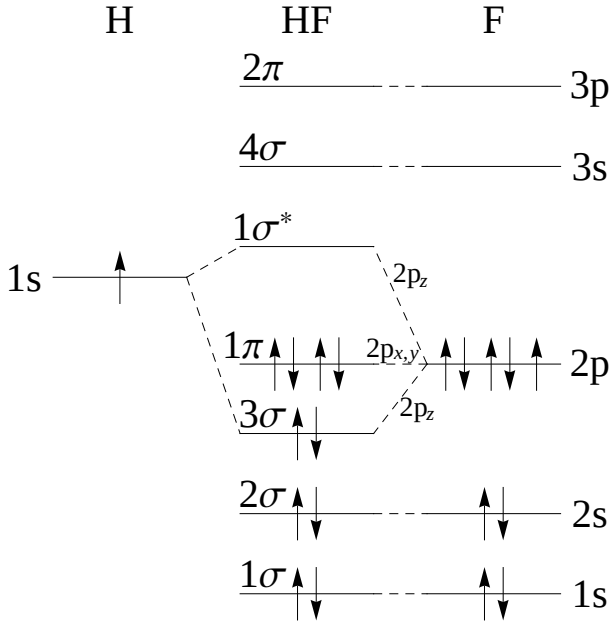

Figure 3.1: A schematic showing the electronic configuration of HF with molecular orbitals associated with the orbitals of the isolated atoms; energies not to scale. The configuration shown is the primary configuration in the ground $X\,^1\Sigma^+$ state, with an ionic character. At larger bond-lengths this configuration contributes to the B-state as shown in figure 3.3.

of the electronic orbital and spin angular momenta respectively [61, 62, 63],

$$\hat{\mathcal{H}}_{\rm hfs} = \hat{a}\hat{\mathbf{I}}\cdot\hat{\mathbf{L}} + \hat{b}_{\rm F}\hat{\mathbf{I}}\cdot\hat{\mathbf{S}} + \frac{1}{3}\hat{c}\left\{3\hat{I}_z\hat{S}_z - \hat{\mathbf{I}}\cdot\hat{\mathbf{S}}\right\} + \frac{1}{2}\hat{d}\left\{e^{2i\phi}\hat{I}^-\hat{S}^- + e^{-2i\phi}\hat{I}^+\hat{S}^+\right\}. \tag{3.10}$$

3.1.1 Hyperfine structure in $H^{19}F$

The analysis detailed in this chapter investigates and explains experimental results for excitation from the ground state of $H^{19}F$, which at the equilibrium bond-length consists primarily of the highly-ionic $1\sigma^2 2\sigma^2 3\sigma^2 1\pi^4$ electronic configuration shown in figure 3.1. This configuration, comprised entirely of closed subshells, produces the $X\,^1\Sigma^+$ ground state [64].

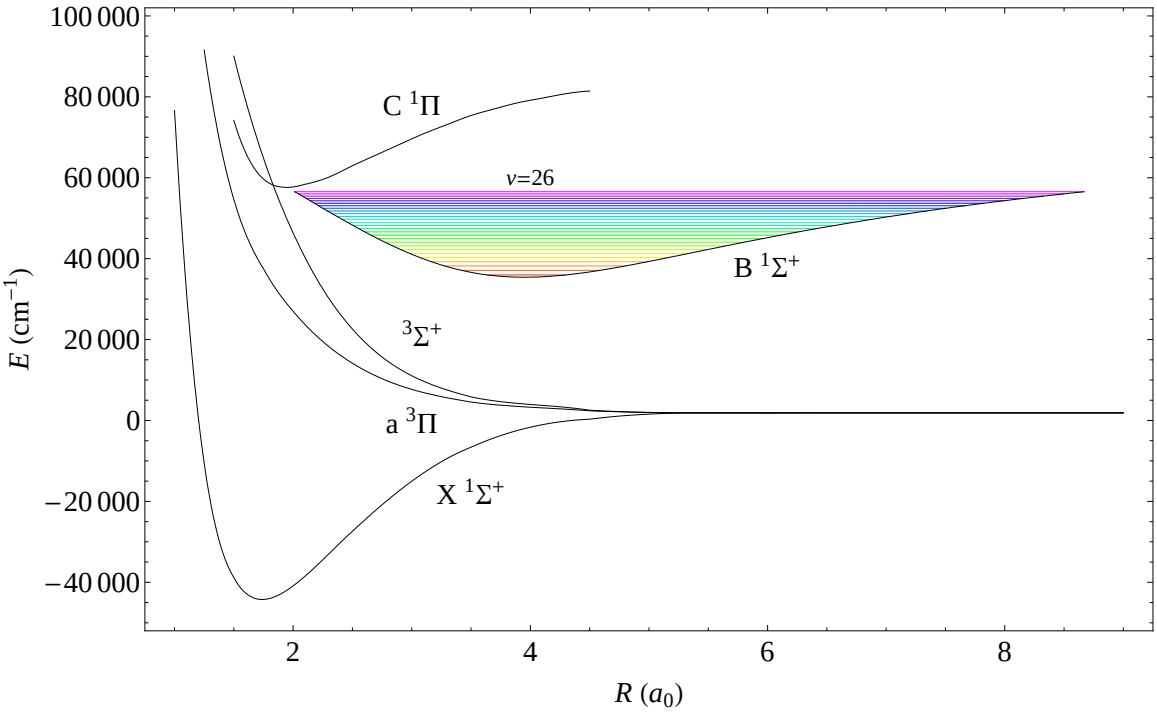

Figure 3.2: Some potential energy curves of HF, showing experimentally derived vibrational levels of the *outer well* of the $B\,^1\Sigma^+$ state up to $v = 26$ [67, 68, 69].

As we shall see, the excitation ends up being to a superposition of particular vibrational levels of the $B\,^1\Sigma^+$ and $C\,^1\Pi$ electronic states, shown in figure 3.2, however the eigenstate superposition is dominated by the C-state, with a $1\sigma^2 2\sigma^2 3\sigma^2 1\pi^3 4\sigma$ configuration. The orbital angular momentum of the single unpaired 1π electron is therefore the only contribution to the summation in equation 3.8 and hence $\langle \hat{\ell}_z \rangle = \Lambda = \pm 1$. The B-state is a long-range, double-well state [65], consisting of a covalent, $1\sigma^2 2\sigma^2 3\sigma^2 1\pi^3 2\pi$, configuration at short-range, an anti-bonding, $1\sigma^2 2\sigma^2 3\sigma 1\pi^4 1\sigma^*$, configuration at intermediate range, and an ionic, $1\sigma^2 2\sigma^2 3\sigma^2 1\pi^4$, configuration at long-range [66]. Figure 3.3 gives a schematic illustration of how avoided crossings between different configuration state functions produce this type of potential energy curve.

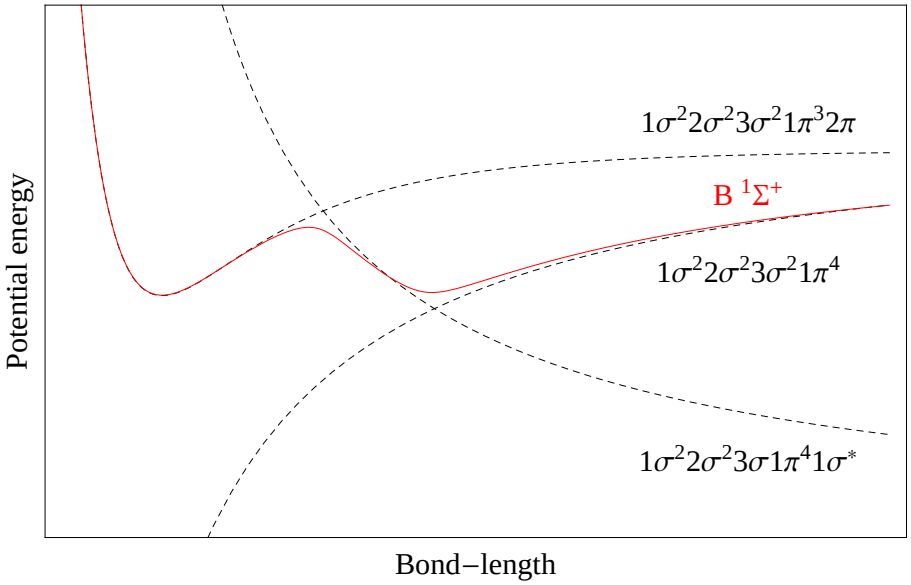

Figure 3.3: A schematic illustration of how coupled configuration states combine to produce a double-well molecular potential energy curve. The curves are labelled with the particular configurations that contribute to the B $^1\Sigma^+$ state of HF for comparison only and have not been calculated for any particular state.

All of the relevant states are singlet states ($S = 0$) so that the complete magnetic hyperfine Hamiltonian only includes the first term from equation 3.10, one for each nucleus of non-zero spin, $I_\mathrm{F} = I_\mathrm{H} = 1/2$,

$$\hat{\mathcal{H}}_\mathrm{hfs} = \hat{a}_\mathrm{F}\hat{\mathbf{I}}_\mathrm{F}\cdot\hat{\mathbf{L}} + \hat{a}_\mathrm{H}\hat{\mathbf{I}}_\mathrm{H}\cdot\hat{\mathbf{L}}. \tag{3.11}$$

The $\hat{a}$ operators are given by

$$\hat{a} = 2g_I\mu_\mathrm{N}\mu_\mathrm{B}\frac{\mu_0}{4\pi}\frac{1}{r^3}, \tag{3.12}$$

where r is the radial coordinate of the unpaired 1π electron with respect to the nucleus in question, for which g_I is the nuclear g-factor. The two atomic orbitals

comprising the 1π subshell are the $2p_{x,y}$ orbitals of atomic fluorine and hence this electron remains localized around the fluorine nucleus.

The angular momentum coupling scheme used in this work is an extended version of Hund's case (a_β) incorporating the two nuclear angular momenta, as illustrated in figure 3.4. Working in the coupled representation we have a basis ket,

$$|\gamma\, \Lambda\, S\, \Sigma\, J\, I_\mathrm{F}\, F_1\, I_\mathrm{H}\, F\, M_F\rangle, \tag{3.13}$$

where S is the total electron spin quantum number, Σ is the projection of $\mathbf{S}$ onto the internuclear axis, and γ represents the electronic configuration and all other quantum numbers required to uniquely define each state. The coupling scheme assumes that the interaction with $\mathbf{I}_\mathrm{F}$ is the dominant term in the hyperfine energy,

$$\begin{aligned} \mathbf{J} &= \mathbf{L} + \mathbf{S} + \mathbf{R}, \\ \mathbf{F}_1 &= \mathbf{J} + \mathbf{I}_\mathrm{F}, \\ \mathbf{F} &= \mathbf{F}_1 + \mathbf{I}_\mathrm{H}. \end{aligned} \tag{3.14}$$

The treatment of angular momentum in quantum mechanics places no explicit restriction on the order in which the different angular momenta are coupled: in an exact solution any ordering must lead to the same set of energy eigenvalues. Coupling the nuclear spin associated with the dominant contribution to the hyperfine energy first results in smaller off-diagonal elements of the Hamiltonian such that low-order perturbation theory gives more accurate results.

For a state $|\psi\rangle$, the diagonal matrix elements of each term in equation 3.11 are proportional to the hyperfine parameter, $a \equiv \langle\psi|\hat{a}|\psi\rangle$, for the respective nuclei. These

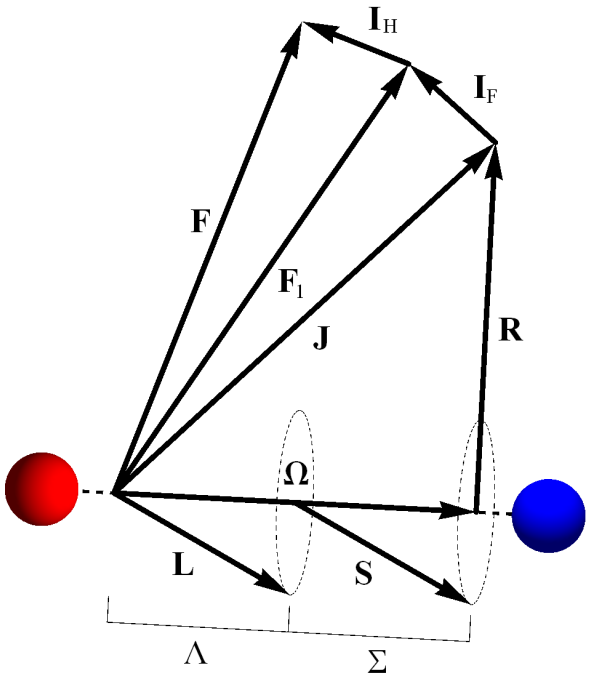

Figure 3.4: The angular momentum coupling scheme used for HF. The orbital angular momentum, **L**, is coupled to the internuclear axis due to the electrostatic attraction of the nuclei, while the electron spin, **S**, is more weakly coupled via the spin–orbit interaction. The precise orientations of **L** and **S** are not well defined so the axial components, Λ and Σ respectively, are combined to form a vector, $\mathbf{\Omega}$, that is coupled to the rotational angular momentum, **R**, to form **J**. The nuclear angular momenta, $\mathbf{I}_F$ and $\mathbf{I}_H$, are coupled in order of their contributions to the hyperfine energy to form first $\mathbf{F}_1$ and then **F**.

parameters determine the strength of the interaction between the nuclear spin and the electronic orbital angular momentum, and, because in general they include a factor of $\langle \sum_i \hat{\ell}_{zi}/r_i^3 \rangle$, also provide information about the spatial distribution of the chemically important unpaired electrons.

Although the ground, $X\,^1\Sigma^+$, electronic state does feature hyperfine effects due to both the nuclear spin–nuclear spin ($\mathbf{I}_F \cdot \mathbf{I}_H$) and nuclear spin–rotation ($\mathbf{I} \cdot \mathbf{R}$) interactions, the splitting of ~300 kHz [70] is negligible compared with both the C-state splitting and the experimental resolution and is hence neglected in the analysis that

follows.

3.2 Ion-pair–covalent state mixing

The hyperfine a-parameter takes the same value for all rotational levels of a given *pure* vibronic state, however, coupling between the rotational levels of different vibronic states can introduce an apparent rotational dependence due to the effective 'leaking' of hyperfine effects into another state. The correct view of this effect is that of excitation to a linear combination of states, with the amount of the perturbing state mixed in dependent upon the rotational level in question.

For states described by Hund's case (a) or (b), each ro-vibronic level of an electronic state with $|\Lambda| > 0$ consists of two components with projections of $\mathbf{L}$ onto the internuclear axis of $\pm|\Lambda|$. Together these two components are known as a Λ-doublet and in the absence of rotation they remain perfectly degenerate. Rotation breaks the symmetry between the two components and lifts the degeneracy by an amount that depends on the value of Λ (or Ω for non-singlet states) and increases with J [53].

This effect, known as Λ-doubling because it effectively doubles the number of distinct energy levels, occurs due to mixing of the rotational levels of a degenerate electronic state with the corresponding levels of a Σ state of the same multiplicity. Mixing occurs only between levels with the same e/f-rotationless parity. Each Λ-doublet consists of an e/f pair while Σ^+ states consist entirely of e-parity levels and Σ^- states are entirely f-parity.

For the case of the C $^1\Pi$, $v=0$ level in $H^{19}F$, Λ-doubling occurs due to mixing with proximate vibrational levels of the B $^1\Sigma^+$ state. The e-parity components of the low-J rotational levels mix predominantly with the corresponding rotational levels of the

nearby $B\,^1\Sigma^+\, v=29$-vibrational level [55]. In the notation of rotational spectroscopy, $\{P, Q, R\}$-branch absorption lines correspond to transitions with $\Delta J = \{-1, 0, +1\}$, and $\{P(J), Q(J), R(J)\}$-transitions correspond in absorption to $J \to \{J-1, J, J+1\}$. The ground electronic state is a Σ^+ with only e-parity levels, and hence from the e/f-parity selection rules[5] the P- and R-branch lines probe the perturbed e-parity components of the C-state levels, while Q-branch lines probe the f-parity components that do not interact with the B-state. As a consequence of the mixing, the excited eigenstate with quantum number J must be written as a linear combination of the C- and B-state contributions,

$$|J\rangle = c_1(J)|C\ ^1\Pi,\ v=0,\ J\rangle + c_2(J)|B\ ^1\Sigma^+,\ v=29,\ J\rangle. \tag{3.15}$$

A quantitative measure of the mixing is given by the *mixing fraction*, ζ_J, obtained by projecting this eigenstate onto the $|C\ ^1\Pi,\ v=0,\ J\rangle$ state,

$$\zeta_J = |\langle C\ ^1\Pi,\ v=0,\ J|J\rangle|^2 = |c_1(J)|^2. \tag{3.16}$$

The remainder of this section covers methods for calculating the amount of mixing and the resultant energy shifts, both using the effective-Hamiltonian approach and then using the results of a deperturbation analysis.

[5] $e \leftrightarrow e$ and $f \leftrightarrow f$ for P and R branches, and $e \leftrightarrow f$ for the Q-branch [71].

3.2.1 Λ-doubling calculations using the effective Hamiltonian

The typical approach used for Λ-doubling calculations makes use of the *effective Hamiltonian* to reduce the size of the basis set and derive simple expressions for approximate eigenenergies. Rigorously defined, the effective Hamiltonian is the operator obtained by projecting the Hamiltonian onto the subspace of states within a given vibronic level to the desired resolution (rotational, spin–orbit, hyperfine). Calculating eigenenergies of the full Hamiltonian using this method requires that the effects of off-diagonal matrix elements between states of the vibronic level of interest and those of any other vibronic level are included perturbatively through the inclusion of additional parameters.

For the case of Λ-doubling interactions, there are three such parameters commonly used: the o, p and q parameters, representing the spin–orbit energy, the coupled spin–orbit–rotational energy, and the rotational energy respectively. For singlet states such as those under consideration only q is non-zero, given by

$$q = 2\sum_{\gamma,v} \pm \frac{|\langle \gamma'\,{}^{2S+1}\Lambda\, v'|\hat{B}(R)\hat{L}_{+})|\gamma\,{}^{2S+1}\Sigma^{\pm}\, v\rangle|^2}{E_{\gamma,v} - E_{\gamma',v'}}, \tag{3.17}$$

where $\hat{B}(R) = 1/(2\mu R^2)$ is the rotational kinetic energy operator and the sign is chosen to match the parity of the Σ-state in question for each value of γ in the summation. The energy shift due to the rotational Λ-doubling interaction is given by $qJ(J+1)$.

3.2.2 Perturbations between near-degenerate levels

For the case of a state with $|\Lambda| > 0$ with a subset of levels perturbed by the nearly-degenerate levels of a Σ-state with the appropriate parity, the effective Hamiltonian approach breaks down and must be replaced with a more general treatment capable of explicitly including coupling between rotational levels of different electronic states.

An effect that couples states of different $|\Lambda|$ is known as a *heterogeneous perturbation*. For a rotating molecule, the rotational Hamiltonian can couple states with $\Delta\Lambda = \pm 1$ and $\Delta S = \Delta\Sigma = 0$, an effect sometimes referred to as the Coriolis interaction [72]. The rotational Hamiltonian can be compactly written as

$$\hat{\mathcal{H}}_{\text{rot}} = \hat{B}\hat{R}^2, \tag{3.18}$$

where $\hat{B}(R) = 1/(2\mu R^2)$ and $\hat{\mathbf{R}}$ represents the rotational angular momentum of the molecule.

For any linear molecule, including all diatomics, the moment of inertia about the molecular axis is identically zero and hence $R_z = 0$. Expressing the Hamiltonian in terms of the conventional Hund's case (a) total angular momentum (excluding nuclear spin) quantum number, J, gives,

$$\hat{\mathcal{H}}_{\text{rot}} = \hat{B}[(\hat{J}_x - \hat{L}_x - \hat{S}_x)^2 + (\hat{J}_y - \hat{L}_y - \hat{S}_y)^2], \tag{3.19}$$

which can in turn be expressed in terms of the mutually commuting operators, $\hat{J}^2$, $\hat{J}_z$, $\hat{L}^2$, $\hat{L}_z$, $\hat{S}^2$, $\hat{S}_z$, and their associated raising and lowering operators, $\hat{J}_\pm = \hat{J}_x \pm i\hat{J}_y$,

Table 3.1: Variation of the mixing fraction, ζ_J, with J.

J	Mixing fraction, ζ_J
1	0.99981
2	0.99914
3	0.99588
4	0.91807
5	0.97873

$\hat{L}_\pm = \hat{L}_x \pm i\hat{L}_y$ and $\hat{S}_\pm = \hat{S}_x \pm i\hat{S}_y$,

$$\begin{aligned}\hat{\mathcal{H}}_{\rm rot} =& \hat{B}[(\hat{J}^2 - \hat{J}_z) + (\hat{L}^2 - \hat{L}_z) + (\hat{S}^2 - \hat{S}_z)^2 \\ &+ (\hat{L}_+\hat{S}_- + \hat{L}_-\hat{S}_+) - (\hat{J}_+\hat{L}_- + \hat{J}_-\hat{L}_+) - (\hat{J}_+\hat{S}_- + \hat{J}_-\hat{S}_+)]. \end{aligned} \tag{3.20}$$

Note that these operators are all defined in the *molecule-fixed frame*, with the result that the components of $\hat{\mathbf{J}}$ have anomalous commutation relations ($[\hat{J}_x, \hat{J}_y] = -i\hbar\hat{J}_z$), and consequently $\hat{J}_+$ is a lowering operator and $\hat{J}_-$ is a raising operator[6]. Product operators of the form $\hat{J}_\pm\hat{L}_\mp$ and $\hat{J}_\pm\hat{S}_\mp$ would give nonsensical results if this were not the case.

For the case of perturbations between the $\left(\mathrm{B}\ ^1\Sigma^+,\ v{=}29,\ J\right)$ and $\left(\mathrm{C}\ ^1\Pi,\ v{=}0,\ J\right)$ levels, the first bracketed term in equation 3.20 gives rise to the diagonal matrix elements, while the fifth bracketed term couples states with $\Delta\Lambda = \pm 1$ and $\Delta\Sigma = 0$. The mixing can be calculated by constructing a 2×2 matrix for each value of J, given by,

$$\underline{\underline{\mathcal{H}}}_{\rm rot} = \begin{pmatrix} E_{\rm B29} + B_{\rm B29}J(J+1) & \beta\sqrt{J(J+1)} \\ \beta\sqrt{J(J+1)} & E_{\rm C0} + B_{\rm C0}J(J+1) \end{pmatrix}, \tag{3.21}$$

[6]See reference [73], page 338.

where $\beta = -\langle \mathrm{C}\ ^1\Pi|\hat{B}\hat{L}_+|\mathrm{B}\ ^1\Sigma^+\rangle$. The unknown parameters were obtained from a deperturbation of absolute line positions from reference [55]: $E_{\mathrm{B29}} = 105\,393.91044$ cm^{-1} and $E_{\mathrm{C0}} = 105\,867.52322$ cm^{-1} are the line-centres of the transitions to the respective vibronic states, $B_{\mathrm{B29}} = 104.701$ GHz and $B_{\mathrm{C0}} = 403.2022$ GHz are the respective rotational constants, and $\beta = 75.7336$ GHz is the heterogeneous rotational perturbation parameter. The eigenvalues of this matrix are the energies of the mixed states described by equation 3.15,

$$E_J = \frac{1}{2}\Big[(E_{\mathrm{C0}} + E_{\mathrm{B29}}) + (B_{\mathrm{C0}} + B_{\mathrm{B29}})J(J+1) \pm \sqrt{(E_{\mathrm{C0}} - E_{\mathrm{B29}} + (B_{\mathrm{C0}} - B_{\mathrm{B29}})J(J+1))^2 + 4J(J+1)\beta^2}\Big], \tag{3.22}$$

with the positive and negative signs corresponding to those states consisting predominantly of the Π-state and Σ-state respectively. The eigenvectors give the parentage of the eigenstates in terms of the two $|\Lambda|$-states and are used to obtain the mixing fractions defined in equation 3.16 and listed in table 3.1.

Figure 3.5 shows how the perturbation shifts the rotational levels of the two vibronic states by an amount that increases with decreasing separation of the unperturbed levels and changes sign when they cross.

3.3 Experimental details

The hyperfine-resolved XUV spectra of the various rotationally-resolved transitions within the electronic Rydberg transition were taken at the Laser Centre of the Vrije Universiteit, Amsterdam, The Netherlands, by the group of Prof. Wim Ubachs. The basis for these measurements was the development of a narrow-bandwidth pulsed

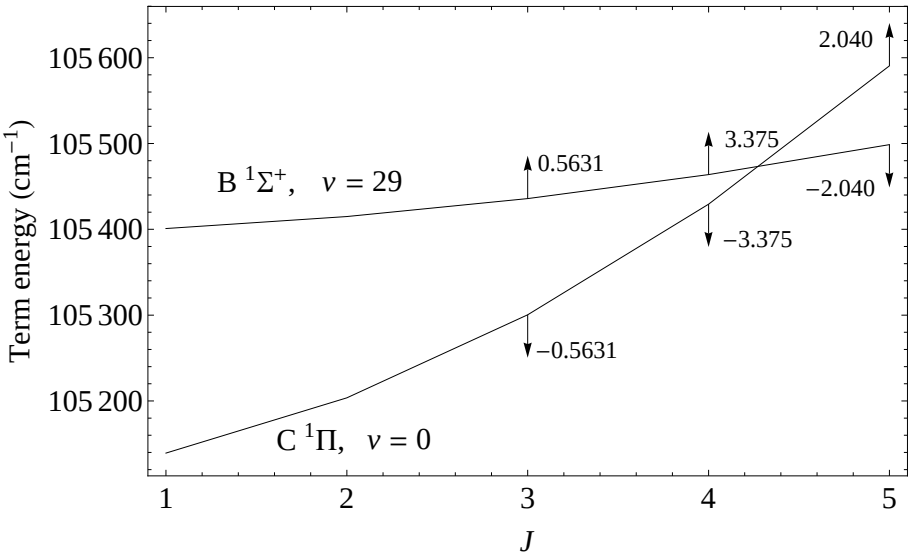

Figure 3.5: Energy shifts due to perturbations between the B $^1\Sigma^+$, $v = 29$ and C $^1\Pi$, $v = 0$ states. The curves represent the unperturbed energies, while the arrows represent the shifts of the perturbed levels in the B- and C-states.

laser source tunable in the region around 95 nm [56]. The author was not part of the group that took the data but a brief description of the experimental setup is included here for completeness.

The initial source was an argon-ion pumped CW ring-dye laser at around 570 nm that is subsequently amplified in three consecutive dye-cells pumped by a frequency-doubled, pulsed Nd:YAG laser at 532 nm. The amplified light is frequency-doubled in a KD*P crystal to produce high-power pulsed UV light at around 285 nm, with up to 90 mJ/pulse. After being coupled into a vacuum chamber through a lithium fluoride window, the UV pulses are frequency-tripled in a pulsed jet of xenon, producing coherent XUV radiation, tunable in the region of 95 nm, with a bandwidth of 250–350 MHz.

The relatively low efficiency of the frequency-tripling process results in pulses

with spatially and temporally overlapped UV and XUV components, ideal for multi-photon ionization processes. These laser pulses were crossed with a pulsed beam of HF produced by a solenoid valve and collimated by a 1 mm diameter aperture.

The XUV photons were tuned across the $(\mathrm{C}\,^1\Pi,\ v = 0)$–$(\mathrm{X}\,^1\Sigma^+,\ v = 0)$ transition, while the UV photons excited from the C-Rydberg state to the continuum, producing HF^+ ions that were extracted with a pulsed electric field and detected with an electron multiplier. This technique is known as 1 XUV + 1 UV resonance-enhanced multi-photon ionization (REMPI) spectroscopy.

Note that no absolute frequency measurements were performed in this experiment. Relative frequency measurements were obtained using transmission fringes, produced by a component of the visible output of the ring-dye laser incident on an actively stabilized étalon, as a frequency reference for the XUV spectrum.

3.4 Determination of the a_{F} hyperfine parameter

Experimental determination of spectroscopic parameters such as the a-hyperfine constant generally proceeds by fitting the spectra obtained to a particular functional form derived from the theory of molecular structure. Fitting the spectra requires calculation of the relative line energies and intensities, and using the appropriate lineshape based on knowledge of the broadening mechanisms present in the experiment.

An in-depth derivation of the matrix elements of the hyperfine Hamiltonian is given in section A.1, here the results are simply quoted. The matrix elements of the terms in equation 3.11 associated with the fluorine and hydrogen nuclei, between bras

and kets of form 3.13, are labelled ME_{F} and ME_{H} respectively,

$$\begin{aligned} ME_{\mathrm{F}} =& \delta_{M_F M_F'} \delta_{FF'} \delta_{F_1 F_1'} a_{\mathrm{F}} \Lambda (-1)^{F_1 + I_{\mathrm{F}} + J + J' - \Lambda} \\ & \times \sqrt{(2J'+1)(2J+1)(2I_{\mathrm{F}}+1)(I_{\mathrm{F}}+1)I_{\mathrm{F}}} \\ & \times \left\{ \begin{array}{ccc} J' & I_{\mathrm{F}} & F_1 \\ I_{\mathrm{F}} & J & 1 \end{array} \right\} \left(\begin{array}{ccc} J' & 1 & J \\ -\Lambda & 0 & \Lambda \end{array} \right) \end{aligned} \tag{3.23}$$

and

$$\begin{aligned} ME_{\mathrm{H}} =& \delta_{M_F M_F'} \delta_{FF'} a_{\mathrm{H}} \Lambda (-1)^{F + 2F_1 + I_{\mathrm{H}} + 2J' + I_{\mathrm{F}} + 1 - \Lambda} \\ & \times \sqrt{(2J'+1)(2J+1)(2F_1'+1)(2F_1+1)} \\ & \times \sqrt{(2I_{\mathrm{H}}+1)(I_{\mathrm{H}}+1)I_{\mathrm{H}}} \left\{ \begin{array}{ccc} F_1' & I_{\mathrm{H}} & F \\ I_{\mathrm{H}} & F_1 & 1 \end{array} \right\} \\ & \times \left\{ \begin{array}{ccc} J' & F_1' & I_{\mathrm{F}} \\ F_1 & J & 1 \end{array} \right\} \left(\begin{array}{ccc} J' & 1 & J \\ -\Lambda & 0 & \Lambda \end{array} \right), \end{aligned} \tag{3.24}$$

where the primed and unprimed quantum numbers refer to the bra and ket labels respectively, both in the excited electronic state with $\Lambda = 1$.

The upper state energy splittings used to fit the data were obtained using first-order perturbation theory. To confirm the validity of this approximation, table 3.2 compares the values obtained in this way with the results of a diagonalization assuming the full Hamiltonian to be block-diagonal in J. All values fall within 5 MHz of the exact values, less than the eventual uncertainties in a_{F} determined from the fit.

Equations 3.23 and 3.24 can be used to obtain the off diagonal elements between

Table 3.2: Comparing 1st order perturbation theory with the results of an exact diagonalization of the Hamiltonian matrix. Because F_1 is only an approximately good quantum number, a small amount of mixing between states of the same F and different F_1 occurs leading to the observed differences. Values given are for the Q(1)-line, in MHz relative to the rotational levels in the absence of hyperfine structure.

F_1	F	$g=2F+1$	1st order pert.	Exact	% diff
3/2	2	5	1151.75	1151.75	0
3/2	1	3	824.417	829.191	0.58
1/2	1	3	-1976.17	-1980.94	0.24
1/2	0	1	-2303.5	-2303.5	0

levels with different J; diagonalizing requires adding the rotational energy, $B_v J(J+1)$, to the diagonal elements. With rotational spacing of ~ 50 cm^{-1}, the effects on the eigenenergies are negligible.

The relative intensity, S, for hyperfine transitions within a rotational line of the C–X absorption spectrum is derived in section A.2. For linearly polarized light and a quantization axis chosen to be parallel to the optical polarization, S takes the form,

$$\begin{aligned} S =& (2F+1)(2F'+1)(2F_1+1)(2F_1'+1) \\ &\times \left[\begin{pmatrix} F' & 1 & F \\ -M_F' & 0 & M_F \end{pmatrix} \begin{Bmatrix} F' & F_1' & I_{\mathrm{H}} \\ F_1 & F & 1 \end{Bmatrix} \begin{Bmatrix} F_1' & J' & I_{\mathrm{F}} \\ J & F_1 & 1 \end{Bmatrix} \right]^2, \end{aligned} \tag{3.25}$$

where the primed and unprimed quantum numbers refer to the bra (final state, $\Lambda = 1$) and ket (initial state, $\Lambda = 0$) labels respectively.

The absolute, two-photon line-intensities for the REMPI process would require knowledge of the photoionization cross-sections for HF in the C-state in addition to details of the laser beam intensity, molecular beam number density, and the geometry

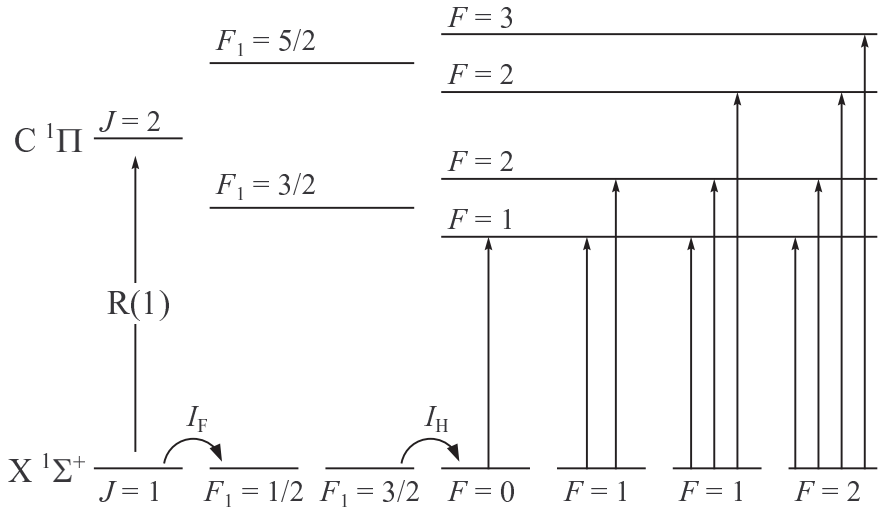

Figure 3.6: Allowed electric dipole transitions for the R(1) line in HF. The ground state has negligible hyperfine splitting, while the excited state exhibits splitting in F_1 due to the $\mathbf{I}_\mathrm{F} \cdot \mathbf{L}$ coupling and splitting in F due to the $\mathbf{I}_\mathrm{H} \cdot \mathbf{L}$ coupling. The electric dipole selection rules are $\Delta F = 0, \pm 1,\ F = 0 \nrightarrow F = 0$ in the absence of an external field, and $\Delta F_1 = 0, \pm 1,\ F_1 = 0 \nrightarrow F_1 = 0$ under the assumption that the fluorine nucleus dominates the hyperfine energy.

of the overlap region. In the absence of precise knowledge of these quantities, the one-photon relative line intensity, S, was used under the assumption that there is no strong dependence of the ionization cross-section on the particular hyperfine component within a rotational line.

For the coupling case described in section 3.1.1 and shown in figure 3.4, the allowed transitions under the electric dipole approximation are taken to be $\Delta F \in \{0, \pm 1\}$ ($F = 0 \nrightarrow F = 0$), $\Delta F_1 \in \{0, \pm 1\}$ ($F_1 = 0 \nrightarrow F_1 = 0$), and $\Delta M_F \in \{0, \pm 1\}$. In fact F_1 is only a good quantum number for the case in which the energy associated with the $\mathbf{I}_\mathrm{H} \cdot \mathbf{L}$ coupling is small compared with that of the $\mathbf{I}_\mathrm{F} \cdot \mathbf{L}$ coupling. This is, as we shall see, a good approximation. Figure 3.6 is a schematic illustration of the allowed transitions within the R(1) absorption line, due to the $J = 1 \rightarrow J = 2$ rotational transition.

Armed with expressions for the energies and intensities of the allowed transitions within a given line, a simulated spectrum can be constructed using the known lineshape based on the broadening mechanisms present in the experimental setup. For the REMPI experiment the primary broadening mechanism is power-broadening due to the high UV power used in the ionization step, with some transit-time broadening associated with the molecular beam crossing a narrow laser beam at right-angles, and residual Doppler-broadening due to divergence of the molecular beam. The power-broadening mechanism results in homogeneous broadening, maintaining the natural, finite-lifetime broadened, Lorentzian lineshape,

$$g(\nu - \nu_0) = \frac{\Delta\nu/(2\pi)}{(\Delta\nu/2)^2 + (\nu - \nu_0)^2}, \tag{3.26}$$

where ν_0 is the respective transition frequency and $\Delta\nu$ is the full-width at half-maximum.

The unknown parameters in the simulated spectra are a_{F}, a_{H} and $\Delta\nu$. The standard fitting process involves varying the unknown parameters to minimize the sum of the squared errors between the simulated and experimental spectra.

Because the sole unpaired electron with a non-zero value of λ in the C-state configuration occupies an essentially unchanged fluorine $2\mathrm{p}_{x,y}$ orbital, it remains localized around the fluorine nucleus and hence the orbital angular momentum coupling to the hydrogen nuclear-spin is weak. Given this weak coupling, the value of a_{H} is expected to be small compared with the experimental uncertainty, and so it is not reasonable to expect the fitting procedure to provide an accurate value. The value used for a_{H} is 107 MHz, obtained through theoretical calculations for the ground state of HF^+ [63], expected to be similar to the neutral Rydberg state due to the decreasing effects on

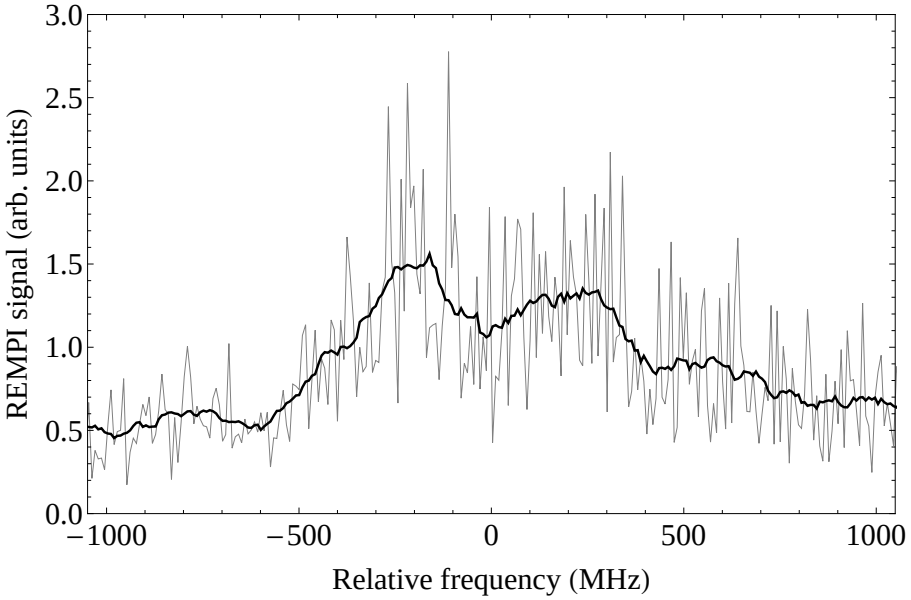

Figure 3.7: A spectrum taken in the region of the HF ($B\,^1\Sigma^+$, $v=30$)–($X\,^1\Pi$, $v=0$) transition, possibly showing hyperfine splitting due to B–C mixing. The bold line shows the same spectrum following the application of a moving average filter with a window of 15 data-points covering ~100 MHz.

the core electrons as the ionization limit is approached.

An initial analysis performed on the available experimental C–X spectra (including lines R(0)–R(4) and Q(1)) found an apparent variation in the value of a_{F} with J, contrary to what would be expected from a simple reading of equation 3.12. Additionally, a single, low quality B–X spectrum was provided, shown in figure 3.7, with a signal–to–noise ratio close to unity. In spite of the noisy data, the apparent presence of splitting in this spectrum initiated the investigation of B–C mixing through the Λ-doubling process as a possible mechanism for the apparent variation in a_{F}.

The experimental C–X spectra with their respective simulated fit lines are shown in figure 3.8 showing the measured lineshapes to be in good agreement with the theory. The apparent value of the a_{F} parameter obtained from each line is given in the figure

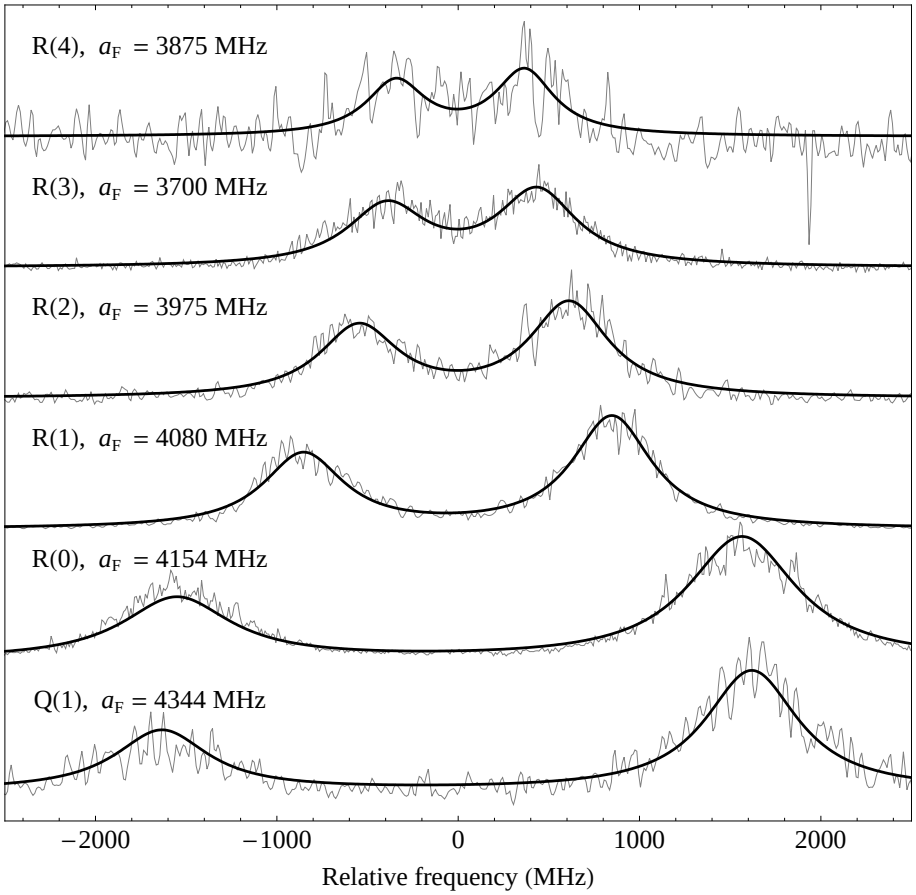

Figure 3.8: Experimental and simulated spectra of the HF C–X transition. The apparent values of a_F derived from each line are included, with the variation showing the effects of perturbation by the nearby $v = 29$ level of the B-state. The relative heights of the spectra have been rescaled for clarity.

although the effects of Λ-doubling must be accounted for before an unperturbed, J-independent value can be obtained.

The value of $\Delta\nu$ was allowed to vary as part of the fitting procedure, arriving at a mean value of 550 MHz, consistent with the ~300 MHz linewidth expected of the light-source described in section 3.3, under the influence of the broadening mechanisms discussed above. Intensity fluctuations in the higher energy peak of the R(0) spectrum and the low SNR in the R(4) spectrum led to values of $\Delta\nu$ differing

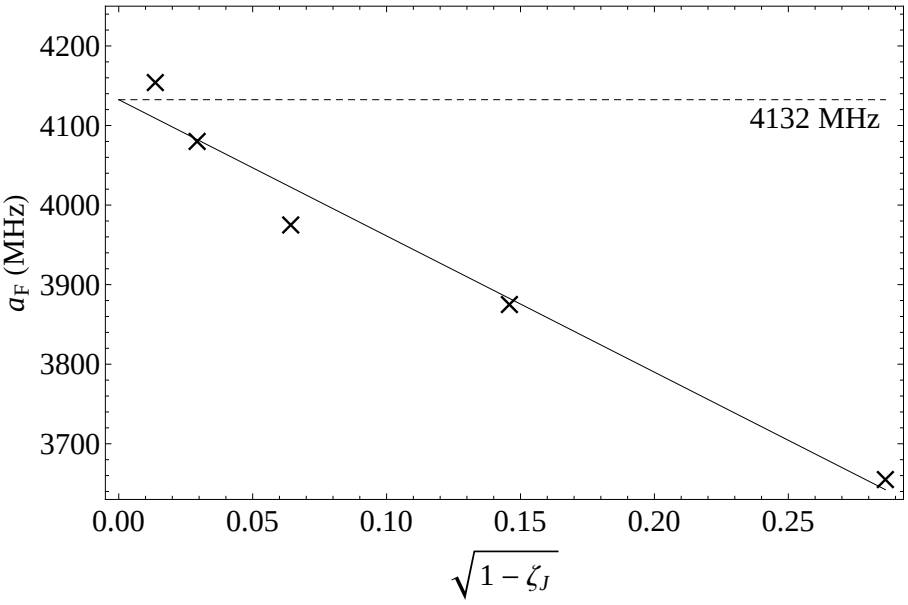

Figure 3.9: Extrapolating to an unperturbed value of a_{F}.

from the mean by ~150 MHz, however this did not significantly affect the values of a_{F} obtained.

Having calculated the mixing fractions associated with the different excited state rotational levels, the effects of the perturbation can in principle be removed to arrive at a single unperturbed value of the a_{F} hyperfine parameter for the $\mathrm{C}\,^1\Pi$, $v = 0$ vibronic state. One approach is to average over the apparent hyperfine parameters for the R(0)–R(4) lines, $a_{\mathrm{F}}^{\mathrm{R}(J)}$, scaled by the experimentally-derived mixing fractions,

$$\begin{aligned} a_{\mathrm{F}} &= \frac{1}{5}\sum_{J=0}^{4}\frac{a_{\mathrm{F}}^{\mathrm{R}(J)}}{\zeta_J}, \\ &= 4034(84)\ \mathrm{MHz}. \end{aligned} \tag{3.27}$$

An alternative deperturbation procedure is based on a plot of the apparent hyperfine parameter against the mixing fraction, extrapolating the curve to a mixing fraction

of unity. Making the transformation, $\zeta \rightarrow \sqrt{1-\zeta}$, and using a linear extrapolation results in a value, a_{F} = 4132(25) MHz as shown in figure 3.9. The extrapolation method appears to be more robust and therefore that is the value listed in table 3.3 below. Both of these results rely upon the assumption that B $^1\Sigma^+$, v = 29 is the only vibronic state to mix with the C $^1\Pi$, v = 0 levels included in the study, an assumption that seems justified by the congruence between the J-dependence of $a_{\mathrm{F}}^{\mathrm{R}(J)}$ and ζ_J as illustrated in figure 3.10.

For comparison, note that the $a_{\mathrm{F}}^{\mathrm{Q}(1)}$ parameter, for which no perturbation is expected due to symmetry considerations, takes the value 4344(150) MHz. Although this is in reasonable agreement with both of the R-branch derived values, it is significantly closer to the latter. The imperfect agreement may be attributable to the presence of minor-additional heterogeneous perturbations with states such as the b $^3\Pi$ state discussed by Douglas and Greening [74].

3.5 Comparison with results from the literature

From equation 3.12, the a_{F} hyperfine parameter is proportional to $\langle r^{-3} \rangle_{1\pi}$, where r is measured from the fluorine nucleus[7]. Spectroscopic determination of a_{F} thus provides an experimental measurement of the radial distribution of the unpaired electron contributing to the hyperfine energy. To the best of the author's knowledge, there are no other measurements or calculations of a_{F} in the C-state of HF available in the literature. There are, however, a number of values available for related parameters in other species. The 4σ valence electron in the C-state is most likely to be found far from the molecular-ion core, so the value for a_{F} should approximately match that for

[7]The ^{19}F nuclear g-factor is +5.25774 [75].

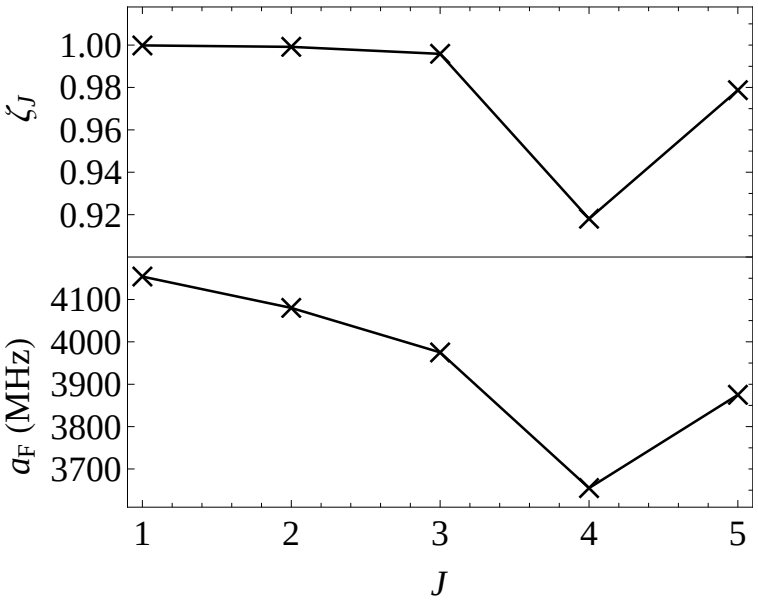

Figure 3.10: Congruent variation of the mixing fraction (upper panel) and the apparent value of the a_{F} hyperfine parameter (lower panel).

the ground state of HF^+. Similarly, because the 1π molecular orbitals are composed almost entirely of the fluorine $2p_{x,y}$ atomic orbitals, the value for $\langle r^{-3}\rangle_{1\pi}$ should be close to $\langle r^{-3}\rangle_{2\mathrm{p}}$ for the ground state of F^+.

A number of theoretical and experimental approaches have been used to obtain comparable parameters for HF^+, with the results listed in table 3.3. A many-body perturbation theory analysis of diatomic hyperfine constants by Kristiansen and Veseth [63] found a complete set of magnetic hyperfine parameters, allowing a comparison of the electron charge and spin distributions because $a/(d + c/3) \equiv \langle r^{-3}\rangle_{\mathrm{orb.}}/\langle r^{-3}\rangle_{\mathrm{spin}}$. Complete sets of parameters were obtained experimentally by Coe *et al.*[76] using laser absorption spectroscopy, and Allen *et al.* [77] using far-infrared laser magnetic resonance spectroscopy. A more recent theoretical work by Bruna and Grein [78] used density functional theory to obtain only the spin-dipole parameters, c and d, from which the a-parameter can be inferred assuming that $\langle r^{-3}\rangle_{\mathrm{orb.}} \approx \langle r^{-3}\rangle_{\mathrm{spin}}$.

Table 3.3: Comparing the values of a_{F} and $\langle r^{-3} \rangle$ in HF with equivalent values from HF^+ and F^+ provided by other authors.

Species	Term	a_{F} (MHz)	$\langle r^{-3} \rangle$ ($\mathrm{\AA}^{-3}$)	Reference
HF	C $^1\Pi$	4132(25)	55.59	This work
HF^+	X $^2\Pi$	3957.87	53.2430	[63]
HF^+	X $^2\Pi$	3850(31)	51.79	[76]
HF^+	X $^2\Pi$	3985.81	53.619	[77]
HF^+	X $^2\Pi$	4164(15)	56.02	[78]
F^+	^{3}P	–	56.7455	[79]

As expected, the value of $\langle r^{-3} \rangle_{\mathrm{orb.}}$ for the 1π orbital in HF is broadly in agreement with the corresponding value for an orbital in the 2p subshell of F^+. This parameter was obtained by combining the magnetic resonance spectroscopy derived value for the A_J atomic hyperfine parameter measured by Brown *et al.* [80] with the $\langle r^{-3} \rangle_{\mathrm{spin}}$ and $|\psi(0)|^2$ parameters calculated using a polarization wave function approach by Schaefer and Klemm [79]. This correspondence is good evidence for the validity of the electron configurations assumed in this work.

Chapter 4

Ionic–Covalent Coupling in Alkali–Alkali Collisions

At large bond-lengths the potential energy curves for diatomic molecular electronic states, such as the X-, B- and C-states of HF discussed in chapter 3, asymptote to the energy of the separated atoms in particular atomic states, providing a direct link between the supposedly disparate fields of atomic collision theory and molecular spectroscopy. At intermediate- to long-ranges the form of the potential energy is given by the LeRoy–Bernstein expansion based on multipole expansions describing the charge distribution in each atom [81], while at shorter ranges the overlap of the electron clouds gives rise to covalent bonds supporting the familiar diatomic vibrational levels. Coexisting with the relatively flat long-range asymptotes of these covalently bound states is another potential energy curve with the long-range attractive nature characteristic of the $-1/R$ Coulombic potential energy. A molecule on this curve has an ionic bond and can dissociate to form a cation–anion pair.

The non-crossing rule of Wigner and von Neumann states that the eigenenergies

of states of a diatomic with the same symmetry character cannot intersect [82], and that consequently two such states approaching one another as the bond-length changes will undergo an *avoided crossing*. A classic example of this behaviour is an avoided crossing between the ionic and covalent curves described above, which can lead to charge exchange during the collision of two neutral atoms or the neutralization of a cation–anion pair,

$$A^* + B \longleftrightarrow A^+ + B^-. \tag{4.1}$$

The ionic and covalent states are diabatic states of the colliding pair, so-called because in the limit of a fully diabatic process (the sudden approximation) their is no time for charge exchange and the system retains its initial configuration. The eigenstates of the Hamiltonian are the adiabatic states of the system, so-called because in the limit of a fully adiabatic process the system can adapt its configuration during the collision, resulting in charge exchange.

In addition to ion-pair production and neutralization [83], adiabatic charge transfer is important in many other chemical processes such as collisional excitation and quenching [84], chemi-ionization [85] and chemi-luminescence [86].

Atomic units are used throughout this chapter except where explicitly stated otherwise[1].

[1]Atomic units: Ry = 1/2, $m_e = 1$, $a_0 = 1$, $\hbar = 1$, $\varepsilon_0 = 1/(4\pi)$, $c = 1/\alpha \approx 137$ [87].

4.1 Calculating diabatic couplings – theory

The key requirement for calculating diabatic-transition rates (traversing an avoided crossing with no change in character) and cross-sections for charge-exchange processes is the determination of the coupling energies in the diabatic Hamiltonian matrix. With the completion of this step, further calculation of system properties, using dynamical approximations such as the Landau–Zener [88], Rosen–Zener [89] or Landau–Teller methods [90], or the generally more precise numerical solutions of the system's equations of motion, presents a relatively modest challenge.

At large internuclear distances the ionic and covalent diabatic molecular wave functions retain the character of their atomic progenitors, and further, in the limit of negligible electron–electron correlations these atomic states can be represented by products of one-electron atomic orbitals centred on their respective nuclei. This approach is known as the *asymptotic approximation* [91].

Throughout the present work the donor atom, A, is always taken to be an alkali metal, and so its cation, A^+, has a closed-shell electronic configuration that is neglected in the calculation except insofar as it is responsible for the quantum defect included in the valence orbital of the A-atom. Consequently, the spatial component of the molecular ionic wave function consists solely of a product of two identical valence orbitals on the B^- anion with a necessarily antisymmetric spin component. In the limit of LS-coupling, the electric dipole selection rules do not couple states with different spin ($\Delta S = 0$) and hence the covalent spatial wave function must be a symmetric combination of the A- and B-atom valence orbitals. In terms of the atomic

basis states, the two wave functions are given by,

$$|\psi_{\rm i}\rangle = |b'\rangle_1|b'\rangle_2, \tag{4.2}$$

$$|\psi_{\rm c}\rangle = \frac{1}{\sqrt{2}}\Big(|a\rangle_1|b\rangle_2 + |a\rangle_2|b\rangle_1\Big), \tag{4.3}$$

where $|\psi_{\rm i}\rangle$ and $|\psi_{\rm c}\rangle$ represent the ionic and covalent states respectively, $|a\rangle$ is the valence orbital on the A-atom originally occupied by the transferred electron, $|b\rangle$ is the occupied valence orbital of the neutral B-atom prior to the transfer, and $|b'\rangle$ is the valence orbital of the B^- anion. For heavier atoms the assumption of spatial symmetry in the covalent state may be a poor approximation[2]. Using these expressions the overlap of the covalent and ionic states can be obtained,

$$\begin{aligned} S =& \langle\psi_{\rm c}|\psi_{\rm i}\rangle \\ =& \frac{1}{\sqrt{2}}\left(\langle b|b'\rangle_1\langle a|b'\rangle_2 + \langle b|b'\rangle_2\langle a|b'\rangle_1\right) \\ =& \sqrt{2}\langle b|b'\rangle\langle a|b'\rangle, \end{aligned} \tag{4.4}$$

where in general S implicitly depends on R due to the factor of $\langle a|b'\rangle$.

For energetically well-separated covalent asymptotes a 2×2 diabatic Hamiltonian matrix can be constructed for each asymptote using a basis consisting of the ionic state and just a single covalent state,

$$\underline{\underline{\mathcal{H}}} = \begin{pmatrix} \mathcal{H}_{\rm ii} & \mathcal{H}_{\rm ic} \\ \mathcal{H}_{\rm ci} & \mathcal{H}_{\rm cc} \end{pmatrix}, \tag{4.5}$$

[2]See reference [92], page 57.

where $\mathcal{H}_{jk} = \langle\psi_j|\hat{\mathcal{H}}|\psi_k\rangle$ and $\hat{\mathcal{H}}$ is the Hamiltonian operator excluding the nuclear kinetic energy. In the following it is assumed that $\underline{\underline{\mathcal{H}}}$ is a symmetric matrix, and hence $\mathcal{H}_{jk} = \mathcal{H}_{kj}$.

The Hamiltonian operator for this system is given by,

$$\hat{\mathcal{H}} = \underbrace{-\sum_{i=1}^{N}\left(\frac{\nabla_i^2}{2} + \frac{1}{r_{b,i}}\right) + \sum_{i>j}\frac{1}{r_{ij}}}_{\hat{\mathcal{H}}_0} + \underbrace{\frac{1}{R} - \sum_{i=1}^{N}\frac{1}{r_{a,i}}}_{\hat{V}}, \tag{4.6}$$

where $r_{a,i}$ and $r_{b,i}$ are the radial distances of the i^{th} electron from the A and B nuclei respectively, and N is the total number of valence electrons from the two colliding species. For alkali atoms with their single valence electron, and in fact more generally [93], only the two orbitals involved in the electron transfer contribute significantly to the coupling energy, and hence it is appropriate to set $N = 2$.

Since $\hat{\mathcal{H}}_0|\psi_{\text{i}}\rangle = \varepsilon_{\text{i}}|\psi_{\text{i}}\rangle$ and $\varepsilon_{\text{i}}(R_{\text{c}}) = \varepsilon_{\text{c}}(R_{\text{c}}) = -1/R_{\text{c}}$ (zero taken to be the separated ion-pair limit), the $\hat{\mathcal{H}}_0$ and $+1/R$ contributions to $\mathcal{H}_{\text{ic}}$ cancel at the crossing, being equal to $\mp S/R_{\text{c}}$ respectively. The diabatic states are therefore coupled only by that part of the Hamiltonian representing the potential energy of the two electrons involved in the transfer, experiencing the potential due to the ion-core of the donor atom,

$$\begin{aligned}
\mathcal{H}_{\text{ic}} = V_{\text{ic}} &= \frac{1}{\sqrt{2}}\Big(\langle b|_2\langle a|_1 + \langle b|_1\langle a|_2\Big)\left(-\frac{1}{r_{a,1}} - \frac{1}{r_{a,2}}\right)\Big(|b'\rangle_1|b'\rangle_2\Big) \\
&= -\frac{1}{\sqrt{2}}\Big[\langle a|\frac{1}{r_a}|b'\rangle_1\langle b|b'\rangle_2 + \langle b|\frac{1}{r_a}|b'\rangle_1\langle a|b'\rangle_2 \\
&\qquad + \langle a|\frac{1}{r_a}|b'\rangle_2\langle b|b'\rangle_1 + \langle b|\frac{1}{r_a}|b'\rangle_2\langle a|b'\rangle_1\Big] \\
&= -\sqrt{2}\Big(\langle b|b'\rangle\langle a|\frac{1}{r_a}|b'\rangle + \langle a|b'\rangle\langle b|\frac{1}{r_a}|b'\rangle\Big).
\end{aligned} \tag{4.7}$$

Under the asymptotic approximation it can be assumed that $1/r_a$ is slowly varying around the B-nucleus and equal to $1/R$. The expression for $\mathcal{H}_{\rm ic}(R_{\rm c})$ can therefore be simplified using the approximations, $\langle b|r_a^{-1}|b'\rangle \approx \langle b|b'\rangle/R_{\rm c}$ and $\langle b'|r_a^{-1}|b'\rangle \approx R_{\rm c}^{-1}$, giving,

$$\mathcal{H}_{\rm ic}(R_{\rm c}) = -\sqrt{2}\langle b|b'\rangle\langle a|\frac{1}{r_a} + \frac{1}{R_{\rm c}}|b'\rangle. \tag{4.8}$$

The eigenvalues of a 2×2 matrix are invariant with respect to a change in the sign of the off-diagonal elements, so the sign of $\mathcal{H}_{\rm ic}$ is unimportant.

In place of the diabatic coupling energy, $\mathcal{H}_{\rm ic}(R_{\rm c})$, many authors choose to provide the closely-related splitting of the adiabatic potential energy curves at the crossing, $\Delta V(R_{\rm c})$. This quantity can be obtained from the difference between the two solutions of the full secular equation for the Hamiltonian matrix at $R = R_{\rm c}$. The full secular equation for non-orthogonal diabatic basis states can be obtained by projecting each of the diabatic states onto the full state vector,

$$\langle\psi_{\rm i}|\hat{\mathcal{H}}|\psi\rangle = c_{\rm i}\mathcal{H}_{\rm ii} + c_{\rm c}\mathcal{H}_{\rm ic} = c_{\rm i}E + c_{\rm c}ES \tag{4.9}$$

$$\langle\psi_{\rm c}|\hat{\mathcal{H}}|\psi\rangle = c_{\rm i}\mathcal{H}_{\rm ci} + c_{\rm c}\mathcal{H}_{\rm cc} = c_{\rm i}ES^* + c_{\rm c}E, \tag{4.10}$$

then rearranging to form a matrix equation and taking the determinant in the usual manner,

$$\begin{vmatrix} \mathcal{H}_{\rm ii} - E & \mathcal{H}_{\rm ic} - ES \\ \mathcal{H}_{\rm ci} - ES^* & \mathcal{H}_{\rm cc} - E \end{vmatrix} = 0. \tag{4.11}$$

Taking the limit,

$$\lim_{R\to R_{\rm c}} \mathcal{H}_{\rm ii} = \mathcal{H}_{\rm cc}, \tag{4.12}$$

and using the binomial approximation this becomes,

$$\Delta V(R_c) = \frac{2(\mathcal{H}_{ic} - \mathcal{H}_{ii}S)}{1 - S^2}. \tag{4.13}$$

The $\hat{\mathcal{H}}_0$ and $+1/R$ contributions to $\mathcal{H}_{ii}$ cancel, being equal to $\mp 1/R_c$ respectively, giving a simplified form for the adiabatic splitting,

$$\Delta V(R_c) = \frac{2(V_{ic} - V_{ii}S)}{1 - S^2}. \tag{4.14}$$

The diagonal element, V_{ii}, can be obtained in the now familiar manner,

$$\begin{aligned} V_{ii} =& \langle b'|_1 \langle b'|_2 \left(-\frac{1}{r_{a,1}} - \frac{1}{r_{a,2}} \right) |b'\rangle_1 |b'\rangle_2 \\ =& -2\langle b'|\frac{1}{r_a}|b'\rangle. \end{aligned} \tag{4.15}$$

Again utilizing the assumptions about the nature of $1/r_a$ near the B-nucleus, a simple form is obtained, $V_{ii} = -2/R_c$, from which the final form for the adiabatic splitting is obtained,

$$\Delta V(R_c) = \frac{2^{3/2}}{1 - S^2} \langle b|b'\rangle \langle a|\frac{1}{r_a} - \frac{1}{R_c}|b'\rangle. \tag{4.16}$$

Note that in the limit of fully orthogonal diabatic states the adiabatic splitting is trivially related to the diabatic coupling energy,

$$\lim_{S \to 0} \Delta V(R_c) = 2\mathcal{H}_{ic}. \tag{4.17}$$

For crossings at long-range the covalent curve, arising from short-range interactions, can be taken to be flat and hence the crossing bond-length can be found simply

by equating the binding energies of the two states,

$$\mathrm{EA_B} + \frac{1}{R_\mathrm{c}} = \mathrm{IP_A}(n\ell), \tag{4.18}$$

where $\mathrm{IP_A}(n\ell)$ is the ionization energy of atom A in state $n\ell$ and $\mathrm{EA_B}$ is the electron affinity of atom B.

Cast in this form, the problem of calculating $\mathcal{H}_\mathrm{ic}$ for a given molecular system becomes the problem of finding suitable forms for the orbitals of interest. Because $|b\rangle$ and $|b'\rangle$ are orbitals within a ground-state configuration, the radial functions, $R_b(r_b)$ and $R_{b'}(r_b)$ can be obtained numerically via the Hartree-Fock method. The excited-state valence orbital for the donor atom in general presents a greater challenge. In many cases electron–electron correlations are important and factorization into radial and angular functions is an unacceptably crude approximation. For alkali atoms, as considered in this work, with a single valence electron about a closed-shell core, the correlations are sufficiently weak that the concept of separate radial and angular wave functions can be retained.

There now follows a discussion of the forms of the wave functions to represent the $|a\rangle$, $|b\rangle$ and $|b'\rangle$ orbitals in calculating the coupling using equations 4.8 and 4.16.

4.1.1 Ground-state valence orbitals, $|b\rangle$ and $|b'\rangle$

Hartree-Fock orbitals for the ground state configurations of the atoms He → Xe, cations $Li^+ \rightarrow Cs^+$ and anions $H^- \rightarrow I^-$ are published as tables [94, 95] in the convenient analytic form developed by Roothaan [96]. The Hartree-Fock method assumes that electron–electron interactions can be well described by a spherically symmetric mean-field potential, maintaining the separability of the Schrödinger equation into a radial

part with eigenfunctions as listed in the aforementioned references and and an angular part with the set of spherical harmonics as eigenfunctions.

The results presented in this chapter include calculations for all alkali–alkali donor–acceptor combinations excluding Cs as an acceptor due to the absence of anion wave functions with $Z > 53$ in the literature (also excluding francium which is unstable with a half-life of less than 22 minutes [75]).

Roothaan-type wave functions fit an analytic function to the numerical Hartree-Fock results, using an expansion of Slater-type radial basis functions that take the form,

$$\chi_{n\ell p} = \frac{(2\zeta_{\ell p})^{n+1/2}}{\sqrt{(2n)!}} r^{n-1} e^{-\zeta_{\ell p} r}, \tag{4.19}$$

where n and ℓ are the principle quantum number and orbital angular momentum quantum number respectively, p is the basis function index and $\zeta_{\ell p}$ is the effective nuclear charge accounting for shielding by the core electrons. The radial wave function for an $n\ell$ orbital is a linear combination of the basis functions,

$$R_{n\ell}(r) = \sum_p c_{n\ell p} \chi_{n\ell p}, \tag{4.20}$$

and the complete wave function is the product of this radial function and the spherical harmonic of degree ℓ and order m,

$$\psi_{n\ell m}(r, \theta, \phi) = R_{n\ell}(r) Y_\ell^m(\theta, \phi). \tag{4.21}$$

The wave functions, $\psi_{n\ell m}$, represent the functional forms of the Hilbert-space vectors, $|b\rangle$ and $|b'\rangle$, for the B-atom and B^--anion respectively, and are distinct only in the radial components, $R_b(r_b)$ and $R_{b'}(r_b)$.

4.1.2 The donor's excited-state valence orbital, $|a\rangle$

The calculation of orbitals of an excited-state configuration in general represents a much greater challenge than for their ground state cousins. In general, a mean-field representation of the electron–electron correlations is a poor approximation, precluding factorization of the wave function into radial and angular components. For alkali atoms, however, with a single valence electron about a closed-shell core, a particular form for the radial function based on a truncated expansion for the Whittaker W-function was suggested by Bates and Damgaard [97],

$$R_a(r) = Ne^{-r/n^*} \sum_{t=0}^{\lfloor n^* \rfloor} a_t r^{n^*-t-1}, \tag{4.22}$$

where $n^* = n - \delta_{n\ell}$ is the effective principle quantum number and the experimentally determined quantum defects, $\delta_{n\ell}$, approximate the effects of polarization and penetration of the core by the valence electron[3]. The expansion coefficients, a_t, are determined by substituting equation 4.22 into the radial Schrödinger equation and equating the coefficients of powers of r to obtain the recurrence relation,

$$a_{t+1} = a_t \frac{n^*}{2t}[\ell(\ell+1) - (n^*-t)(n^*-t+1)], \tag{4.23}$$

with $a_0 = 1$. The normalization factor, based on that originally proposed by Hartree [98], is given by

$$N = \frac{2^{n^*}}{(n^*)^{n^*+1}}[\Gamma(n^*+\ell+1)\Gamma(n^*-\ell)]^{-1/2}. \tag{4.24}$$

Although Hartree only proved the functional form of this normalization constant

[3]Alkali quantum defects taken from reference [10], page 353. Note that the printed δ_0 coefficient for np levels of ^{7}Li is too large by a factor of ten (*cf.* np quantum defect noted on page 343).

for the hydrogenic case of integer n^*, numerical integration was used to confirm its validity for the cases presented herein.

Testing the excited state orbitals

As a simple test of the veracity of the excited state orbitals they have been used to calculate spin–orbit splittings in the alkalis and hydrogen for comparison with precise experimental measurements. For atoms with a single valence electron the spin–orbit Hamiltonian is given by

$$\hat{\mathcal{H}}_{\ell s} = \hat{\xi}(r)\hat{\boldsymbol{\ell}} \cdot \hat{\mathbf{s}}, \tag{4.25}$$

where $\hat{\xi}(r) = \alpha^2/(2r^3)$, giving a spin–orbit energy,

$$E_{\ell sj} = \frac{\alpha^2}{4}\langle a|r^{-3}|a\rangle_{n\ell}\left[j(j+1) - \ell(\ell+1) - s(s+1)\right], \tag{4.26}$$

and hence a spin–orbit splitting,

$$\Delta E_{\ell s} = \frac{\alpha^2}{4}\langle a|r^{-3}|a\rangle_{n\ell}\left[j_2(j_2+1) - j_1(j_1+1)\right], \tag{4.27}$$

with $j_1 = \ell - 1/2$ and $j_2 = \ell + 1/2$, giving

$$\Delta E_{\ell s} = \frac{\alpha^2}{4}\langle a|r^{-3}|a\rangle_{n\ell}\,(2\ell+1)\,, \tag{4.28}$$

Figure 4.1 shows a comparison of spin–orbit splittings calculated using the $|a\rangle$ orbitals with the corresponding NIST experimental values [99]. Reassuringly, the excited-state alkali wave functions completely agree with the measured values for hydrogen in the absence of a quantum defect. The agreement is very good for all

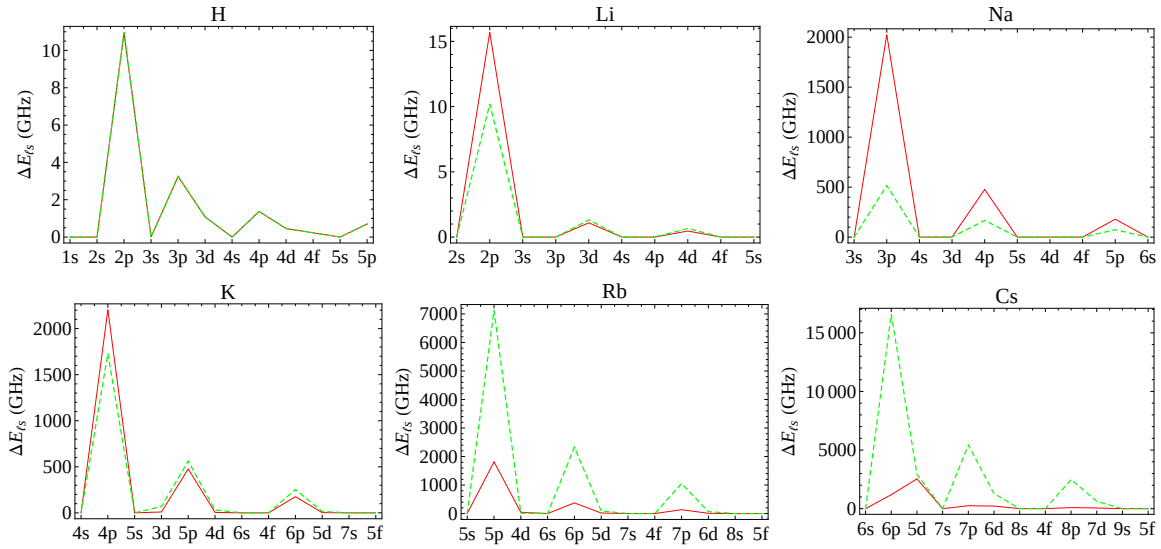

Figure 4.1: Calculated spin–orbit splittings for the group I elements up to Cs, including all states with energies below the ion-pair asymptote. The solid red line represents the calculated values, while the dashed green line shows the corresponding NIST experimental values for comparison [99]

states of Li and K, while for Na, Rb and Cs, the general form is followed but the disagreements are significant.

4.2 Testing the coupling calculations – alkali-halides

As a further test of the excited state wave functions, and more generally to test the implementation of the overall method adopted for calculating ionic–covalent couplings, a set of calculations were performed for alkali–halogen collisions for comparison with previously published results. The halogen atoms, with their large electron affinities, all play the role of the acceptor atom (B). Analyzing equation 4.18 it is clear that

only those donor atom states with a large ionization energy will fall below the ion-pair asymptote, which in most cases includes only the ground-state, although LiF, LiBr and LiI also have a single excited-state crossing. Conversely, for alkali–alkali systems there is no ionic–covalent crossing with the donor atom in its ground-state as the electron clouds of the two ions overlap before the ion-pair curve approaches the energy of the ground-state asymptote. For alkali-halide molecules, with a compact, closed shell-anion, the outer part of the ground state potential energy curve is almost entirely ionic[4].

The $|b'\rangle$ orbital is in a p-subshell of the halogen anion for which the only contribution to the diabatic coupling energy will be from the $n\mathrm{p}_0$ orbital oriented along the internuclear axis, and hence the angular part of the wave function for each $|b'\rangle$ orbital is the spherical harmonic, $Y_1^0 = \sqrt{3/(4\pi)}\cos\theta_b$. The $|a\rangle$ orbital for an alkali in its ground-state is in an s-subshell and hence the angular part of this orbital is simply $Y_0^0 = 1/\sqrt{4\pi}$. Using these identities along with the radial wave functions discussed in sections 4.1.1 and 4.1.2 the required integrals can be given explicitly as,

$$\langle b|b'\rangle = \int_0^\infty r_b^2 R_b(r_b) R_{b'}(r_b)\mathrm{d}r_b, \tag{4.29}$$

$$\langle a|b'\rangle = \frac{\sqrt{3}}{2}\int_0^\infty \int_0^\pi r_b^2 \sin\theta_b R_a(r_a) R_{b'}(r_b)\cos\theta_b \mathrm{d}\theta_b \mathrm{d}r_b, \tag{4.30}$$

$$\langle a|r_a^{-1}|b'\rangle = \frac{\sqrt{3}}{2}\int_0^\infty \int_0^\pi r_b^2 \sin\theta_b \frac{R_a(r_a)}{r_a} R_{b'}(r_b)\cos\theta_b \mathrm{d}\theta_b \mathrm{d}r_b, \tag{4.31}$$

where r_a can be expressed in terms of r_b, θ_b and R_c using the cosine rule, $r_a = \sqrt{r_b^2 + R_\mathrm{c}^2 - 2r_b R_\mathrm{c}\cos\theta_b}$.

[4]See reference [100], page 372.

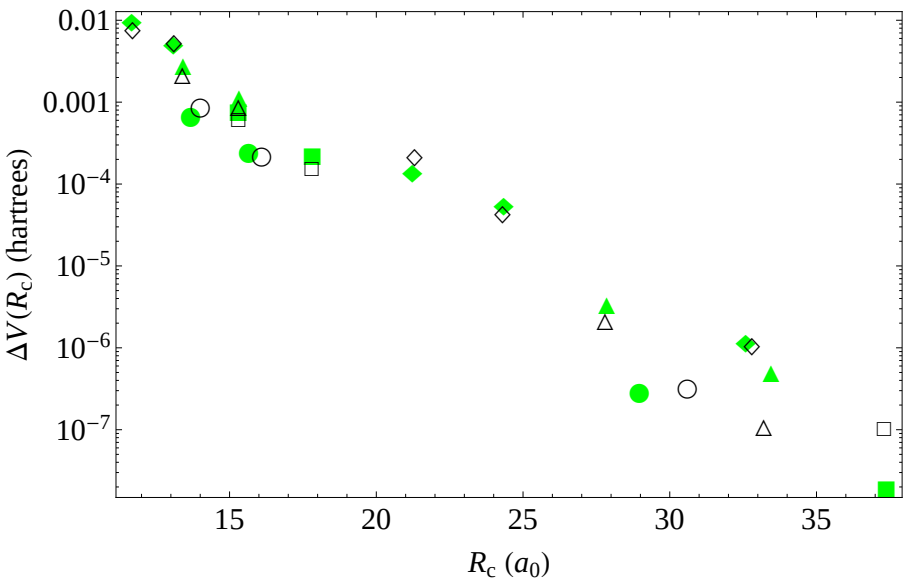

Figure 4.2: Adiabatic curve splitting in alkali-halides, showing F(○ – Li...K), Cl(□ – Li...K), Br(△ – Li...Rb) and I(◇ – Li...Cs). The crossing bond-length, R_c, increases monotonically with donor (alkali) atomic number. The empty symbols show values calculated in this work, while the filled symbols show the values of Grice and Herschbach [91, 101] for comparison.

Figure 4.2 presents calculated values of $\Delta V(R_c)$ plotted as a function of the crossing bond-length for a number of alkali-halide systems together with the results of earlier calculations by Grice and Herschbach shown for comparison [91, 101]. Overall the agreement is good, with some of the differences accounted for by significant changes in the accepted values for the halogen electron affinities since 1974 as demonstrated by the imperfect agreement in the crossing bond-lengths, R_c. The complete set of calculated values of $\Delta V(R_c)$ for alkali-halides is tabulated in appendix B.

Table 4.1: Atomic parameters used for the alkali metals: EA = electron affinity in, IP = ionization energy in the ground-state [75].

	Li	Na	K	Rb	Cs
EA (eV)	0.547926	0.618049	0.50147	0.48592	0.471626
IP (eV)	5.391719	5.139076	4.3406633	4.177128	3.893905

4.3 Alkali–alkali calculations

The ion-pair asymptotes for alkali–alkali systems are well above the molecular ground-state and hence there are numerous incoming channels that cross the ion-pair curve. The crossing bond-lengths are determined from equation 4.18 based on the acceptor electron affinities and donor ground-state ionization energies listed in table 4.1, along with excitation energies from reference [99].

The alkali anions have spherically symmetric s-subshell valence orbitals and hence the angular part of the anion wave function is constant, $Y_0^0 = 1/\sqrt{4\pi}$. The different donor atom excited-states have a range of values of ℓ, however the dominant contribution to the ionic–covalent coupling in each case is taken to be the cylindrically symmetric orbital with $m_\ell = 0$, with quantization axis chosen to lie along the internuclear axis. The resulting general form for the angular part of the donor atom wave function is given by $Y_\ell^0 = \sqrt{(2\ell+1)/(4\pi)}P_\ell(\cos\theta_a)$, where $P_\ell(\cos\theta_a)$ is the Legendre polynomial of degree ℓ centred on the A-atom.

Using this angular dependence along with the radial wave functions discussed in sections 4.1.1 and 4.1.2, the complete wave functions can be constructed in accordance

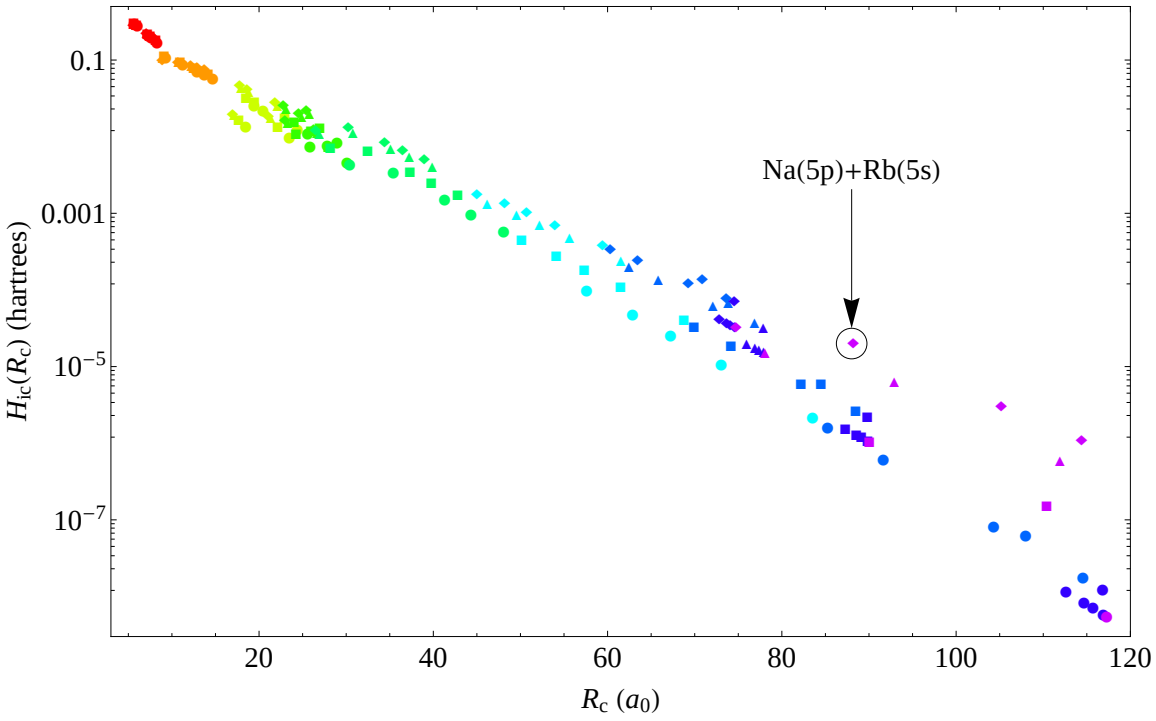

Figure 4.3: Ionic–covalent coupling energies in alkali–alkali systems, with acceptor atoms, Li(○), Na(□), K(△) and Rb(◇). The crossing bond-length, R_c, increases monotonically with donor atom atomic number, with colours denoting different donor atom states with their energies in spectral order. To give an example, the value corresponding to the Na(5d)+Rb(5s) collision is noted.

with equation 4.21 to give the required integrals for all alkali–alkali crossing channels,

$$\langle b|b'\rangle = \int_0^\infty r_b^2 R_b(r_b) R_{b'}(r_b) \mathrm{d}r_b, \tag{4.32}$$

$$\langle a|b'\rangle = \frac{\sqrt{2\ell+1}}{2} \int_0^\infty \int_0^\pi r_b^2 \sin\theta_b R_a(r_a) R_{b'}(r_b) P_\ell(\cos\theta_a) \mathrm{d}\theta_b \mathrm{d}r_b, \tag{4.33}$$

$$\langle a|r_a^{-1}|b'\rangle = \frac{\sqrt{2\ell+1}}{2} \int_0^\infty \int_0^\pi r_b^2 \sin\theta_b \frac{R_a(r_a)}{r_a} R_{b'}(r_b) P_\ell(\cos\theta_a) \mathrm{d}\theta_b \mathrm{d}r_b, \tag{4.34}$$

where as before r_a can be written $r_a = \sqrt{r_b^2 + R_c^2 - 2r_b R_c \cos\theta_b}$, and additionally, $\cos\theta_a = (R_c - r_b\cos\theta_b)/r_a$.

The resulting values of $\mathcal{H}_{ic}$ are tabulated in appendix B for the ten lowest donor

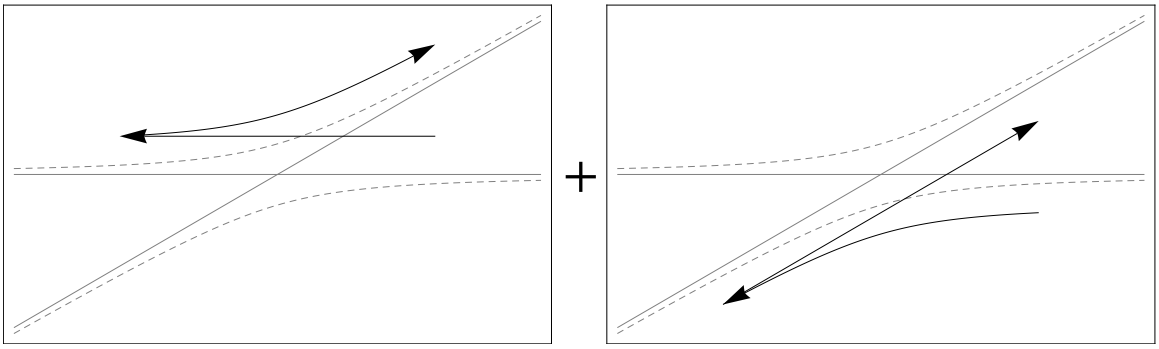

Figure 4.4: One proposed mechanism for the collisional formation of ion-pairs [102]. An incoherent sum of the two possible processes that include one diabatic and one adiabatic transition with no change in character at short range.

atom states, excluding those with $\ell \geq 4$; comprehensive listings of quantum defects are generally listed only up to the f-states. Figure 4.3 shows how the calculated couplings show a generally exponential fall-off with crossing bond-length, with the crossing bond-length increasing monotonically with donor atomic number for a given coupling energy.

4.3.1 Example cross-section calculation

As an example of how the calculated couplings can be used to obtain measurable parameters, cross-sections are obtained for a particular ion-pair production mechanism illustrated in figure 4.4 [102]. Neutral atoms colliding on the flat long-range covalent asymptote undergo one diabatic and one adiabatic traversal in total, in either order, separating as an ion-pair. This process assumes that any coupling to other states at short range can be neglected, along with any interference effects on the return to the crossing.

Calculation of the relevant probabilities is greatly simplified by the use of the commonly used Landau–Zener approximation [88] under the three assumptions that

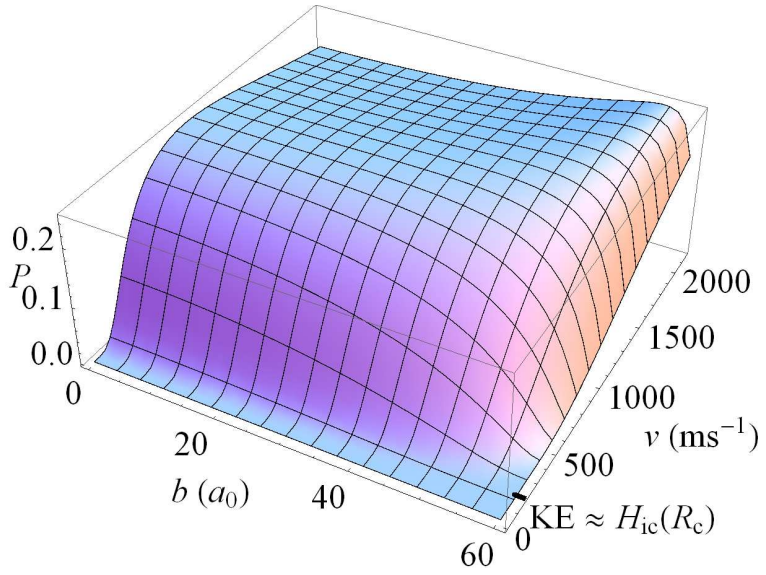

Figure 4.5: Probability for a particular mechanism for ion-pair formation in a Rb(5d)+Na(3s) collision shown as a function of relative speed and impact parameter, noting the speed at which the kinetic energy is equal to $\Delta V(R_c)/2$.

R can be treated as a well-defined classical parameter, the slopes of the diabatic potential energy curves in R are locally linear around the crossing, and that $\mathcal{H}_{ic}$ is not a function of R. Given these conditions, the probability of a single diabatic traversal is given by[5],

$$P_{ic} = \exp\left(-\frac{2\pi\mathcal{H}_{ic}^2}{v_c \Delta F}\right), \tag{4.35}$$

where $v_c = \left|\frac{dR}{dt}\right|_{R_c} = \left|\mathbf{v}\cdot\hat{\mathbf{R}}\right|_{R_c}$ is the relative radial speed at the crossing in terms of the relative velocity, $\mathbf{v}$, and ΔF is the difference between the slopes of the diabatic potential energy curves at the crossing.

[5]Reference [93] states that for non-orthogonal diabatic states $\mathcal{H}_{ic}$ should be replaced by $\Delta V(R_c)/2$. Tables of both quantities are listed in appendix B.

For a colliding pair with reduced mass, μ, the relative radial speed can be calculated as a function of the impact parameter, b,

$$v_{\mathrm{r}} = v\frac{\sqrt{R^2 - b^2}}{R}, \tag{4.36}$$

where $v_{\mathrm{c}} = v_{\mathrm{r}}(R = R_{\mathrm{c}})$. Assuming that the covalent curve is flat, the difference in slopes is easily calculated as the gradient of the ion-pair curve at the crossing,

$$\begin{aligned}\Delta F &= \frac{\mathrm{d}}{\mathrm{d}R}\left(\mathrm{IP} - \mathrm{EA} - \frac{1}{R}\right)\bigg|_{R_{\mathrm{c}}} \\ &= \frac{1}{R_{\mathrm{c}}^2}.\end{aligned} \tag{4.37}$$

The total probability for the mechanism shown in figure 4.4 can now be calculated as a function of the impact parameter and the relative speed at the crossing,

$$P(v,b) = 2P_{\mathrm{ic}}(v,b)\left(1 - P_{\mathrm{ic}}(v,b)\right). \tag{4.38}$$

Figure 4.5 shows how the probability varies as a function of these two parameters, using the Rb(5d)+Na(3s) collision to illustrate the general functional form of $P(v,b)$, and noting the speed at which the kinetic energy is equal to $\mathcal{H}_{\mathrm{ic}}$. This is an important point of reference because the first of the three conditions mentioned for the use of the Landau–Zener formula, that R can be treated as a well-defined classical variable, is equivalent to a requirement that the kinetic energy be much greater than $\mathcal{H}_{\mathrm{ic}}$.

The total cross-section for the charge-transfer mechanism can be obtained by integrating over the impact parameter out to the maximum value for which a transition

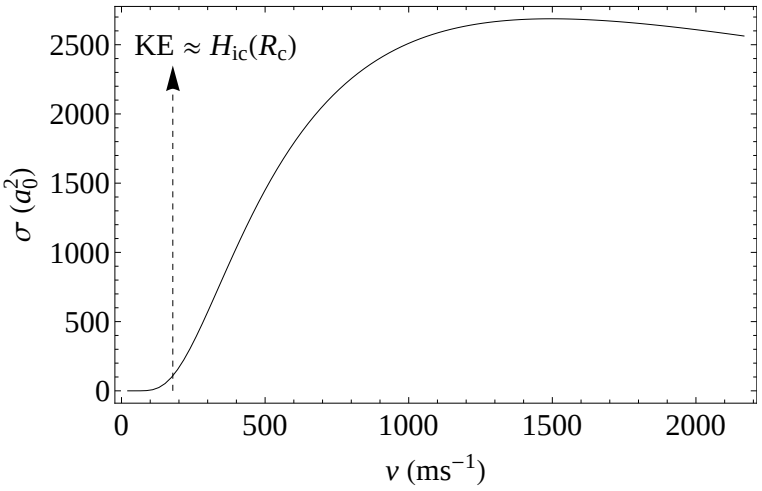

Figure 4.6: Cross-section for a particular mechanism for ion-pair formation in a Rb(5d)+Na(3s) collision shown as a function of relative speed, noting the speed at which the kinetic energy is equal to $\Delta V(R_c)/2$.

can occur, the crossing bond-length,

$$\sigma(v) = \int_0^{R_c} 2\pi b P(b,v) \mathrm{d}b. \tag{4.39}$$

Figure 4.6 shows how this cross-section varies as a function of relative speed for an Rb(5d)+Na(3s) collision.

Chapter 5

The Magneto-Optical Trap – Theory

The large thermal kinetic energy in atomic systems at room temperature obscures their quantum nature due to the broad range of internal energies of the constituent atoms. The development of the magneto-optical trap (MOT) in the mid-1990s [103] provided a reliable means for producing populations of certain classes of atom at sub-mK temperatures, maintained for periods that are long compared with typical atomic beam experiments.

This concept utilized the technique of laser-cooling, whereby the kinetic energy of atoms and atomic ions, and in principle also molecules, is reduced through interaction with laser-light, and added a spatially varying magnetic field that defines a trap-centre and leads to true trapping, as opposed to simply cooling the atoms.

SI units are used throughout this and subsequent chapters except where explicitly stated otherwise.

5.1 Principles of laser cooling

Laser cooling is a technique for reducing the kinetic energy of atoms and atomic ions using momentum transfer from laser radiation. The scattering of a photon by an atom has the potential to either increase or decrease the atom's kinetic energy. The primary consideration for implementing a cooling scheme is the selective interaction of the radiation field with those atoms in a velocity class that will lead to a reduction in their kinetic energy.

The theory of laser cooling originated with Hänsch and Schawlow in 1975 [28]. They described how the Doppler effect results in radiation pressure that depends on the component of an atom's velocity along the direction of propagation of a collimated laser beam, allowing selective interaction with a particular velocity class. The effect is known as *Doppler cooling* and can be understood in the context of a simple, 2-state quantum system.

Consider a model atomic system with a ground state, $|1\rangle$, and excited state, $|2\rangle$, separated by an energy, $\hbar\omega_0$, illuminated with monochromatic laser radiation propagating in the $+z$-direction, with angular frequency, ω, in the system's rest frame. For a given detuning, $\Delta = \omega - \omega_0$, those atoms in the ground state will absorb a photon and undergo a transition to the excited state through the electric dipole interaction with a component of velocity,

$$v_z = \frac{c\Delta}{\omega}. \tag{5.1}$$

In addition to the energy obtained from the electromagnetic field, the atom will acquire linear momentum with magnitude,

$$\delta p = \frac{\hbar\omega}{c}, \tag{5.2}$$

in the direction of the photon wave-vector, $\mathbf{k}$. If this excited atom is subsequently stimulated to decay in the laser field, the acquired momentum will be returned to the field and the atom will return to its original velocity.

With a finite excited-state lifetime, τ, an atom can undergo spontaneous emission, acquiring a recoil momentum equal in magnitude and opposite in direction to the momentum of the emitted photon. After a process of many absorption–emission cycles the effects of spontaneous emission on the atom's momentum average to zero, although this process does increases the uncertainty in each of the velocity components.

A state with lifetime, τ, has a natural linewidth of $1/(2\pi\tau)$ (in frequency), which allows atoms with a range of velocities to satisfy the resonance condition. The change in the Doppler shift due to the absorption of a single photon imparting an additional recoil velocity, $\mathbf{v}_\mathrm{r}$, is given by,

$$\delta\omega = \mathbf{k} \cdot \mathbf{v}_\mathrm{r} = \frac{\hbar\omega^2}{Mc^2}, \tag{5.3}$$

where M is the atomic mass.

For any real atomic system $\delta\omega \ll \Gamma$, and therefore an atom must scatter a large number of photons to induce a change in velocity sufficient to shift the apparent frequency of the light significantly with respect to any spectral feature. Consequently, laser-cooling presents a highly non-perturbative problem [104].

The sign of $\delta\omega$ is determined by the sign of the resonant velocity, v_z, which is in turn determined by the sign of the detuning, Δ. The key requirement for laser cooling is that of red-detuning: $\omega < \omega_0 \Rightarrow \Delta < 0$. Due to the finite linewidth, atoms with any value of v_z may scatter photons, however those atoms moving towards the laser see the light shifted towards the resonance frequency, ω_0, and scatter at a higher

rate. The condition for a *reduction* in an atom's kinetic energy following *absorption* of a photon is

$$\mathbf{k} \cdot \mathbf{v} < 0, \tag{5.4}$$

where $\mathbf{k}$ is the wave-vector of the photon and $\mathbf{v}$ is the velocity of the atom.

A configuration consisting of three orthogonal pairs of counter-propagating, co-linear beams, red-detuned from a cooling transition, is known as *optical molasses* due to the retarding effect it has on atoms in the overlap region. Although optical molasses is an effective method for cooling a population of atoms, it is not defined as a trap because there is no position dependence to the applied forces and hence no attractive 'trap centre'. Figure 5.1 shows the relationship between the components of acceleration and velocity along a particular beam-axis; the retarding effect is clearly indicated by the opposite signs of the two quantities.

The theoretical minimum temperature achievable through this Doppler-cooling mechanism can be obtained by considering the rates of heating and cooling and examining them at thermal equilibrium. The rate at which kinetic energy is lost due to reduction in v_z is given by the rate of work done by the cooling beam in retarding atomic motion,

$$\left[\frac{dE}{dt}\right]_{\text{cool}} = F_z v_z. \tag{5.5}$$

The average damping force, F_z, occurs due to the absorption of photons, each with momentum of magnitude $\hbar k$, on a transition with a power-broadened Lorentzian lineshape [105],

$$F_z = \hbar k \frac{\Gamma}{2} \frac{I/I_0}{1 + I/I_0 + [2(\Delta - k v_z)/\Gamma]^2}, \tag{5.6}$$

where I is the laser intensity and I_0 is the saturation intensity, at which the transition

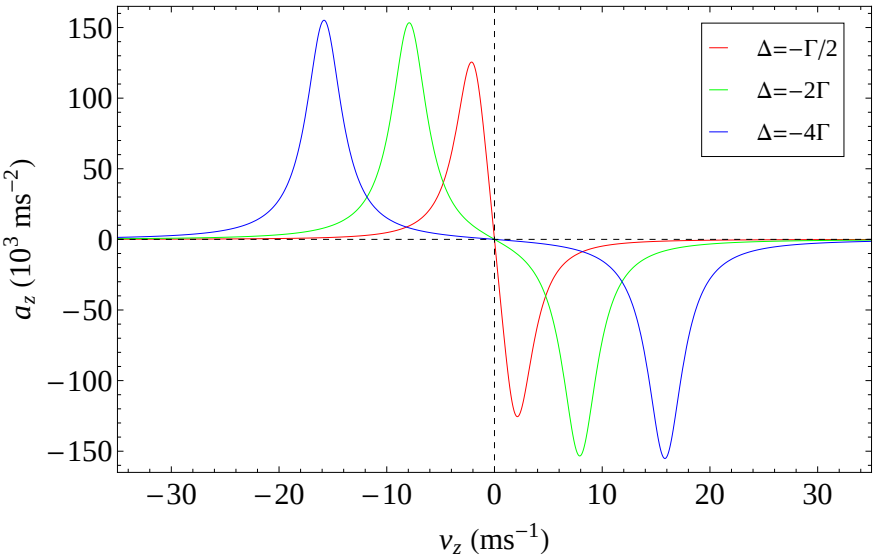

Figure 5.1: Cooling with a pair of red-detuned, counter-propagating beams oriented along the z-axis. The relationship between the axial components of acceleration and velocity is shown for three different values of the detuning, Δ, and optical fields at 10 % of the saturation intensity. Note that atoms with a positive velocity have negative acceleration and vice versa. The atomic mass, excited state lifetime and transition frequency have been chosen for the D2 line in ^{7}Li.

is broadened by a factor of $\sqrt{2}$ from the natural line-width. For a multiple beam configuration, at intensities higher than those considered here, absorption from one beam significantly reduces the ground-state population available for excitation by another beam. Under the assumption that $I \ll I_0$, the counterpropagating beams act independently and the total force along the beam axis is simply the sum of the forces from each beam. In the limit that $|kv_z| \ll \Gamma$ and $|kv_z| \ll \Delta$, the total force on an atom due to the two beams is given by [106]

$$F_z = 4\hbar k \frac{I}{I_0} \frac{kv_z(2\Delta/\Gamma)}{[1+(2\Delta/\Gamma)^2]^2}, \tag{5.7}$$

equivalent to the linear regime in figure 5.1.

Spontaneous emission causes an atom to acquire momentum equal in magnitude, in the opposite direction to the photon momentum, heating the atom. The rate of heating associated with a single axis is given by,

$$\left[\frac{dE}{dt}\right]_{\text{heat}} = \frac{\hbar^2 k^2}{2M}(2R), \tag{5.8}$$

where R is the total photon scattering rate at low intensity, given by

$$R = \Gamma \frac{I/I_0}{1 + (2\Delta/\Gamma)^2}. \tag{5.9}$$

Using the equilibrium condition,

$$\left[\frac{dE}{dt}\right]_{\text{cool}} + \left[\frac{dE}{dt}\right]_{\text{heat}} = 0, \tag{5.10}$$

an expression for $\langle v_z^2 \rangle$ can be obtained and inserted into $\frac{1}{2}k_{\text{B}}T_{\text{eq}} = \frac{1}{2}M\langle v_z^2 \rangle$ to obtain,

$$k_{\text{B}}T_{\text{eq}} = \frac{\hbar\Gamma}{4}\frac{1 + (2\Delta/\Gamma)^2}{2|\Delta|/\Gamma}. \tag{5.11}$$

The form of this function is shown in figure 5.2 using the lifetime of the $2\,^2\text{P}$ term in ^7Li. The function has its minimum value at $2\Delta/\Gamma = -1$, giving the Doppler-cooling limit,

$$T_{\text{min}} = \frac{\hbar\Gamma}{2k_{\text{B}}}. \tag{5.12}$$

A 2-level system is an ideal *cycling transition*: decay from the excited-state always leaves the system ready to absorb another photon from the cooling laser. Other decay modes from the excited state deplete the population of atoms on the cooling

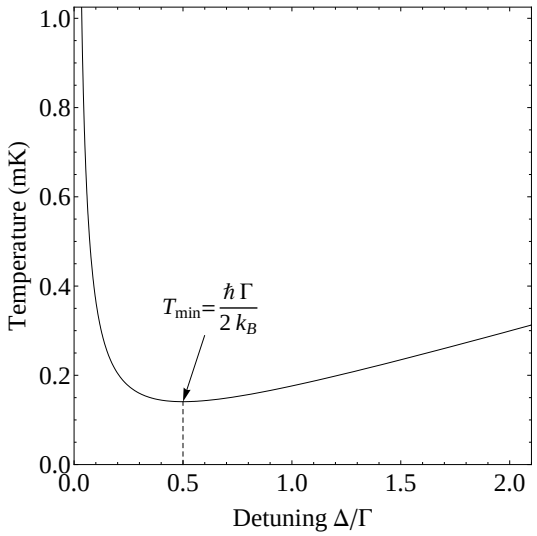

Figure 5.2: Modelled equilibrium temperature of a Doppler-cooled cloud of atoms in the limit $|kv| \ll \Gamma$ and $|kv| \ll \Delta$. The Doppler limit at $\Delta = \Gamma/2$ has been marked. Values representative of ^{7}Li have been chosen.

transition, limiting the minimum temperature achievable as each atom only undergoes a limited number of absorption–emission cycles on the cooling transition.

5.1.1 Laser cooling of ^{7}Li

For a real, multi-level atom the cooling transition must be carefully selected to meet the necessary criteria regarding accessibility to available laser systems, excited state lifetime and decay modes. For an efficient cooling system, the chosen excited state must be connected by a large electric dipole transition moment to the lower-state, with other decay-modes strongly suppressed by angular momentum selection rules.

The most abundant isotope of lithium, ^{7}Li (92.4%), has at least two separate cycling transitions that satisfy these requirements. The transition wavelengths are accessible to readily available, commercially produced diode lasers in the region around 671 nm. The $2\,^2$P term has a lifetime of approximately 27 ns [108], with $J = 1/2$

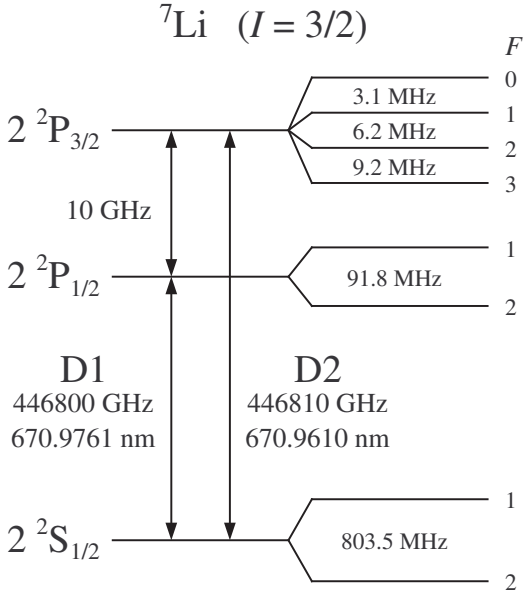

Figure 5.3: Schematic depiction of the energy levels comprising the D1 and D2 lines in ^{7}Li, including frequencies and vacuum wavelengths for both lines.

and $J = 3/2$ levels connected by large transition dipole moments to the ground $2\,^2\mathrm{S}_{1/2}$ level; transitions referred to as the D1 and D2 lines respectively.

The level scheme for ^{7}Li is shown in figure 5.3: the nuclear spin, $I = 3/2$, leads to hyperfine splitting of the J levels. The electric dipole selection rules for the total angular momentum quantum number, F, require transitions with $\Delta F \in \{0, \pm 1\}$ ($F = 0 \nrightarrow F = 0$) and $\Delta M_F \in \{0, \pm 1\}$. The D2 line hyperfine transition, $(2\,^2\mathrm{S}_{1/2}, F = 2, M_F = 2) \leftrightarrow (2\,^2\mathrm{P}_{3/2}, F = 3, M_F = 3)$, is an example of a cycling transition, so-called because the only electric dipole allowed decay from the $M_F = 3$ state is back into the ground, $M_F = 2$ state.

Because the spacing of the hyperfine components of the $J = 3/2$ level is comparable with the natural linewidth, $\Gamma/(2\pi) = 5.9$ MHz, an appreciable fraction of absorption events excite an atom into the $F = 2$ or $F = 1$ levels from where they can decay with

high probability into the ground, $F = 1$ level. Left unchecked, this mechanism would rapidly deplete the number of atoms available for cooling and hence severely limit the minimum achievable temperature. The addition of a second optical frequency component resonant with the $(2\,^2\mathrm{S}_{1/2},\, F = 1) \leftrightarrow (2\,^2\mathrm{P}_{3/2},\, F = 2)$ transition permits such lost atoms to be recycled back onto the cooling transition. The additional laser is known as a *repumping beam*.

5.2 The magnetic field: position dependent radiation force

The addition of a static quadrupole magnetic field centred on the intersection of the three beam-pairs in an optical molasses configuration results in a constant magnetic field gradient along the beam axes and an approximately constant gradient throughout the intersection region. In the absence of coupling between states, the Zeeman shift leads to a linear dependence of the eigenenergies on magnetic flux-density.

For states in a particular $(^{2S+1}L_J,\, F)$ manifold in field-free space, the states corresponding to different values of M_F are all degenerate and the polarization of the light is immaterial: the π, σ^+ and σ^- polarizations (linear along the quantization axis, right-circular and left-circular respectively) can each interact with 1/3 of the available transitions between any two states. The presence of a non-zero local magnetic field defines a space-fixed axis and breaks the degeneracy of the different angular momentum orientations described by the projection quantum number.

Conservation of angular momentum requires that the change in the total atomic angular momentum due to optical excitation corresponds precisely with that provided

by the absorbed photon, as defined by its polarization. This requirement is codified in the angular momentum selection rules that can be derived from the properties of the Wigner 3-j symbols commonly used to calculate the coupling of two angular momentum states.

For fully-polarized laser radiation absorbed through the electric dipole interaction, the relative strength of a particular transition between magnetic sub-states, $|\gamma\, F\, M_F\rangle$, and, $|\gamma'\, F'\, M'_F\rangle$, with γ representing all unspecified quantum numbers, is given by the square of the 3-j symbol,

$$\begin{pmatrix} F' & 1 & F \\ -M'_F & m & M_F \end{pmatrix}, \tag{5.13}$$

where m is zero for π polarized light and ± 1 for $\sigma^{\pm}$ polarization. The value of the 3-j symbol is identically zero unless $M'_F = M_F + m$ and $F' = F \pm 1$.

A transition between so-called *stretched states* (maximum F, maximum M_F) generally provides a good cycling transition because the electric-dipole angular momentum selection rules, $\Delta F \in \{0, \pm 1\}$, $F = 0 \nrightarrow F = 0$, and $\Delta M_F \in \{0, \pm 1\}$, suppress decay into other states.

A population of ultra-cold atoms near the potential energy minimum of a trap experiences an approximately harmonic potential leading to harmonic motion of the atoms in the trap. The oscillating atoms thus experience a time-dependent Doppler shift that periodically brings them into resonance with the cooling beams. Figure 5.4 is a schematic illustration of how the amplitude of the oscillation is reduced as momentum is lost each time the atoms pass through the resonant velocity, defined in equation 5.1 that leads to absorption from a cooling beam.

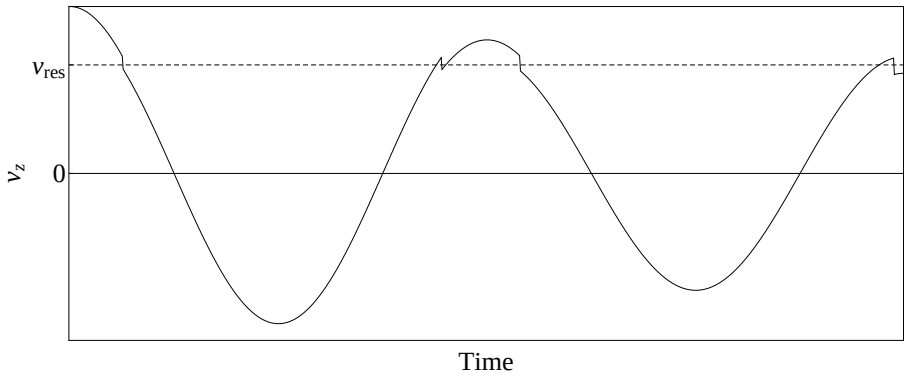

Figure 5.4: A laser-cooled atom undergoing damped harmonic motion. At a particular velocity, $v_{\text{res}} = c\Delta/\omega$, the Doppler-shift brings the light into resonance with the atomic cooling transition, reducing the velocity. Adapted from reference [104].

5.2.1 Zeeman structure in ^{7}Li

The Hamiltonian for a lithium atom in a magnetic field is given by

$$\hat{\mathcal{H}} = \hat{\mathcal{H}}_0 + \hat{\mathcal{H}}_{\text{hfs}} + \hat{\mathcal{H}}_{\text{mag}}. \tag{5.14}$$

The electronic kinetic energy and potential energy terms up to the spin–orbit coupling term are all included in $\hat{\mathcal{H}}_0$, taking E_0 as the zero point for measuring the energy of any given state, where $\hat{\mathcal{H}}_0|\psi\rangle = E_0|\psi\rangle$ for any eigenstate $|\psi\rangle$.

The different spin and orbital angular momentum terms in the magnetic hyperfine Hamiltonian discussed in chapter 3 can be compactly written [59],

$$\hat{\mathcal{H}}_{\text{hfs}} = \hat{\xi}_{\text{hfs}}(r)\hat{\mathbf{I}} \cdot \hat{\mathbf{J}}. \tag{5.15}$$

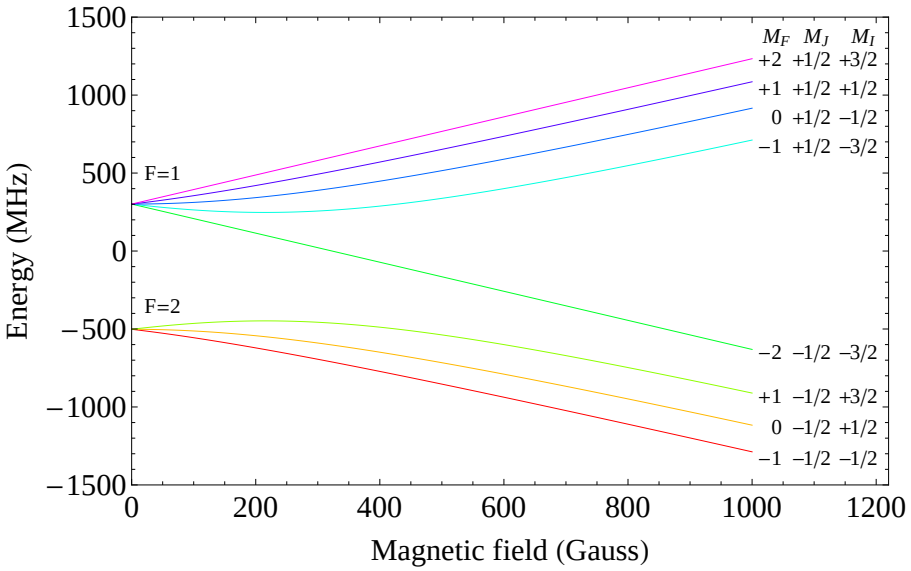

Figure 5.5: Zeeman map for the 8 states making up the $2\,^2S_{1/2}$ level in ^{7}Li. The $|F=2,\ M_F=+2\rangle$ state is the lower state of the cooling transition. Note the avoided crossings between states with the same value of M_F.

Expanding the scalar product in a spherical basis gives,

$$\hat{\mathbf{I}}\cdot\hat{\mathbf{J}} = \frac{1}{2}\left(\hat{I}_+\hat{J}_- + \hat{I}_-\hat{J}_+\right) + \hat{I}_0\hat{J}_0. \tag{5.16}$$

The magnetic Hamiltonian is given by

$$\hat{\mathcal{H}}_{\rm mag} = \left[\mu_{\rm B}\left(\hat{\mathbf{L}} + g_S\hat{\mathbf{S}}\right) + \mu_{\rm N} g_I \hat{\mathbf{I}}\right]\cdot\mathbf{B}. \tag{5.17}$$

Due to spin–orbit coupling, $\mathbf{L}$ and $\mathbf{S}$ precess around $\mathbf{J}$, with the result that L and S cease to be good quantum numbers. Using the approximation that $\hat{\mathbf{L}} + g_S\hat{\mathbf{S}} \approx g_J\hat{\mathbf{J}}$, where,

$$g_J = \frac{3}{2} + \frac{1}{2}\left[\frac{S(S+1) - L(L+1)}{J(J+1)}\right], \tag{5.18}$$

and choosing the orientation of the z-axis so that it is parallel with the magnetic field

vector gives,

$$\hat{\mathcal{H}}_{\mathrm{mag}} = \left(\mu_{\mathrm{B}} g_J \hat{J}_0 + \mu_{\mathrm{N}} g_I \hat{I}_0\right) B. \tag{5.19}$$

The matrix elements of the complete Hamiltonian can now be obtained in the uncoupled basis, $|\gamma\, J\, I\, M_J\, M_I\rangle$,

$$\begin{aligned}
&\langle\gamma'\, J'\, I'\, M'_J\, M'_I|\hat{\mathcal{H}}|\gamma\, J\, I\, M_J\, M_I\rangle = \\
&\frac{1}{2}\langle\xi_{\mathrm{hfs}}\rangle\sqrt{J(J+1) - M_J(M_J-1)}\sqrt{I(I+1) - M_I(M_I+1)}\delta_{M'_J,(M_J-1)}\delta_{M'_I,(M_I+1)} + \\
&\frac{1}{2}\langle\xi_{\mathrm{hfs}}\rangle\sqrt{J(J+1) - M_J(M_J+1)}\sqrt{I(I+1) - M_I(M_I-1)}\delta_{M'_J,(M_J+1)}\delta_{M'_I,(M_I-1)} + \\
&\left(\langle\xi_{\mathrm{hfs}}\rangle M_I M_J + g_J\mu_{\mathrm{B}} M_J B + g_I\mu_{\mathrm{N}} M_I B\right)\delta_{M_J M'_J}\delta_{M_I M'_I}.
\end{aligned} \tag{5.20}$$

Note that the Hamiltonian will couple two different states $|\psi\rangle$ and $|\psi'\rangle$ only if $M_J = M'_J \pm 1$ and $M_I = M'_I \mp 1$, and hence $M_F = M'_F$ necessarily. The effect of the coupling is most clearly visible in the avoided crossing between the two $M_F = -1$ states in the $2\,^2\mathrm{S}_{1/2}$ level shown in figure 5.5. The values of $\langle\xi_{\mathrm{hfs}}\rangle$ for the upper and lower levels of the D2 line in ^{7}Li are -3.06 MHz and 401.5 MHz respectively [109].

The eigenvalues of the Hamiltonian, being observable characteristics of the system, do not depend on the choice of basis vectors. The coupled state basis vectors, $|\gamma\, J\, I\, F\, M_F\rangle$, may be obtained by a unitary transformation from the uncoupled basis vectors, accomplished using a sum over Clebsch–Gordon coefficients,

$$|\gamma\, J\, I\, F\, M_F\rangle = \sum_{M_J\, M_I} |\gamma\, J\, I\, M_J\, M_I\rangle\langle J\, I\, M_J\, M_I|F\, M_F\rangle. \tag{5.21}$$

The eigenenergies were obtained by diagonalizing the Hamiltonian and are plotted as a function of magnetic flux density as Zeeman maps for the $2\,^2\mathrm{S}_{1/2}$ and $2\,^2\mathrm{P}_{3/2}$ levels

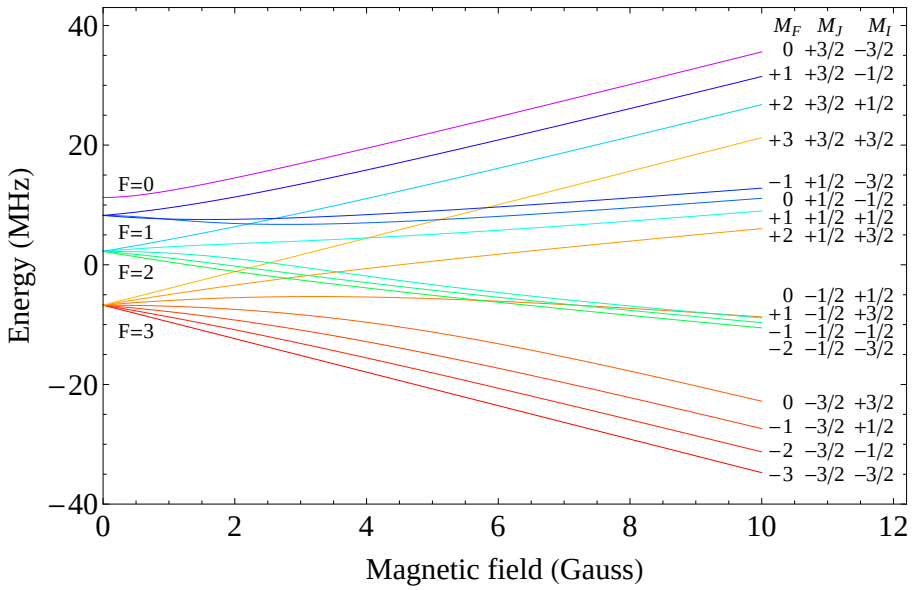

Figure 5.6: Zeeman map for the 16 states making up the $2\,^2\mathrm{P}_{3/2}$ level in ^{7}Li. The gradient of an eigenenergy is related to the magnetic moment of the corresponding state at that field; note that the gradients are correlated with M_F at low fields, while for higher fields **I** and **J** become uncoupled and the states are best labelled with M_J, a phenomenon known as the Paschen-Back effect [92]. The $|F=3,\ M_F=+3\rangle$ state is the upper state of the cooling transition.

of ^{7}Li, shown in figures 5.5 and 5.6 respectively.

The chosen cooling transition is that between states $|2\,^2\mathrm{S}_{1/2},\ F=2,\ M_F=+2\rangle$ and $|2\,^2\mathrm{P}_{3/2},\ F=3,\ M_F=+3\rangle$. This is known as a cycling transition because the electric dipole transition selection rules ($\Delta F = 0,\ \pm1$, not $0 \to 0$, and $\Delta M_F = 0,\ \pm1$) prevent decay from the upper state into any state other than the chosen lower state. Using the expressions for the eigenenergies of the relevant states we can obtain an equation for the *increase* in energy separation as a function of the magnetic field, in SI units:

$$\Delta E(B) = 1.4 \times 10^6 \hbar B. \tag{5.22}$$

5.3 The complete system

The magnetic quadrupole field in a MOT is typically provided by a pair of parallel circular coils carrying current in the opposite sense, known as anti-Helmholtz coils. The inhomogeneous magnetic field varies approximately linearly by a few gauss/cm [110], itself exerting negligible force on the population of neutral atoms. The position dependent restoring force is provided by the three pairs of counterpropagating beams with σ^+ polarization as described in section 5.1.

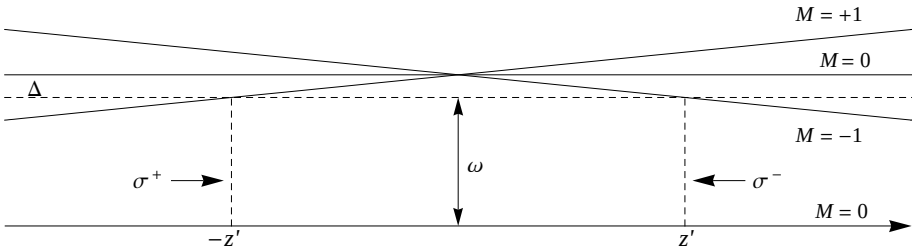

Figure 5.7: MOT transitions for an atom at rest. Counter-propagating beams of frequency ω, Δ-detuned from $M = 0 \rightarrow M = 0$ transition, with polarizations $\sigma_+(\sigma_-)$, preferentially absorbed if atom is at $-z'(+z')$.

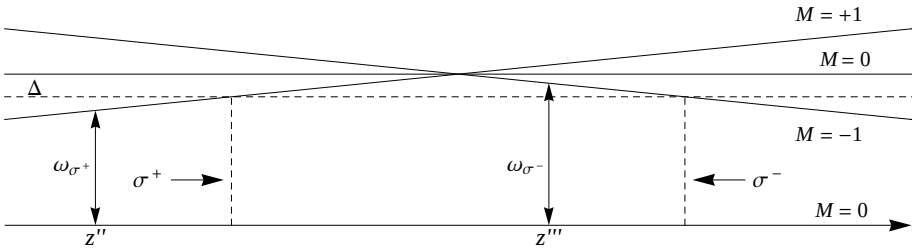

Figure 5.8: MOT transitions for an atom with $v_z > 0$. The atom sees $\sigma_+(\sigma_-)$ beam shifted to frequency $\omega_{\sigma_+} = \omega - \delta\omega(\omega_{\sigma_-} = \omega + \delta\omega)$. With $v_z = c\delta\omega/\omega$ atom may absorb from σ_+ beam if at z'', or σ_- beam if at z'''.

For a single pair of counterpropagating beams, figure 5.7 shows how an atom at rest in a MOT gets pushed towards the centre of the trap. As each state has a finite width, there is a non–zero probability that an atom anywhere in the trap will absorb

from either laser, being excited on the allowed transition for that polarization. Figure 5.8 shows how a velocity component parallel to the beam axis shifts the positions where each beam is maximally absorbed such that atoms moving away from the trap centre preferentially absorb closer to the centre. This result generalizes to the full three–dimensional case.

Results for a MOT containing ^{7}Li have been reported with approximately 2×10^9 atoms down to 300 μK.[9]

Chapter 6

The Magneto-Optical Trap – Experiment

The main challenge in the construction of the ^{7}Li MOT is the precise control of light, providing frequency-stable, coaxial cooling and repumping beams from independently tunable, single-mode, narrowband sources in the correct wavelength-range, with sufficient power. Once this requirement has been fulfilled the remaining requirements are the quadrupole magnetic field, an ultra-high vacuum system and a source of ^{7}Li atoms.

The following sections provide a detailed description of the techniques and instrumentation used to fulfill these requirements along with analysis of the performance of the different subsystems and discussion of possible enhancements and applications to planned experiments.

6.1 Light sources

The key requirements for the light sources used for the MOT are tunability while lasing on a single longitudinal mode, stability over timescales defined by the intended experiments and a linewidth narrow compared with the natural linewidth of the transitions to be addressed.

Fortuitously, a common type of red laser-diode used for laser-pointers, barcode scanners and laser printers (AlGaInP) [111] happens to lase in the spectral region around the D1 and D2 transitions in ^{6}Li and ^{7}Li close to room temperature, opening up the possibility of using these reliable, low-cost, continuous-wave (CW) sources to produce the cooling and repumping beams required for the MOT (as discussed in section 5.1.1).

The linewidth of the bare diodes are equivalent to approximately 17 natural linewidths of the ^{7}Li D2-line and, while coarse tuning with temperature or injection-current is possible, there is no tuning mechanism that can maintain single-mode operation with the necessary range, precision and response-time to be suitable for a high-bandwidth frequency-locking system. Placing the bare diode in an external cavity delimited by a diffraction grating and using frequency-selective optical feedback from the grating addresses these shortcomings, providing an additional tuning mechanism based on the angle of the grating and resulting in linewidths that can be as low as 100 kHz, a small fraction of the natural linewidth [112].

The optical setup for the MOT is based on three such external-cavity diode lasers (ECDLs) in the Littrow configuration using AlGaInP diodes that can lase in the required region around 670 nm. A brief outline of the operation of an ECDL in the Littrow configuration now follows with detailed discussion limited to those features

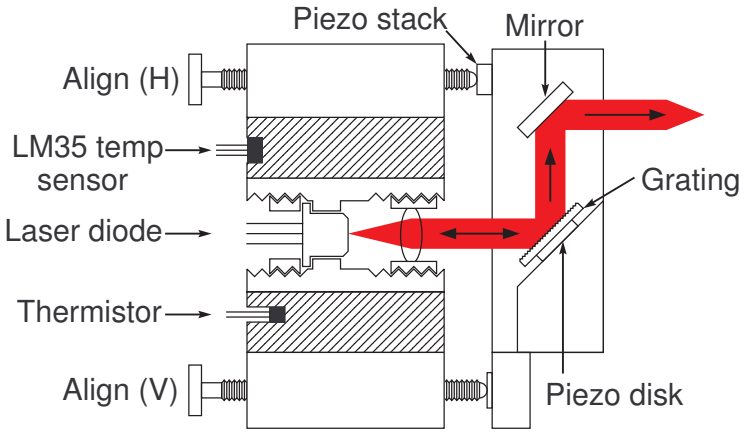

Figure 6.1: Schematic of an external cavity diode laser in the Littrow configuration, showing feedback from the diffraction grating, the two thumbscrews for vertical and horizontal alignment, and the piezo stack and disk for fine and ultra-fine frequency tuning respectively. Adapted from reference [114].

particularly relevant to their use in the MOT apparatus. For more information see references [44] and [114].

6.1.1 Diode lasers in the Littrow configuration

A diffraction grating in the Littrow configuration for a particular wavelength and diffraction order has a diffracted beam that retraces the path of the incident beam [42]. The grating equation gives,

$$m\lambda = d(\sin\theta_{\mathrm{i}} + \sin\theta_{\mathrm{d}}), \tag{6.1}$$

where m is the diffraction order, λ the optical wavelength, d the groove spacing, and θ_{i} and θ_{d} are the angles of incidence and diffraction respectively. The Littrow

configuration is equivalent to setting an incident angle,

$$\theta_{\mathrm{i}} = \sin^{-1}\left(\frac{m\lambda}{2d}\right). \tag{6.2}$$

A reflection-type, Littrow configuration ECDL directs the first-order diffracted beam back into the laser diode to seed additional amplification within a spectral range determined by the grating angle; the essential features of this arrangement are shown in figure 6.1. Light emitted from the diode is collimated by an aspheric lens into a beam incident on a gold-coated holographic reflection diffraction grating with 1800 lines/mm (Richardson Gratings, model 3399FL–330H), with approximately 63% diffraction efficiency at 670 nm [113]. The zeroth-order reflected component provides the output beam while the first-order diffracted component, with a frequency that depends on the angle of incidence, is re-injected back into the diode in a process known as self-injection locking.

The grating is mounted on a standard kinematic mirror mount with an orientation controlled using a fine-threaded thumb-screw controlling the frequency of the diffracted light, while the addition of a mirror on the same mount makes the final output beam angle independent of the orientation of the mount [114]. Between the tip of the thumb-screw and the movable platform of the kinematic mount, a piezoelectric transducer stack ('the stack') can be used for fine-tuning of the grating angle. For still finer control, a piezo-disk ('the disk') is placed between the grating and the kinematic mount. Active temperature control is achieved through the use of a MELCOR CP1.0-127-05L Peltier thermo-electric unit driven by a Wavelength Electronics MPT-5000 temperature controller connected to a 10 kΩ thermistor embedded in the laser mount. A separate LM35 temperature sensor acts as a monitor, giving a readout

in degrees Celsius.

Full details of the physics underlying the broad single-mode tuning range obtained using this simple setup are extremely subtle. Briefly, the requirement for a large tuning range is simultaneous and concomitant frequency-tuning of the populated electromagnetic mode of the external cavity (due to changing cavity length), the first-order diffracted frequency from the grating, and the active mode of the laser-diode itself. Rotating the grating about a point off the beam axis leads to simultaneous changing of the external-cavity length and the grating angle, satisfying the first two requirements. Although the mechanical length of the diode of course remains unchanged during this process, changes in the current density due to changing optical intensity within the diode cause a change in the refractive index in the diode and hence in the optical path length. A detailed analysis of this process is provided in reference [115].

6.1.2 Diode laser frequency control

Absolute measurements of the laser frequency to 1 GHz resolution were taken using a microcontroller-based travelling Michelson wavemeter constructed in the Trent Optical Physics Group [116]. Data showing the output frequency characteristics using temperature and the thumb-screw tuning are presented in figures 6.2(a) and (b) respectively.

Setting the frequency of an ECDL proceeds as follows: initially the thumb-screw is used to optimize the ECDL alignment in the Littrow configuration by minimizing the threshold injection current, following the procedure outlined in reference [119]. Subsequently the thumb-screw is used tune as close as possible to the desired frequency, recognizing that tuning away from optimal alignment reduces the single-mode tuning

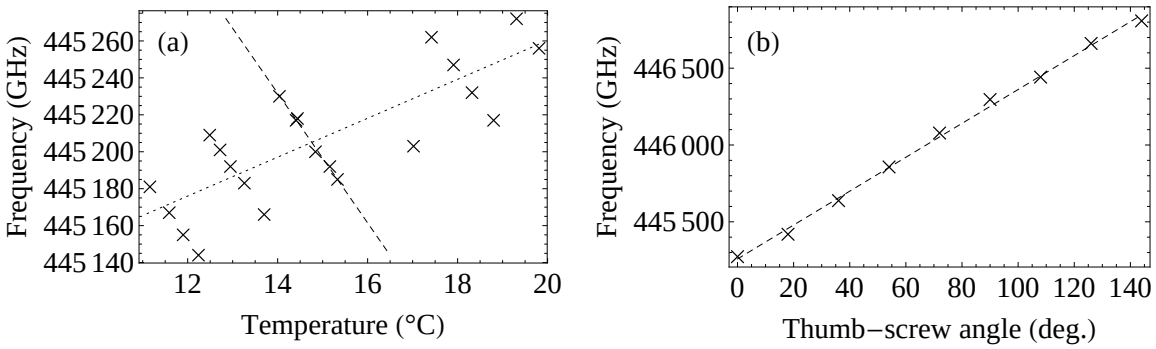

Figure 6.2: Frequency tuning a temperature stabilized ECDL. (a) Tuning only with temperature: the diode expands with increasing temperature decreasing the frequency by 35(1) GHz/°C (dashed line); mode-hops when an additional half-wavelength can be accommodated lead to an overall increase in frequency with temperature of 10(2) GHz/°C (dotted line). (b) Coarse tuning over approximately 1400 GHz by changing the angle of the grating, giving a frequency increase of 11.0(2) GHz/degree counter-clockwise thumbscrew rotation. Note that the maximum frequency reached is within 2 GHz of the ^{7}Li D2 line.

range. The local temperature tuning of -35(1) GHz/°C is used to get within 2 GHz of the desired value followed by fine-tuning with the stack.

Together these tuning mechanisms provide for high-resolution frequency control over a broad range, making these systems ideal light sources for the MOT setup. Three such ECDL systems are used in the setup: one (ECDL1 in figure 6.17) is based on a low-power Opnext (Hitachi) HL6714G diode providing ~10 mW free-running power (not in an external cavity), while the other two are based on high-power Philips CQL-806/G diodes providing ~30 mW free-running power.

6.1.3 System performance

When using ECDLs in experimental physics it is essential that one becomes intimately familiar with the properties of the lasers and control systems, both for awareness of the system's capabilities and so that deterioration of those capabilities due to aging

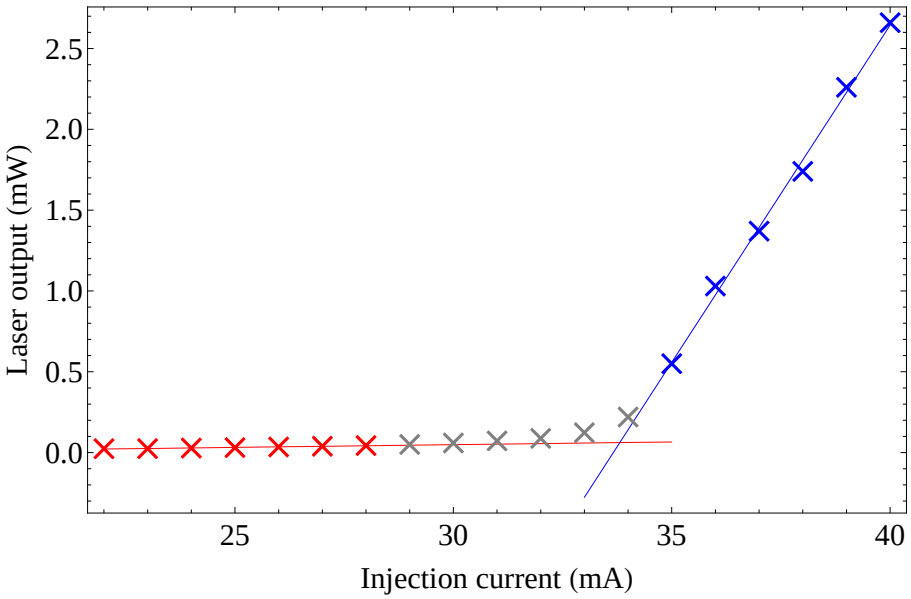

Figure 6.3: Determining the threshold current of an ECDL. The output power varies linearly with injection current both below and above threshold, with the threshold current, defined at the intersection of those two lines, at 33.8 mA. The two lines are linear fits to the respective sets of data points of the same colour.

or damage to the laser diodes can be rapidly identified.

A key parameter that varies with the grating alignment and can change dramatically as a diode ages is the threshold injection current. As the current is increased, the gain in the laser system increases, with threshold reached at the point when the gain per round-trip in the laser cavity is equal to the total round-trip losses, leading to a sudden and dramatic increase in the slope of the output power with injection current. An example data-set for determining the threshold current of an ECDL is shown in figure 6.3, showing the linear dependence of the power output on current both below and above threshold, with the threshold current defined at the intersection of the two lines.

Figure 6.4 shows a sample mode-map with lines representing single-mode frequency tuning of one of the ECDLs using a high-power laser diode. The numbers

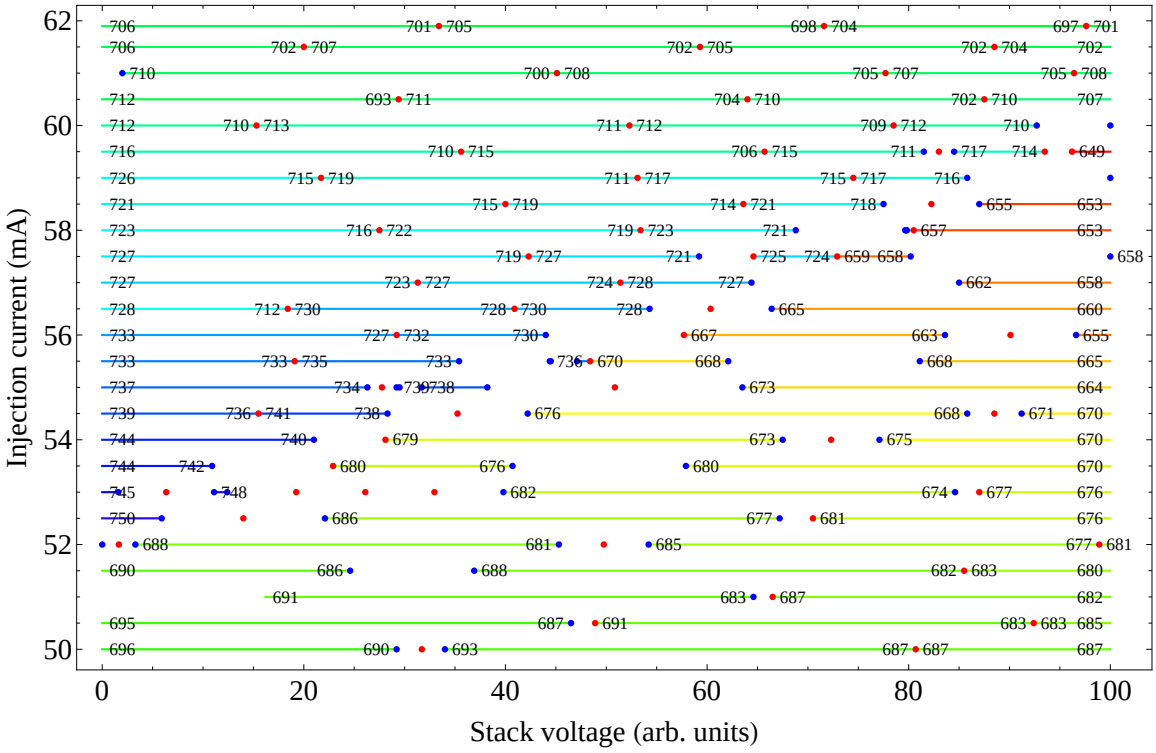

Figure 6.4: Mode-map for an ECDL with lines representing regions of single-mode operation. The numbers show the excess frequency above 446000 GHz, the blue dots represent a smooth transition between single and multi-mode behaviour, while the red dots represent discrete frequency hops.

represent the excess frequency above 446000 GHz, blue dots representing a smooth transition between single and multi-mode behaviour, and red dots representing discrete frequency hops. In general the frequency increases with decreasing stack voltage and current, and from the distribution of mode hops it is clear that maximum tuning range can be obtained by concurrently tuning current with stack voltage by about 0.1 mA/V. The data was obtained using the home-built travelling Michelson wavemeter in conjunction with a Coherent model 240 optical spectrum analyzer to confirm single-mode behaviour. Note that this data was taken for an optimally aligned ECDL;

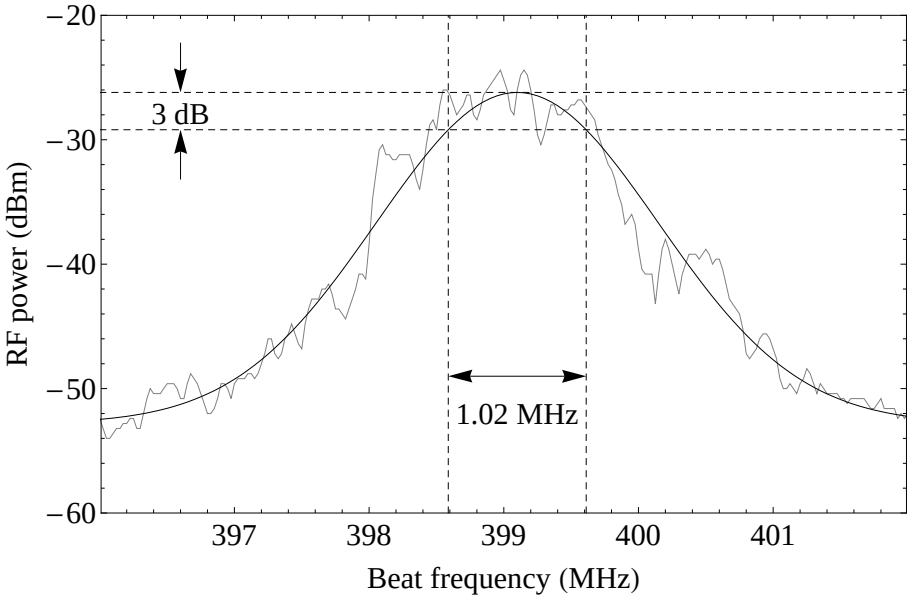

Figure 6.5: Beat-signal between a pair of ECDLs locked 400 MHz apart. The beat-signal is the convolution of the two Lorentzian lineshapes giving a Lorentzian with a width that is the sum of the two individual widths.

in general setting the required operating frequency with the thumbscrew has the effect of misaligning the external cavity, resulting in single-mode behaviour over more restricted regions of parameter-space.

An estimation of the ECDL linewidths was obtained by measuring the width of the beat-signal between an unstabilized ECDL and a second ECDL locked to the first at a fixed frequency separation. Using the locking techniques outlined in sections 6.2 and 6.3, two ECDLs were locked with a stable separation of approximately 400 MHz giving the beat-signal shown in figure 6.5, observed using a HAMEG HM5012-2 RF spectrum analyzer. On a logarithmic scale, the half-maximum point is 3 dB below the peak, at which point the width of the beat profile is approximately 1 MHz. The beat-profile is a convolution of lineshapes of the two beams, which, assuming that they approximate Lorentzians with the same width, gives a laser linewidth of

approximately 500 kHz.

6.2 Absolute laser frequency locking

Having tuned an ECDL to the appropriate operating frequency range, an automated system is required to keep the laser locked to an absolute frequency for the duration of any planned experiment. The technique employed for this task is based on the use of a narrow spectral feature at the frequency in question, in this case a hyperfine-resolved transition within the ^{7}Li D2-line. Such a system must maintain a stable lock in the face of both large-amplitude, low-frequency drifts such as those associated with diurnal temperature and humidity variations, and intermediate- to high-frequency transient noise sources such as power-line fluctuations and mechanical vibrations.

Direct measurement of frequencies in the optical range (approximately 430–750 THz) is beyond the capability of any electrical transducer. Various interferometry-based techniques are available [117], including the traveling Michelson wavemeter discussed in section 6.1.2, however none of these have the temporal or spectroscopic resolution required for a high-bandwidth frequency-locking system with sufficient accuracy.

A widely used solution for this measurement problem is based on the frequency and phase characteristics of the signal transmitted through a vapour-cell when the light source is frequency-dithered about a spectral feature (peak or dip) with a width comparable with the desired locking resolution. This approach is generally referred to as peak-locking [118] and was applied to a feature in the saturated absorption spectrum of lithium.

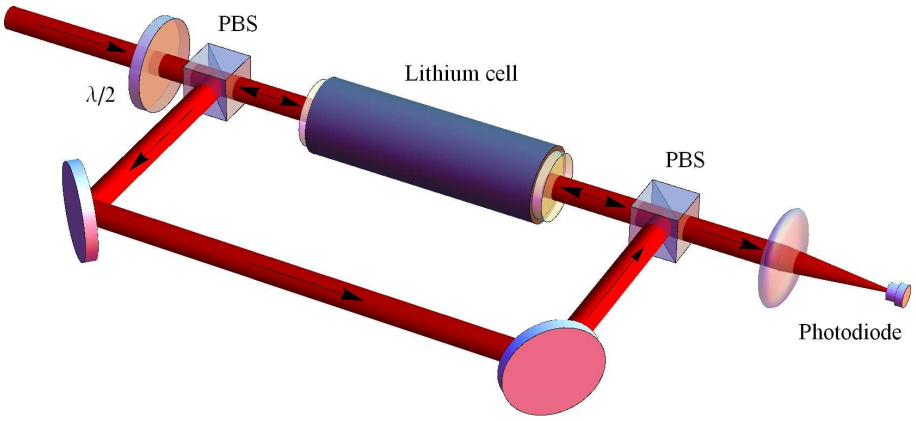

Figure 6.6: Optical layout for saturated absorption spectroscopy. A half-wave plate ($\lambda/2$) and a pair of polarizing beam-splitters (PBS) are used to obtain counter-propagating coaxial beams passing through the lithium cell with a tunable intensity ratio. The low-power, horizontally-polarized probe-beam is transmitted through each PBS and detected by a photodiode, while the high-power, vertically polarized pump-beam is reflected by each PBS.

6.2.1 Saturated absorption spectroscopy

The low vapour pressure of atomic lithium at room temperature ($\approx 10^{-19}$ mbar [75]) makes it impossible to obtain a vapour without significant heating. The lithium vapour-cell is maintained at around 650 K (vapour pressure $\approx 10^{-4}$ mbar) using a 29 Ω Thermocoax heating coil in a bifilar configuration, with an RMS AC-bias of 36 V from a Variac tunable autotransformer giving an RMS current of 1.25 A. The high temperature and concomitant spread in atom speeds broadens direct absorption spectral features to a Doppler-width of around 3 GHz, whereas ideally the frequencies of the MOT cooling and repumping beams would be set and tuned with a precision approaching the natural linewidth of the D2-line, approximately 6 MHz.

The technique of saturated-absorption spectroscopy [120], also known as Lamb-dip spectroscopy, provides a simple approach for observing Doppler-free features in

an absorption spectrum. Figure 6.6 illustrates the essential elements of the technique as implemented in the MOT setup: a half-wave plate and a pair of polarizing beam-splitters are used to obtain two beams with a tunable intensity ratio counter-propagating through a vapour-cell. The transmission of the forward-propagating, low-power 'probe-beam' through the cell is detected with a silicon photodiode (Burr–Brown OPT101) in the presence of the backward-propagating, high-power 'pump-beam'. The transmitted probe-beam generally shows marked attenuation due to absorption in the vapour-cell when tuned within the Doppler profile of an atomic transition.

The velocity-class of atoms with an axial component of velocity such that they see the pump-beam frequency Doppler-shifted to the transition frequency experience partial saturation; that is a large fraction are in the excited state at any one time. Tuning the frequency of the beams within a natural linewidth of the transition allows the beams to interact with the same velocity-class of atoms increasing the transmission of the probe-beam as there are fewer ground-state atoms available to absorb.

The ground $2s\,^2S_{1/2}$ level in ^{7}Li gives rise to two hyperfine components with total angular momentum quantum number $F = (I \pm 1/2) \in \{1, 2\}$. The low value of $\langle\hat{\xi}_{\rm hfs}\rangle$ for the excited $2p\,^2P_{3/2}$ level leads to spacing of the hyperfine components of the order of the natural linewidth, effectively blurring them into a single broad level. A saturated absorption spectrum of the D2-line in a ^{7}Li vapour thus shows the expected Doppler-free transmission peaks for just two resolved hyperfine transitions. In addition to these, there is also a Doppler-free *dip* at the midpoint between these transitions commonly referred to as the 'cross-over dip'. To understand why, consider an atom illuminated by a laser beam with frequency ν, moving with paraxial velocity

component

$$v_{\mathrm{p}} = \pm c\frac{\Delta\nu_{\mathrm{hfs}}}{2\nu}, \tag{6.3}$$

where $\Delta\nu_{\mathrm{hfs}}$ is the ground state hyperfine splitting. Such an atom would experience a Doppler-shifted optical frequency

$$\nu' = \nu \pm \Delta\nu_{\mathrm{hfs}}/2. \tag{6.4}$$

When the laser frequency is tuned within a natural linewidth of the midpoint between the two transitions this velocity-class of atoms can interact with both beams. Because the counter-propagating beams are seen shifted onto transitions with different ground-states, depletion of one of the ground hyperfine-states due to saturation by the pump-beam has the effect of increasing the population of the other ground-state and hence produces a dip due to increased probe-beam absorption. Because this effect occurs for only a particular velocity-class of atoms, again the spectral feature is free of Doppler-broadening. Figure 6.7 shows the form of the variation in detected probe-beam signal as the laser frequency is scanned over the region around the two transitions, showing the cross-over dip at the midpoint.

For an analogous system with two upper-states coupled to a common ground-state, the saturation effect at the midpoint between the two transitions would produce a 'cross-over peak' because the pump-beam is able to deplete the ground-state of the transition driven by the probe-beam.

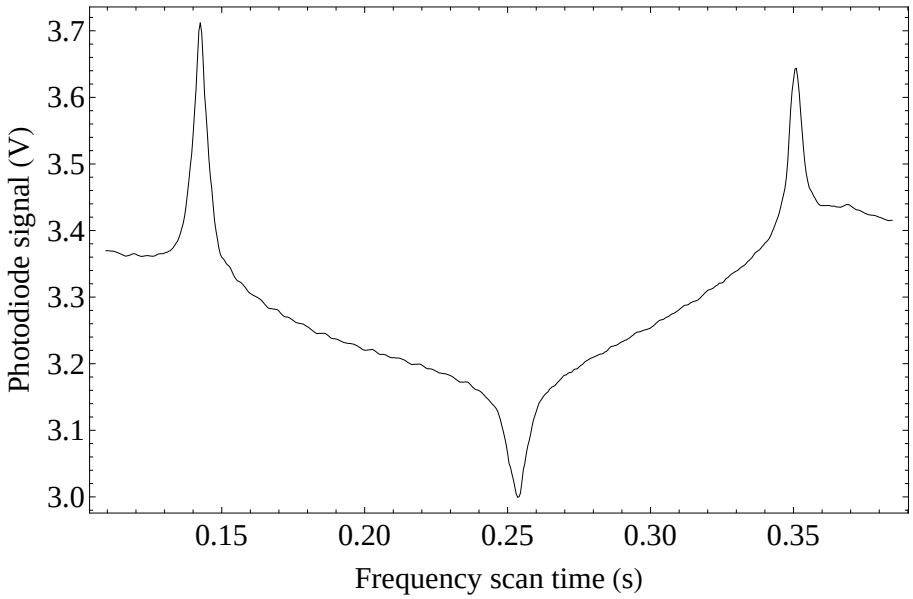

Figure 6.7: Saturated absorption spectrum of the ^{7}Li D2-line. The Doppler-free features include two peaks corresponding to a reduction in absorption from the $F = 1$ and $F = 2$ hyperfine components of the ground state, while the central dip occurs at the midpoint between the two transition frequencies. The offset of the dip from the centre is due to non-linear tuning of the laser frequency with time.

6.2.2 Peak-locking

Having obtained a narrow spectral feature at the midpoint between the two hyperfine transitions of the D2-line at ≈446810 GHz, a system must be implemented that overcomes the aforementioned limitations of direct optical-frequency measurement techniques to provide a usable error-signal for a high-bandwidth locking system. A lock-in amplifier circuit and amplified integrator controller previously constructed by Dr. Ben Sauer at Imperial College[1] are used in the locking system.

Using the peak-locking technique, the laser frequency is dithered around the centre of the crossover-dip at a modulation frequency, $f_{\mathrm{mod}} = 2.4$ kHz, obtained by applying a

[1]Cold Atoms Group, Blackett Laboratory, Imperial College London, UK.

sinusoidal voltage signal across the piezo-disk introduced in section 6.1.2. A peak-to-peak voltage amplitude of 6.7 V results in a laser-frequency modulation range of less than 50 MHz. The detected variation in probe-beam power traces out the spectral-lineshape of the dip which is dominated by the sum of the Lorentzian natural lineshape of the Doppler-free dip itself and the corresponding regions of the Doppler-profiles associated with the two transitions.

For a modulation centred on the dip, with an amplitude small compared with the width of the spectral feature, the harmonic-approximation can be taken, modelling the dip as a quadratic curve and leading to a simple approximate form for the transmitted probe-beam intensity as a function of laser-frequency,

$$I(\nu) = I_0 + \alpha(\nu - \nu_0)^2, \tag{6.5}$$

where $\nu_0 \approx 446810$ GHz is the laser frequency at the centre of the dip, I_0 is the transmitted probe-beam intensity at ν_0, and α is the curvature of the dip. For a sinusoidally varying frequency, $\nu(t) = \nu_L + A_{mod}\sin(2\pi f_{mod}t)$, the time-dependent frequency is given by

$$\begin{aligned} I(t) &= I_0 + \alpha A_{mod}^2 \sin^2(2\pi f_{mod}t) \\ &= I_0 + \frac{\alpha A_{mod}^2}{2}\left(1 - \cos(4\pi f_{mod}t)\right), \end{aligned} \tag{6.6}$$

which results in a detected signal at twice the modulation frequency. As the centre-frequency of the laser modulation, ν_L, moves off the centre of the dip, the curvature becomes progressively less harmonic and the amplitude of the $2f_{mod}$ component of

the detected signal drops while the amplitude of the f_{mod} component increases concomitantly. Any anharmonicity in the frequency-dependent probe-beam transmission curve also produces higher harmonic components, however these tend to be at low signal-levels and are hence neglected in this analysis.

The detected photodiode signal is AC-coupled and amplified, with gain K_{PD}, before being sent to a demodulator (Analog Devices AD630) using the original modulation signal, with a user-controlled phase-shift to account for any time-lag in the loop. The output of the demodulator is given by,

$$V_{\mathrm{demod}}(t) = \int_0^t H\left[\sin(2\pi f_{\mathrm{mod}} t' + \theta)\right] V_{\mathrm{PD}}(t')\mathrm{d}t', \tag{6.7}$$

where $H(x)$ is the Heaviside step-function and $t = 0$ denotes the moment the circuit is powered and the integrating capacitor begins charging. That is, $V_{\mathrm{demod}}(t)$ is given by the time-integral of the AC-coupled photodiode signal only while the modulation signal is positive, with the tunable phase, θ, included to ensure that the zero crossings of the modulation and photodiode signals are in phase. On the positive slope of the cross-over dip the signal being integrated is always positive, on the negative slope it is always negative, and when centred it undergoes a full 2π cycle while the modulation signal is positive and hence integrates to zero.

Finally a simple single-stage low-pass RC filter extracts the DC-component that is used as the error-signal for locking to the dip. A switch allows the inputs to the phase shifter to be exchanged, inverting the error signal if the system is to be used for locking to a peak instead of a dip.

6.2.3 Amplified integrator controller

Using the terminology of control theory [121]: the *error-signal*, E, determines the position of the *process variable*, PV (the absolute laser frequency), relative to the *set-point*, SP (the midpoint of the two resolved hyperfine transitions of the ^{7}Li D2-line). A controller is then required to use the time-varying error-signal to determine the *controller output*, CO, that will drive PV towards SP with the goal of maintaining an error signal as close to zero as possible.

One of the simplest commonly used controllers consists of an analog integrator with variable gain that gives a continuous cumulative integral of the error signal so that the controller 'remembers' time spent off to one side of the dip. This memory is essential for a peak-locking system because an excursion of PV right off the dip gives an instantaneous error-signal of zero. However, the accumulated CO from the excursion ensures that the PV is pushed in the correct direction to return to the SP. The controller output is therefore given by,

$$\mathrm{CO} = \frac{K_\mathrm{P}}{\tau} \int_0^t \mathrm{E}(t')\mathrm{d}t', \tag{6.8}$$

where K_P is the variable gain provided by an amplifier before the integrator, and $\tau = RC$ is the integrator time-constant. Using a pre-integrator gain rather than simply varying the integrator time-constant ensures linear gain-tuning.

The controller output is connected to the stack and current of the laser under control, completing the feedback-loop.

6.2.4 Peak-locking optimization

There are three settings that can be used to optimize the peak-locking system: photodiode gain, K_{PD}, pre-integrator gain, K_{P}, and the phase-shift, θ. A standard approach to the optimization of control systems is to perturb the variable under control and observe the response of the system. A general problem with this approach is that of defining a quantitative measure of system performance; in particular, reproducibly returning the system to the same locked state if the lock is lost due to the perturbation.

The technique for obtaining an error signal in a peak-locking system suggested a particular definition for the 'edge' of the locking region, without actually losing the lock. Monitoring a real-time fast-Fourier transform (FFT) of the photodiode signal permits a comparison of the power in the frequency components that vary as the laser frequency moves on and off the dip-centre. For a perturbing signal with amplitude, A_{p}, at frequency, f_{p}, the perturbed frequency is $\nu(t) = \nu_{\mathrm{L}} + A_{\mathrm{p}} \sin(2\pi f_{\mathrm{p}})$, giving an overall modulated, perturbed laser frequency,

$$\nu(t) = \nu_{\mathrm{L}} + A_{\mathrm{mod}} \sin(2\pi f_{\mathrm{mod}} t + \theta) + A_{\mathrm{p}} \sin(2\pi f_{\mathrm{p}}). \tag{6.9}$$

Substituting this into equation 6.5 gives a detected photodiode intensity,

$$\begin{aligned} I(\nu) &= I_0 + \alpha\left[A_{\mathrm{mod}}\sin(2\pi f_{\mathrm{mod}}t+\theta) + A_{\mathrm{p}}\sin(2\pi f_{\mathrm{p}})\right]^2, \\ &= I_0 + \alpha\big[A_{\mathrm{mod}}^2\sin^2(2\pi f_{\mathrm{mod}}t+\theta) + A_{\mathrm{p}}^2\sin^2(2\pi f_{\mathrm{p}}t+\theta) \\ &\quad + 2A_{\mathrm{mod}}A_{\mathrm{p}}\sin(2\pi f_{\mathrm{mod}}t+\theta)\sin(2\pi f_{\mathrm{p}})\big], \\ &= I_0 + \alpha\Bigg\{\frac{A_{\mathrm{mod}}^2}{2}\left[1-\cos(4\pi f_{\mathrm{mod}}t+\theta)\right] + \frac{A_{\mathrm{p}}^2}{2}\left[1-\cos(4\pi f_{\mathrm{p}}t+\theta)\right] \\ &\quad + A_{\mathrm{mod}}A_{\mathrm{p}}\Big[\cos(2\pi\{f_{\mathrm{mod}}-f_{\mathrm{p}}\}t+\theta) - \cos(2\pi\{f_{\mathrm{mod}}+f_{\mathrm{p}}\}t+\theta)\Big]\Bigg\}. \end{aligned} \tag{6.10}$$

The detected signal thus has frequency components at $2f_{\mathrm{mod}}$, $2f_{\mathrm{p}}$ and $f_{\mathrm{mod}} \pm f_{\mathrm{p}}$. If, however, the locking system is satisfactorily correcting for the perturbation, the power in the $f_{\mathrm{mod}} \pm f_{\mathrm{p}}$ components will be small and the signal will look more like that of equation 6.6. Based on these expectations, a somewhat arbitrary but very precise and reproducible definition for the 'edge' of the lock is the point at which the power in each of the $f_{\mathrm{mod}} \pm f_{\mathrm{p}}$ components is equal to that in the $2f_{\mathrm{mod}}$ component.

Figure 6.8(a) shows an FFT trace of the photodiode signal with a perturbing signal of sufficient frequency and amplitude to place the system at the edge of the locking region. The optimization scheme consists of gradually increasing the perturbation amplitude, and for each value of A_{p}, increasing the value of f_{p} until the edge of the lock is reached, such that any increase in A_{p} or f_{p} will result in more power in the $f_{\mathrm{mod}} \pm f_{\mathrm{p}}$ signal than in the $2f_{\mathrm{mod}}$ signal. In perturbation parameter space the system is now at $\{A_{\mathrm{p,max}}, f_{\mathrm{p,max}}\}$. Plotting $A_{\mathrm{p,max}}$ against $f_{\mathrm{p,max}}$ results in a curve like that shown in figure 6.8(b), where the sinusoidal perturbing voltage amplitude is used as a proxy for A_{p}. The results show a clear inverse relationship, with a small but

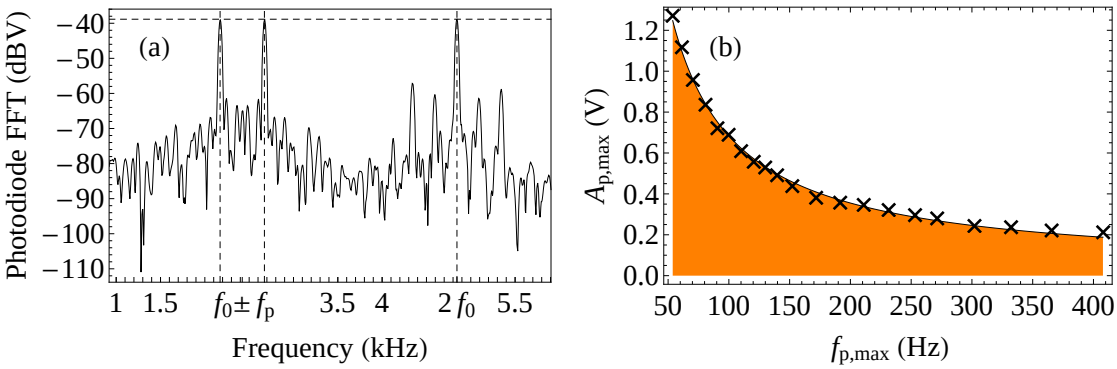

Figure 6.8: Details of the peak-locking optimization scheme. (a) An FFT of the photodiode signal with a perturbation that places the system at the locking 'edge' of the locking region, with equal power in the $f_{\mathrm{mod}} \pm f_{\mathrm{p}}$ and $2f_{\mathrm{mod}}$ signals. (b) The maximum perturbing amplitude for different perturbing frequencies (and vice versa), showing a functional form as in equation 6.11 with $C = 65.7(8)$ V/Hz and $D = 0.027(7)$ V. The shaded region indicates stable locking.

statistically significant offset,

$$A_{\mathrm{p,max}} = \frac{C}{f_{\mathrm{p,max}}} + D. \tag{6.11}$$

The optimal locking system parameters are taken to be those that maximize C. The gain values used for the data shown in figure 6.8 were $K_{\mathrm{PD}} = 10$ and $K_{\mathrm{P}} = 0.56$, resulting in a value, $C = 65.7(8)$ V/Hz and $D = 0.027(7)$ V, while the optimal settings were $K_{\mathrm{PD}} = 100$ and $K_{\mathrm{P}} = 0.1$, resulting in a value, $C = 106(3)$ V/Hz.

With the gain settings optimized through this systematic approach, the locking system successfully locked an ECDL to the crossover dip in the saturated absorption spectrum of the ^{7}Li D2-line for several hours, including testing by momentarily blocking the beam.

6.3 Laser frequency offset locking

Having obtained a stable, low-power frequency reference source locked to the mid-point between the two resolved hyperfine transitions in the ^{7}Li D2-line, the experiment calls for a mechanism to lock two high-power sources with independently tunable frequency-offsets from this reference to provide the cooling and repumping beams that address these two transitions. Independently selectable detunings from the beams' respective transitions are essential for optimization of the MOT population and lifetime.

6.3.1 Offset-locking theory

The offset frequency between the two beams with electric field amplitudes F_1, F_2, with angular frequencies ω_1, ω_2, and polarization vectors $\hat{\boldsymbol{\varepsilon}}_1$, $\hat{\boldsymbol{\varepsilon}}_2$ can be observed through the beat signal obtained by aligning the two beams coaxially on a photodiode with a sufficiently fast response. An ideal, infinite-bandwidth photodiode with the standard quadratic-response would detect a time-varying signal, $S^{(\infty)}(t)$, given by

$$\begin{aligned} S^{(\infty)}(t) =& A[\hat{\boldsymbol{\varepsilon}}_1 F_1 \sin(\omega_1 t) + \hat{\boldsymbol{\varepsilon}}_2 F_2 \sin(\omega_2 t)]^2 \\ =& A\Big(F_1^2 \sin^2(\omega_1 t + \phi_1) + F_2^2 \sin^2(\omega_2 t + \phi_2) \\ &+ \hat{\boldsymbol{\varepsilon}}_1 \cdot \hat{\boldsymbol{\varepsilon}}_2 F_1 F_2 \big(\cos[(\omega_1 + \omega_2)t] - \cos[(\omega_1 - \omega_2)t] \big) \Big), \end{aligned} \tag{6.12}$$

where the constant, A, takes account of the geometrical overlap of the beams and the detector active region, in addition to detector sensitivity, filtering and amplification. At optical frequencies, ω_1, ω_2 and $(\omega_1 + \omega_2)$ are well beyond the upper frequency limit of any real, bandwidth-limited detector, so the actual detected signal, $S(t)$ is given

by

$$S(t) = \hat{\varepsilon}_1 \cdot \hat{\varepsilon}_2 A F_1 F_2 \cos[(\omega_1 - \omega_2)t]. \tag{6.13}$$

An important point included explicitly in these expressions is the requirement for some common component of the two polarization vectors; orthogonally polarized beams produce no beat signal.

The difference frequency that serves as the process variable in the offset-locking system, lying in the range 350–450 MHz, is many orders of magnitude lower than the absolute frequencies of the lasers and does fall within the the region accessible to detectors. Nonetheless, producing a DC error-signal based on direct frequency measurement is still well beyond the capabilities of available transducers so alternative means must be found.

The two standard approaches to detecting frequencies in this range use either the frequency dependent phase-lag following passage through a delay-line [122] or frequency dependent power variation on passage through a filter [123] as proxies for the offset-frequency. Although a circuit for delay-line locking was already available, having been inherited from another group, discussions with Samuel Pollock at Imperial College[2] led to the decision to adopt this latter technique based on its excellent stability and broad locking range.

6.3.2 Side-of-filter locking

Using this method the error signal is obtained by splitting the beat signal in two and comparing the power in a reference arm, including a 6 dB fixed attenuation, with a 'filter' arm including a fixed 3 dB attenuation and a high-pass filter. When the

[2]Cold Atoms Group, Blackett Laboratory, Imperial College London, UK.

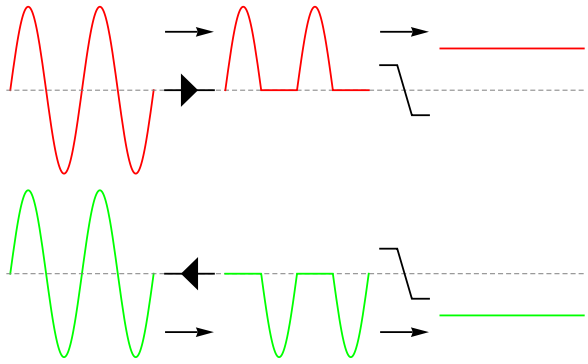

Figure 6.9: Illustrating the use of diodes for RF power comparison. The reference and filter arms are half-wave rectified in the opposite sense, low-pass filtered, and the resulting DC signals averaged to produce the error signal.

frequency of the beat signal is equal to the -3 dB point of the filter the power in the two arms is identical. A tunable offset frequency is obtained through the addition of a voltage-controlled oscillator (VCO) and frequency mixer, giving the difference frequency between the incident beat signal and the VCO signal. The power in the two arms is then equal when the incident beat signal frequency is equal to the sum of the VCO frequency and the -3 dB point of the filter.

Figure 6.9 shows how a pair of diodes with opposite orientations can be used to compare the power in the two arms by half-wave rectifying each in the opposite sense, low-pass filtering to extract the DC components, then taking the average of the two.

With the reference laser locked to the crossover dip at the midpoint between the two resolved hyperfine components of the D2-line, the cooling and repumping lasers must be locked at independently variable red-detunings from the two transitions. The two offset frequencies are given by

$$\nu_{\text{offset}} = \frac{\Delta\nu_{\text{hfs}}}{2} \pm \Delta_{\text{max}}, \tag{6.14}$$

where $\Delta\nu_{\mathrm{hfs}}$ is the ^{7}Li ground-state hyperfine splitting of 803.5 MHz and Δ_{max} is the maximum required detuning. Based on information available in the literature a maximum of 8 natural linewidths is judged to be more than sufficient, where the excited-state lifetime of 27 ns gives a linewidth, $\Gamma/(2\pi) = 1/(2\pi \times 27\ \mathrm{ns}) \approx 5.9$ MHz, giving $\Delta_{\mathrm{max}} \approx 47$ MHz [9].

The RF components are chosen from the widely used Mini-Circuits product-line[3]. It is essential to carefully assess the range of operating frequencies and power levels before choosing particular RF components. The required offset-locking range is 350–450 MHz; the PHP-175+ high-pass filter is used as the frequency → amplitude converter in the filter arm, with a -3 dB attenuation point at 140 MHz giving a required VCO operating range of at least 210–310 MHz. The POS-400+ VCO, with a nominal frequency range of 200–380 MHz, can satisfy the requirements for either the cooling or repumping beams, meaning that two identical systems can be constructed and can be used interchangeably with the two beams despite both being red-detuned from their respective transitions.

In addition to frequency considerations, the RF power at various points in the circuit must be considered. The PDC-20-1W directional coupler is used obtain a low power monitor signal at the incident beat frequency with minimal loss of power from the mainline signal, while the beat-note between the incident beat signal and the internal VCO is obtained using an SRA-2+ mixer with a low conversion loss of around 5.6 dB.

Amplification proved to be more problematic: amplifiers with a through-hole package ('plug-in' to use Mini-Circuits terminology) such as the MAN-1AD and MAN-1LN

[3] http://www.minicircuits.com/

ended up having either the gain or maximum power output too low to drive the error-signal circuit, while high-power stand-alone amplifiers ('connector') are expensive and prevent the entire circuit being constructed on a single printed circuit board (PCB). Surprisingly, it transpires that small surface-mount amplifiers can give the required gain and power output; their excellent thermal coupling to the PCB compensating for a small heat-capacity. The PSA-545+ amplifier, with a gain of 23.5 dB and maximum output power of +20 dBm (100 mW), provides plenty of power, although the SOT-363 surface-mount package with 0.65 mm lead-spacing is challenging to solder and the device is *extremely* sensitive to electrostatic discharge.

Figure 6.10 shows a schematic of the error-signal circuit used to generate the error-signal from the incident beat signal and the controller circuit using to obtain feedback signal from the error-signal. In the error-signal circuit, note the liberal use of decoupling capacitors to reduce noise in the DC control circuitry, the on-board ZSR300 3V regulator, and the powering of the amplifier both through the PWR and OUT pins. The reference (upper) and filter (lower) arms are clearly distinguishable after the power-splitter, with Schottky diodes used to minimize power losses, and a two-stage RC low-pass filter to extract the DC component.

The controller circuit is an implementation of a proportional–integral (PI) control system, somewhat more flexible than the amplified integrator used for absolute frequency locking and discussed in section 6.2.3. The CO for this system is given by,

$$\mathrm{CO} = K_\mathrm{P}\mathrm{E}(t) + K_\mathrm{I}\int_0^t \mathrm{E}(t')\mathrm{d}t', \tag{6.15}$$

where K_P is now the 'proportional gain', and K_I is the 'integrator gain' given by the inverse of the integrator time-constant. An optional inverter is provided on the output

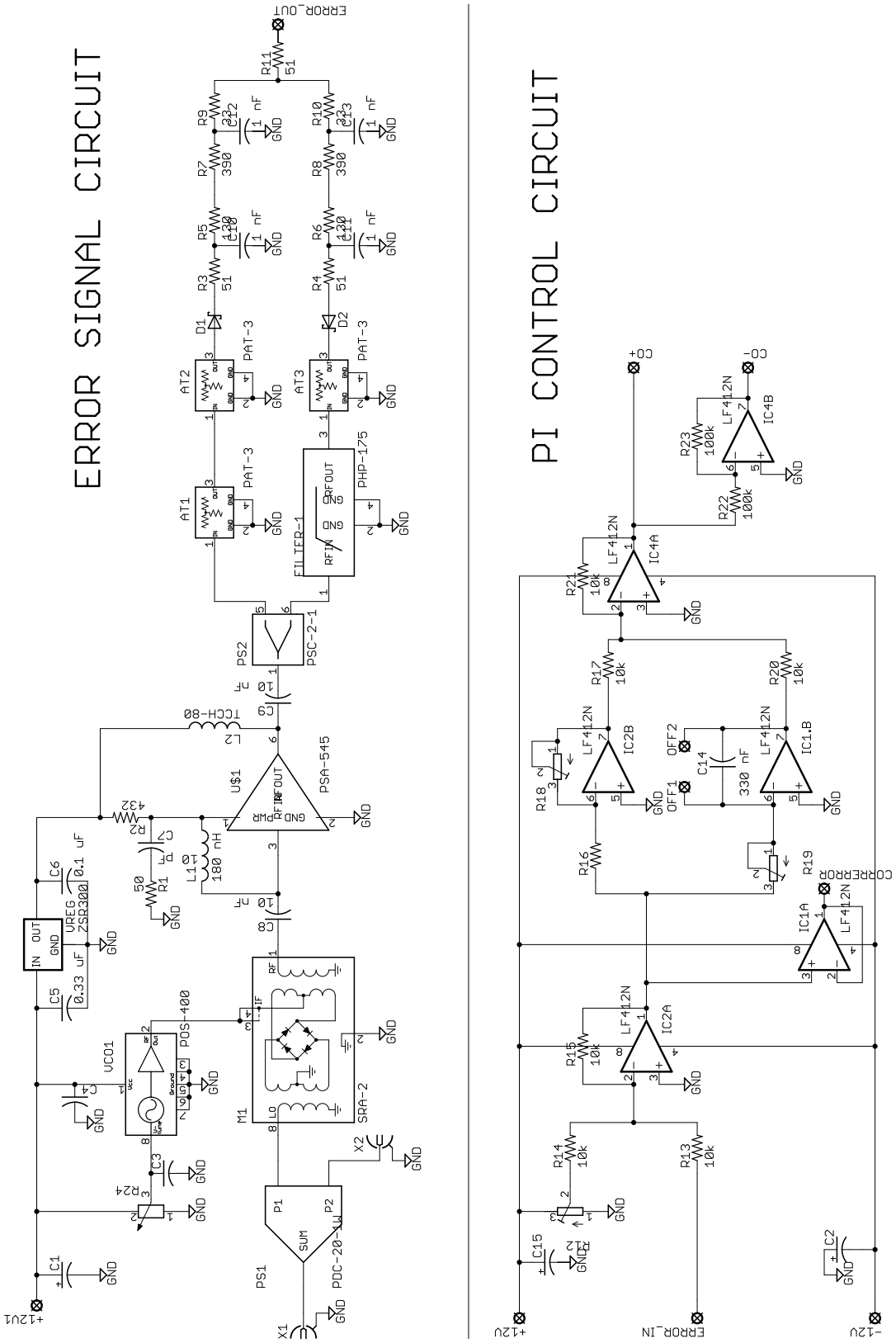

Figure 6.10: Schematics of the offset-locking error-signal and controller circuits.

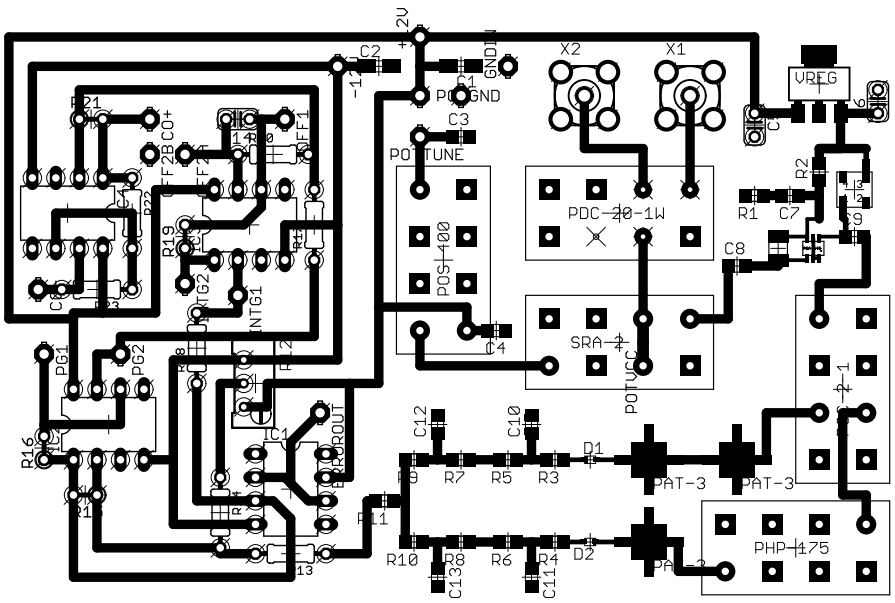

Figure 6.11: Complete offset-locking circuit board layout with the ground-plane omitted for clarity.

giving the option to select ±CO. This feature allows the user to add the information that is lost in using a beat-frequency input, defining whether the laser under lock is higher or lower in frequency than the reference laser. A final feature worthy of note is a tunable voltage added to the ERROR_IN value shown in figure 6.10; this feature corrects for asymmetry in the transmission function of the high-pass filter used in the error-signal circuit and is discussed further below.

The two circuits shown in figure 6.10 are implemented on a single PCB, the layout of which is shown in figure 6.11. Note the on-board SMA coaxial connectors, X1 and X2, for good impedance matching at the junctions with the RF input and monitoring output. A complete ground-plane is included on the board (omitted from the figure) to reduce spurious pick-up, particularly between the RF error-signal circuit and the controller.

The error-signal circuit was tested by providing a fixed input of +6 dBm signal at

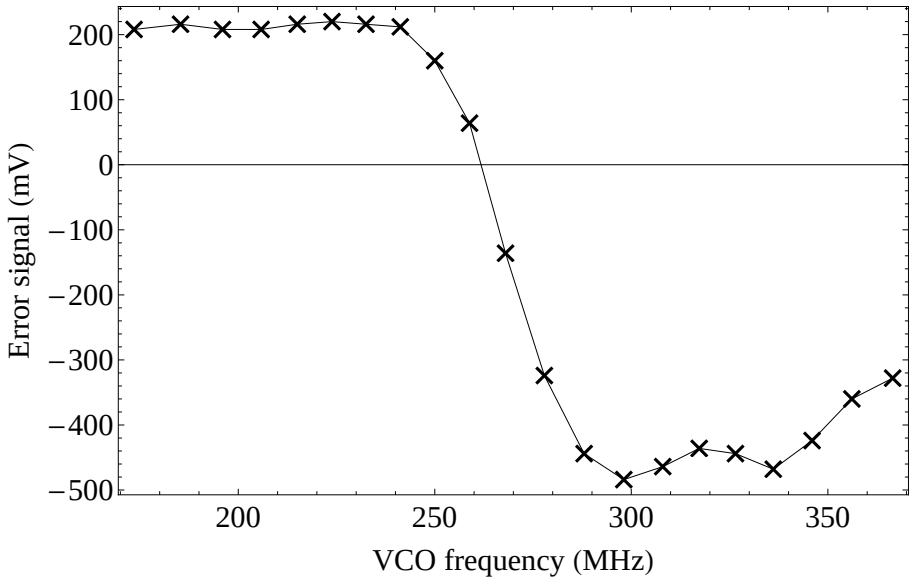

Figure 6.12: Variation in offset-locking error signal with internal VCO frequency for a fixed +6 dBm input at 400 MHz. Note asymmetric limits about the zero-crossing.

400 MHz from an external POS-535+ VCO, tuning the internal VCO frequency, and recording the resultant variation in the error-signal. The results of this test are shown in figure 6.12; note the frequency range of 200 MHz, limited only by the tuning range of the internal VCO, and the asymmetry of the error signal limits about the zero-crossing. The total capture range is limited by parasitic inductance in the circuit, which reduces the transmission of the error-signal circuit at high frequencies.

The frequency offset indicated by the incident beat-frequency is monitored on a spectrum analyzer via the directional coupler (the PDC-20-1W in figure 6.10). Despite the monitor output being taken before the beat-signal is sent to the frequency mixer, the high sensitivity of the spectrum analyzer allows it to pick up small signals representing the other frequencies present in the circuit well above the noise floor. Figure 6.13 shows a typical trace, with the high-power incident beat-signal locked

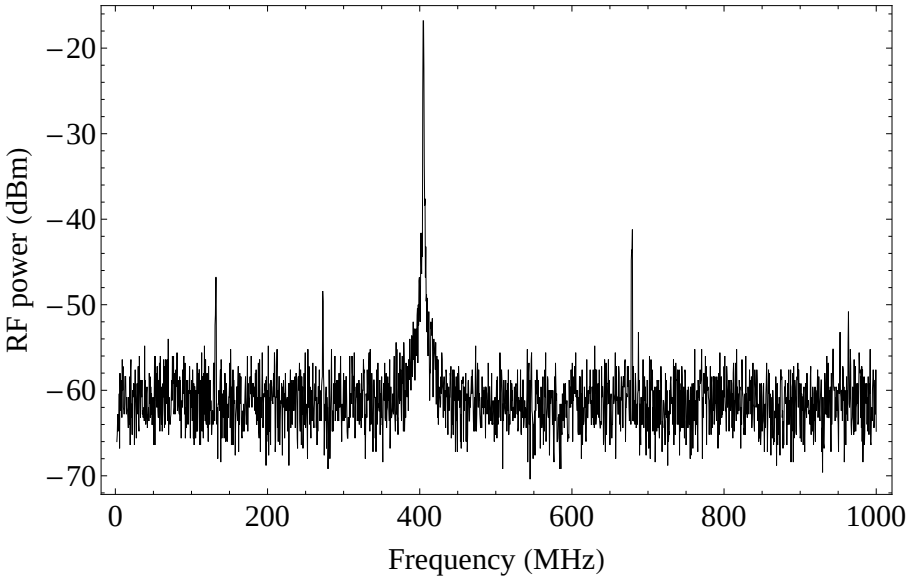

Figure 6.13: Frequencies present during offset-locking, detected through the directional coupler used to monitor the incident beat-signal.

at 400 MHz, the internal VCO at 260 MHz, and the sum and difference frequencies generated by the mixer at 140 MHz (equal to the -3 dB point of the high-pass filter) and 660 MHz respectively. The ability to monitor all frequency components simultaneously is extremely useful for troubleshooting.

Side-of-filter error correction

A curious feature of the side-of-filter error-signal scheme, that appeared without comment in the original publication [123], is the asymmetry of the error signal about the zero-crossing. This effect is clearly visible in figure 6.12. A primary cause of this asymmetry is the asymmetry present in all RF filters: the transmission in the stop-band is essentially zero, while there is a significant amount of attenuation in the pass-band. The transmission of a filter at the -3 dB point is approximately 1/2 ($10^{-3/10} \approx 0.5012$), which is not the midpoint of the transmission limits.

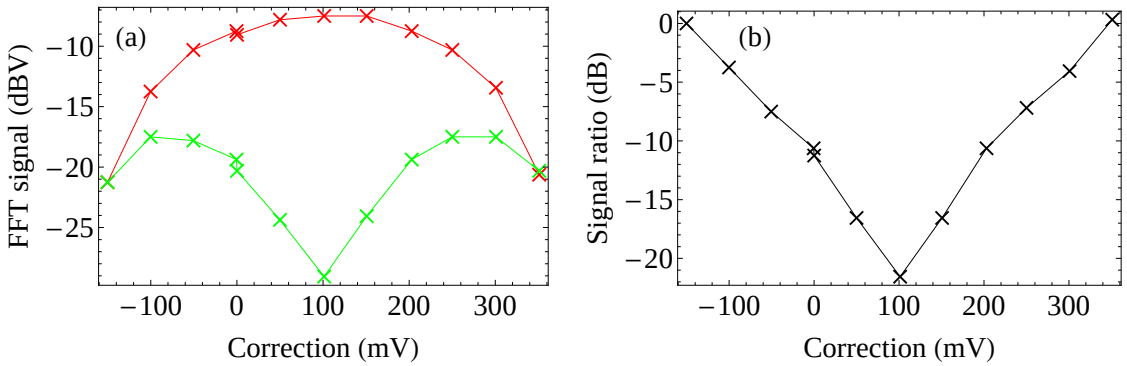

Figure 6.14: Correcting for asymmetry in the offset-locking error-signal. Locked laser output frequency modulated at f_{mod} = 1 kHz: (a) the amplitudes of the f_{mod} (red, upper) and $2f_{\mathrm{mod}}$ (green, lower) components of the error signal; (b) the ratio of the $2f_{\mathrm{mod}}$ and f_{mod} component amplitudes. The symmetry point is clearly evident at a correction of around 100 mV.

The effect of adding a tunable offset voltage to the error-signal to correct for this asymmetry was investigated by modulating the frequency of the locked laser through application of a 1.5 V amplitude, f_{mod} = 1 kHz signal to the disk, taking an FFT of the resulting error signal and recording the power in the f_{mod} and $2f_{\mathrm{mod}}$ components after passing through a modified differentiator employed as a high-pass filter. The dependence of these powers on the offset voltage is shown in figure 6.14(a) labelled 'correction', with the corresponding variation in the ratio of the two powers shown in figure 6.14(b). The point of symmetry is clearly evident at an offset voltage of around 100 mV.

6.4 Optical amplification

The use of a reference ECDL locked to a lithium saturated absorption spectrum and two other ECDLs locked a tunable offset from the reference provides the requisite optical frequencies needed for the MOT cooling and repumping beams, however the

power in each beam is quite low (≈5–7 mW). Injection-locking is a widely applicable amplification technique in which the output of a low-power oscillator with desirable frequency characteristics is injected into a second oscillator with a large gain [124].

In optical systems this means using the beam from a low-power, 'primary' laser with the desired absolute frequency, tunability and linewidth to seed a higher-power, 'secondary' laser to produce a high-power beam with those same frequency characteristics [125]. A particular type of semiconductor device known as a *tapered amplifier* is designed specifically for use as such a secondary laser amplifier, providing high output power with a relatively clean spatial profile [126]. Previous studies have demonstrated the ability of such systems to amplify multiple closely-spaced frequency components in the wavelength region around 671 nm [127].

The tapered amplifier used is a Sacher Lasertechnik TEC-400-0670-500. Under normal operating conditions a low-power beam is emitted in the reverse direction that can be used for alignment purposes. Using a previously developed beam-profiler based on a CMOS image-sensor [128, 129], the Gaussian beam-parameters of this alignment beam were ascertained to permit maximal coupling of the primary laser into the tapered amplifier diode.

As with all diode laser systems (and indeed, any light emitting diode), gain is larger for light polarized in the plane of the PN-junction [130]. For a homogeneously broadened laser such as a diode laser, the mode with the largest excess of gain over losses (per unit length) will come to dominate, and hence the output is highly polarized. For an inhomogeneously broadened laser, a given mode will dominate only within a limited wavelength region, but the result is still a highly polarized output

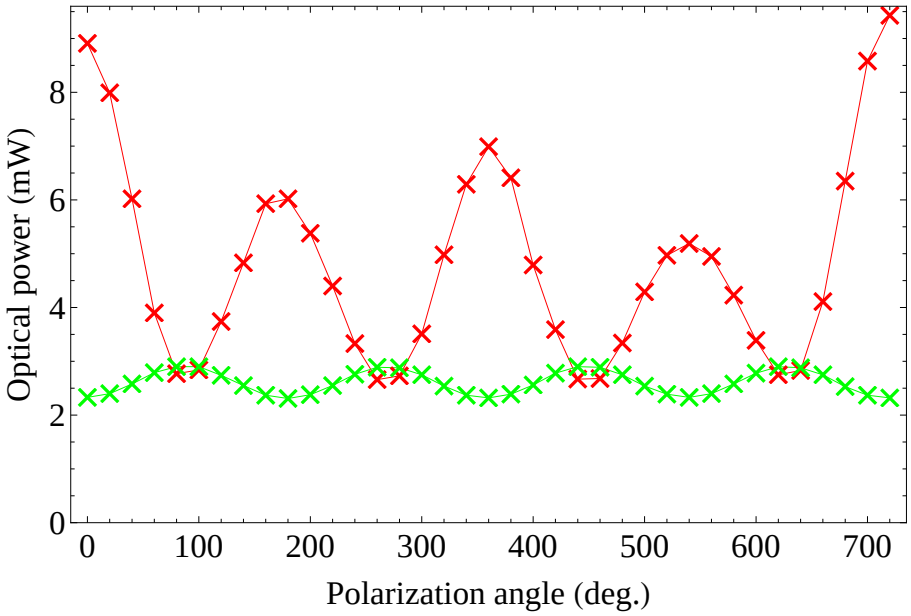

Figure 6.15: Variation in tapered amplifier output power (red – upper) and input power (green – lower) with input polarization, with 0° corresponding to vertical polarization.

beam. Coupling optimally into the tapered amplifier therefore requires precise control, not only of the beam-width, position of the focus and Rayleigh-range, but also the polarization.

The upper curve in figure 6.15 shows the variation in tapered amplifier output power as the input polarization is rotated for an approximately constant input power of 2.7 mW. The polarization was rotated using a half-wave retarder, which effects an optical rotation of twice the physical rotation, such that the 360° rotation at the midpoint of the curve is only a 180° rotation of the optic. It is likely that a small misalignment of the optic within its rotational mount led to the drop in power at the midpoint, while polarization dependent Fresnel reflection from an additional optic downstream of the retarder caused the variation in tapered amplifier input power.

The tapered amplifier diode itself is anti-reflection coated front and back to avoid

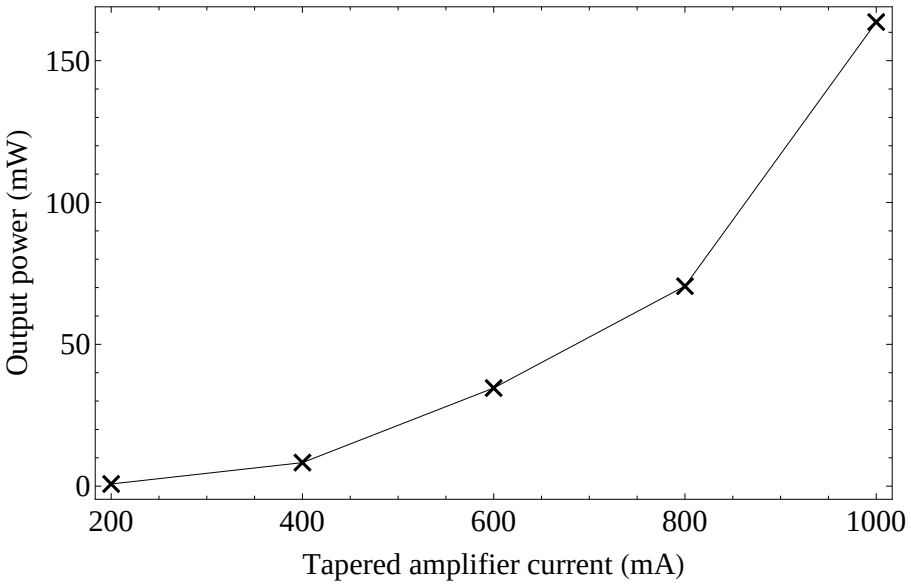

Figure 6.16: Variation in tapered amplifier output power with injection current for an input power of approximately 3.3 mW single-mode, vertically polarized with a wavelength of approximately 671 nm.

laser action independent of the injected seed light [131]. Because there is no optical cavity, all amplification must occur on a single pass, so the gain per unit length must be extremely large, achieved using a very high injection current that necessitates an efficient thermal control system. As a test of the capabilities of the amplifier, a ≈3.3 mW, vertically polarized, single-mode beam from an ECDL was injected and the output power recorded as the tapered amplifier current was varied, resulting in the curve shown in figure 6.16.

6.5 The complete optical system

The complete optical layout of the MOT is shown in figure 6.17. Three ECDLs are used, each protected from back-reflections by an optical isolator, with ECDL1

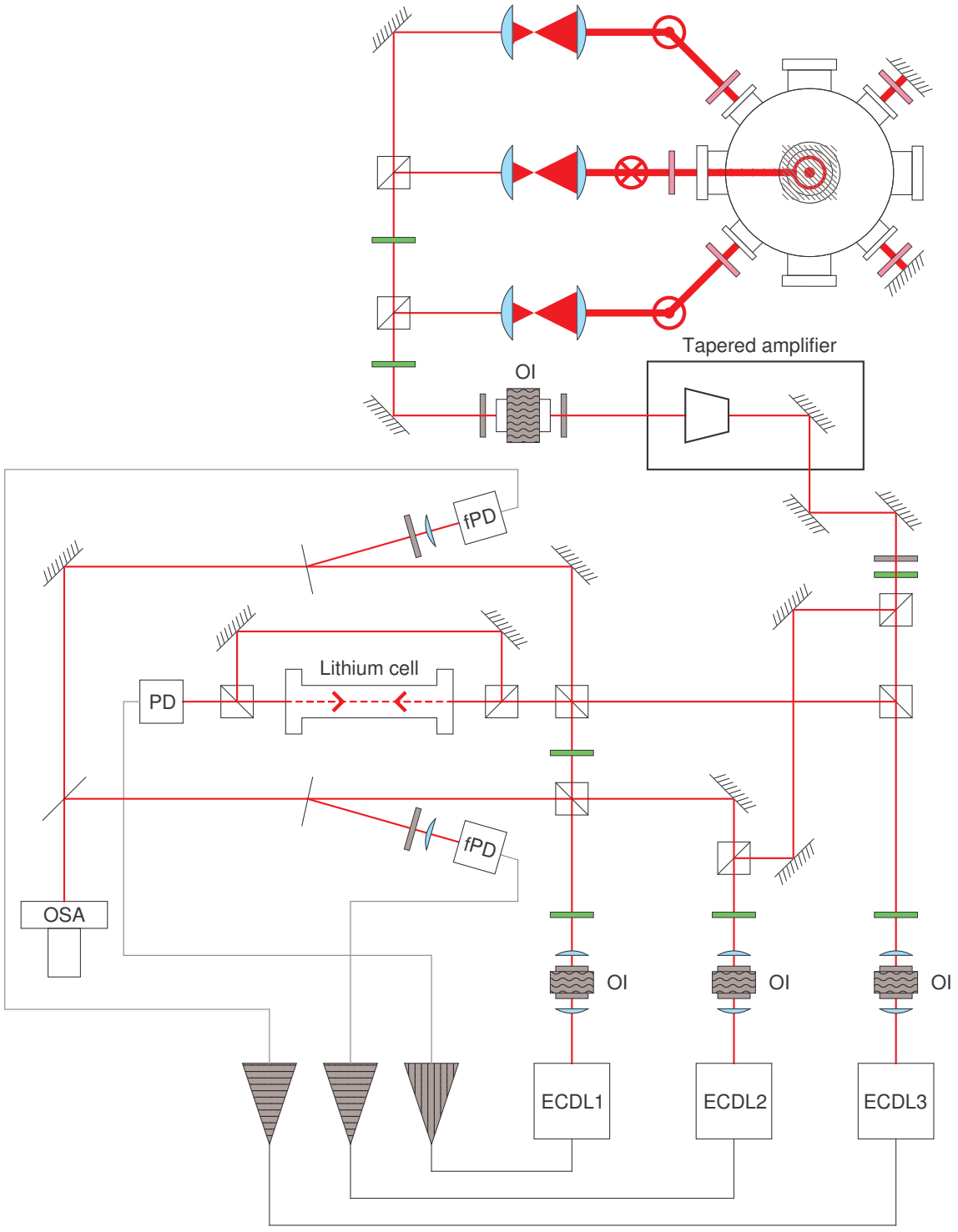

Figure 6.17: Schematic layout of the MOT optics. OI = optical isolator, OSA = optical spectrum analyzer, PD = photodiode, fPD = fast-photodiode, half-wave plates in green, quarter-wave plates in magenta, linear polarizers in grey. The cube beam-splitters reflect vertically (s) polarized and transmit horizontally (p) polarized light.

locked to the crossover dip in the ^{7}Li saturated absorption spectrum using the peak-locking technique discussed in section 6.2.2. The beams from ECDL2 and ECDL3 are overlapped with that of ECDL1 and the beat-signals obtained using a linear polarizer and a fast photodiode for offset-locking using the side-of-filter technique discussed in section 6.3.2. The power ratio at each branching-point is controlled using a half-wave plate to vary the linear polarization angle incident on a polarizing beam-splitter.

The remainder of the ECDL2 and ECDL3 beams are overlapped, rotated to ±45° polarizations, and projected onto a common, vertical axis for injection into the tapered amplifier discussed in section 6.4. The amplified two-component beam passes through a further optical isolator, then is split into three equal power beams that are expanded by a factor of four and converted to right-circular polarization using quarter-wave plates. These three beams, intersecting along three orthogonal axes and retro-reflected with an additional quarter-wave plate to maintain right-circular polarization with respect to the direction of propagation, perform the laser-cooling and repumping functions in the MOT.

At the time of writing of this thesis the optical systems for the MOT are completed and well characterized. Preparations have been made for testing the lithium dispensers to be used for loading the MOT, with a custom mount constructed and ready, and a microcontroller-based current control system designed. Some machining remains to be completed in order to mount a dispenser in the MOT vacuum chamber. It is the authors hope that the integration of the optical, magnetic and mechanical systems will be complete in the near future.

Chapter 7

Polarization Measurement and Control

Consisting of propagating orthogonal transverse waves of electric- and magnetic-fields, an important property of light is its *polarization*, describing the relative amplitudes and phases of two orthogonal components of the electric field in any Cartesian coordinate system as a function of position and time. It is important because it determines such parameters as refraction and diffraction characteristics, and interface reflectivities, and also crucially because it breaks the cylindrical symmetry implicit in theoretical descriptions such as the plane wave or TEM_{00} Gaussian beam.

These effects all stem from the fact that electromagnetic fields carry angular momentum, with an orientation associated with the polarization vector. These angular momentum considerations lead to the electric-dipole selection rules discussed in section 5.2.1 and hence provide a precise tool for the control of atom–light interactions that is essential for the construction of a MOT. Further, as has been described in chapter 6, efficient operation of the tapered amplifier system requires precise control

of the input polarization.

7.1 Introduction to polarimetry

As with any variable that is to be controlled, one of the key requirements is an accurate technique for measurement. Polarization, being described by a vector quantity, cannot be simply determined by a single measurement from a transducer, and in fact turns out to require a minimum of four intensity values for an unambiguous measurement.

The techniques of polarimetry have a wide range of applications. Stokes vector polarimetry is a powerful tool able to capture all of the polarization properties of a given light source [132]. Combined with spectral analysis it forms the basis for Stokes vector spectroscopy which is employed in diverse applications ranging from industrial sample analysis to solar astronomy [133, 134]. Mueller matrix polarimetry uses a source with well-known polarization and applies the techniques of Stokes vector polarimetry to obtain information on the polarization-changing properties of optical elements [135]. When applied to the modes of an optical fiber this provides a direct measurement of polarization-mode dispersion, which places a limit on data transmission rates [136]. Ellipsometry is a related technique that analyzes the polarization state of reflected light to measure the dielectric properties of thin films [137]. Imaging polarimetry, in which a Stokes vector is obtained for each pixel in an image, has become a powerful and widely used tool in remote sensing [138].

7.1.1 The Stokes vector

The polarization character of electromagnetic waves, whether fully-, partially- or un-polarized, can be completely and rigourously described using the Stokes vector. Introduced by Sir George Stokes in 1852 [139], the Stokes vector, $\mathbf{S}$, consists of four parameters, S_0–S_3, representing the total intensity, the excess of horizontal over vertical linearly polarized light, the excess of +45° over −45° linearly polarized light, and the excess of right- over left-circularly polarized light respectively,

$$\mathbf{S} = \begin{pmatrix} S_0 \\ S_1 \\ S_2 \\ S_3 \end{pmatrix} = \frac{1}{2} c\varepsilon_0 \begin{pmatrix} \langle|\tilde{E}_x|^2\rangle + \langle|\tilde{E}_y|^2\rangle \\ \langle|\tilde{E}_x|^2\rangle - \langle|\tilde{E}_y|^2\rangle \\ \mathrm{Re}\langle\tilde{E}_x\tilde{E}_y\rangle \\ \mathrm{Im}\langle\tilde{E}_x\tilde{E}_y\rangle \end{pmatrix}, \tag{7.1}$$

where the direction of propagation is taken to be $\hat{\mathbf{z}}$ and the angle brackets denote a time-average. Using these parameters, the degree of polarization, P can be defined as the ratio of the polarized component to the total intensity,

$$P = \frac{\sqrt{S_1^2 + S_2^2 + S_3^2}}{S_0}. \tag{7.2}$$

To facilitate comparison of different polarizations at different incident intensities, the Stokes parameters are often presented as dimensionless numbers, normalized such that $S_0 = 1$. This convention will be followed throughout the remainder of this chapter.

In order to use Stokes' mathematical formalism to assess how the optical elements comprising a polarimeter affect the incident polarization, a mathematical representation of the optical elements is needed. In 1949, Hans Mueller developed a method

that uses 4×4 matrices to represent the polarization-changing effect of any optical element or group of elements[1] [140]. The effect of rotating an element about the beam axis can be determined using a 4×4 rotation matrix, $\underline{\underline{\mathrm{R}}}$, applied in the conventional manner: $\underline{\underline{\mathrm{M}}}(\theta) = \underline{\underline{\mathrm{R}}}(\theta)^{-1}\underline{\underline{\mathrm{M}}}(0)\underline{\underline{\mathrm{R}}}(\theta)$. Using this approach, general forms can be obtained for a phase retarder with phase Δ, with its fast axis at an angle β to a fixed horizontal reference axis,

$$\underline{\underline{\mathrm{M}}}_{\mathrm{ret}}(\Delta,\beta) = \begin{pmatrix} 1 & 0 & 0 & 0 \\ 0 & \cos^2(2\beta) + \cos\Delta \sin^2(2\beta) & \sin(4\beta)\sin^2(\Delta/2) & -\sin(2\beta)\sin\Delta \\ 0 & \sin(4\beta)\sin^2(\Delta/2) & \cos^2(2\beta)\cos\Delta + \sin^2(2\beta) & \cos(2\beta)\sin\Delta \\ 0 & \sin(2\beta)\sin\Delta & -\cos(2\beta)\sin\Delta & \cos\Delta \end{pmatrix}, \quad (7.3)$$

and an ideal linear polarizer (with an infinite extinction ratio) at an angle γ to the same reference axis,

$$\underline{\underline{\mathrm{M}}}_{\mathrm{pol}}(\gamma) = \begin{pmatrix} \frac{1}{2} & \frac{1}{2}\cos(2\gamma) & \cos\gamma\sin\gamma & 0 \\ \frac{1}{2}\cos(2\gamma) & \frac{1}{2}\cos^2(2\gamma) & \frac{1}{4}\sin(4\gamma) & 0 \\ \cos\gamma\sin\gamma & \frac{1}{4}\sin(4\gamma) & 2\cos^2\gamma\sin^2\gamma & 0 \\ 0 & 0 & 0 & 0 \end{pmatrix}. \quad (7.4)$$

Known as Mueller calculus, this matrix approach can be used to determine the output polarization-state of a beam, $\mathbf{S}_{\mathrm{out}}$, after passing sequentially through N optical elements with Mueller matrices, $\left\{\underline{\underline{\mathrm{M}}}_i\right\}$ $(i = 1, 2, \ldots, N)$, given an incident polarization,

[1] See reference [141], pages 373–379.

$\mathbf{S}_{\text{in}}$,

$$\mathbf{S}_{\text{out}} = \underline{\underline{\mathrm{M}}}_N \cdots \underline{\underline{\mathrm{M}}}_2 \underline{\underline{\mathrm{M}}}_1 \mathbf{S}_{\text{in}}. \tag{7.5}$$

7.1.2 The rotating quarter-wave plate method

In general, techniques for the determination of polarization proceed by observing how a birefringent optical element or elements change the linear polarization component of a beam measured parallel with a fixed or rotating reference axis. Among the most widely used polarimetry techniques is a convenient method known as the rotating quarter-wave plate method. As the name implies, the birefringent element is a quarter-wave retarder at the wavelength of interest, with the fast-axis at a variable angle, β, to the reference axis, conventionally chosen to be horizontal. For broadband light, achromatic retarders are available that provide a consistent quarter-wave retardance over a range of up to several hundred nm [142]. Following the retarder is a linear polarizer with the transmission axis at a fixed angle, γ, to the reference axis, and a detector such as a photodiode to measure the total transmitted intensity over a range of values of β.

From equation 7.5 the Stokes vector following passage through the two optical elements, $\mathbf{S}'$, given an initial Stokes vector, $\mathbf{S}$, is given by,

$$\mathbf{S}' = \underline{\underline{\mathrm{M}}}_{\text{pol}} \underline{\underline{\mathrm{M}}}_{\text{ret}} \mathbf{S}. \tag{7.6}$$

Using the forms for the two Mueller matrices from equations 7.3 and 7.4 the expected

variation in detected intensity, S_0', can be determined,

$$\begin{aligned} I(\beta,\Delta,\gamma) = S_0' = \frac{1}{2}\{&S_0 + S_1[\cos(2\beta)\cos\big(2(\gamma-\beta)\big) - \sin(2\beta)\sin\big(2(\gamma-\beta)\big)\cos\Delta] \\ &+ S_2[\sin(2\beta)\cos\big(2(\gamma-\beta)\big) + \cos(2\beta)\sin\big(2(\gamma-\beta)\big)\cos\Delta] \\ &+ S_3[\sin\big(2(\gamma-\beta)\big)\sin\Delta]\}. \end{aligned} \tag{7.7}$$

There are numerous fitting techniques that could be used to extract the Stokes parameters from a set of data for $I(\beta)$, however a particularly elegant solution uses trigonometric identities to re-express equation 7.7 as a truncated Fourier series with the dependence on Δ and γ absorbed into the coefficients,

$$I(\beta) = \frac{a_0}{2} + a_2\cos(2\beta) + b_2\sin(2\beta) + a_4\cos(4\beta) + b_4\sin(4\beta). \tag{7.8}$$

This approach places additional restrictions on the data set used, requiring points evenly spaced in β, covering the range $0 \to \pi$ or $0 \to 2\pi$. The coefficients can be obtained in the usual manner using the orthogonality of the trigonometric functions. For a set of N intensity values at equally spaced values of β in the range $0 \to (N-1)\pi/N$, with $\beta_i = (i-1)\pi/N$,

$$a_n = \frac{2}{N}\sum_{i=1}^{N} I_i\cos(n\beta_i), \tag{7.9}$$

$$b_n = \frac{2}{N}\sum_{i=1}^{N} I_i\sin(n\beta_i). \tag{7.10}$$

Having calculated the Fourier coefficients using the known intensity values, $\{I_i\}$, and their associated retarder angles, $\{\beta_i\}$, the Stokes parameters can be calculated

provided that Δ and γ are also known,

$$S_0 = \frac{a_0}{2} - \frac{1+\cos\Delta}{1-\cos\Delta}\left[a_4\cos(4\gamma) + b_4\sin(4\gamma)\right], \tag{7.11}$$

$$S_1 = \frac{2}{1-\cos\Delta}\left[a_4\cos(2\gamma) + b_4\sin(2\gamma)\right], \tag{7.12}$$

$$S_2 = \frac{2}{1-\cos\Delta}\left[b_4\cos(2\gamma) - a_4\sin(2\gamma)\right], \tag{7.13}$$

$$S_3 = \frac{a_2}{\sin\Delta\sin(2\gamma)} = -\frac{b_2}{\sin\Delta\cos(2\gamma)}. \tag{7.14}$$

Equations 7.9 and 7.10 remain valid for a set of measurements at equally spaced values of β_i covering the range $0 \to 2\pi$, and this extended range can compensate for systematic errors due to spatial inhomogeneities in the retarder.

7.2 A calibrated rotating quarter-wave plate method

The accuracy of the Stokes parameters obtained from equations 7.11–7.14 depends upon the accuracy with which $\{\beta_i\}$, γ and Δ are known. In general there is an unknown offset, β_0, in the azimuthal angle of the retarder given by the initial angle of the fast axis relative to the reference axis (labelled with $\hat{\mathbf{x}}$). The fixed angle, γ, of the linear polarizer transmission axis relative to this reference axis is subject to experimental uncertainty, and the retarder phase, Δ, is subject to manufacturing tolerances in addition to variations with temperature [143], stress [144], and angle-of-incidence [52]. Additionally, for a given birefringence the retardance is inversely proportional to source wavelength, an issue that can be exacerbated (or alleviated) by the dispersion of birefringence with wavelength [145]. For incident light with vacuum

wavelength, λ, and a wave plate with birefringence, $\Delta n(\lambda)$, and thickness, d, the retardance is given by,

$$\Delta = \frac{2\pi|\Delta n(\lambda)|d}{\lambda}. \tag{7.15}$$

The combined effects of all these uncertainties on the measured Stokes parameters can be rather dramatic and yet they can be challenging to eliminate and are seldom taken into consideration. As an example, an unaccounted-for offset in the retarder angle of $\beta_0 = +3°$, along with a +1 % error in the retardance, Δ, introduces a 13 % error in the normalized Stokes parameter, S_1, for horizontally polarized light, for which unity would otherwise be expected.

It is clear then that the determination of accurate *Stokes parameters* depends critically on having accurate values for the *polarimeter parameters*, β_0, Δ, and γ.

7.2.1 Theory of the calibration method

A calibration method that may be used to reduce all of these uncertainties was previously developed by Prof. Robert L. Brooks during his doctoral research at the University of Alberta [146, 147]. The technique used incident light with a known linear polarization and an assumed value of Δ, with the offset of the optic axes of the retarder and linear polarizer from the horizontal reference axis determined self-consistently from four sets of measurements corresponding to each of the two optical elements either forward or reversed due to rotation about a vertical axis. Recognizing that reversing an optic has no effect if its optic axis is either parallel or perpendicular to the vertical rotation axis, the results of the four sets of measurements will give consistent Stokes parameters only when β_0 and γ are correctly accounted for. Subsequently, a correction to Δ from the assumed value was made using two additional sets

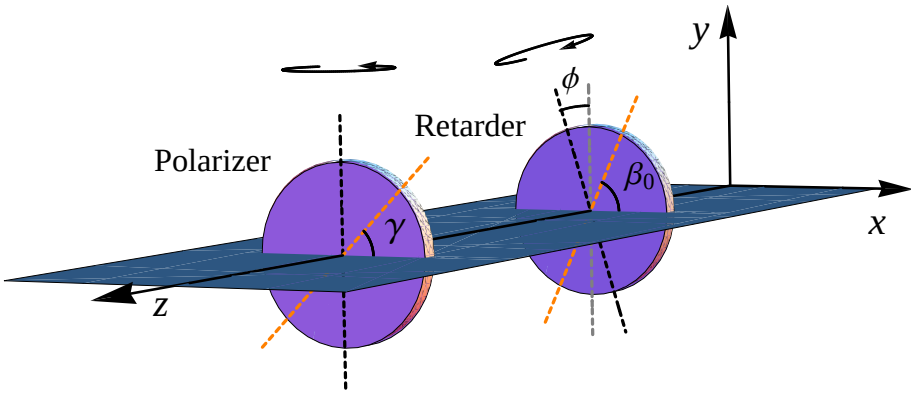

Figure 7.1: An illustration of the relevant angles for the calibrated rotating quarter-wave plate method (angles have been exaggerated for clarity). The angle of the transmission axis of the linear polarizer and the initial angle of the retarder fast axis from the reference axis, $\hat{\mathbf{x}}$, are denoted γ and β_0 respectively. The front-to-back rotation axis of the polarizer defines $\hat{\mathbf{y}}$ and the misalignment of the retarder's front-to-back rotation axis from this is denoted ϕ.

of measurements with vertically polarized incident light and the transmission axis of the linear polarizer first aligned and then crossed with respect to this polarization. This full process was repeated iteratively to obtain convergence of the parameters, β_0, Δ and γ.

The calibration method presented herein [148] accomplishes the accurate determination of these parameters in a single experimental step and also takes into account the presence of a misalignment between the assumed-vertical rotation axes of the retarder and polarizer. Introducing a fourth polarimeter parameter denoted by ϕ, a small value of this misalignment can introduce significant errors into the calibration and hence also into all subsequently measured Stokes parameters based on the calibration. All of the relevant axes and angles are defined in figure 7.1.

For the case of $\beta_0 \neq 0$, the expressions for the Fourier coefficients in equations

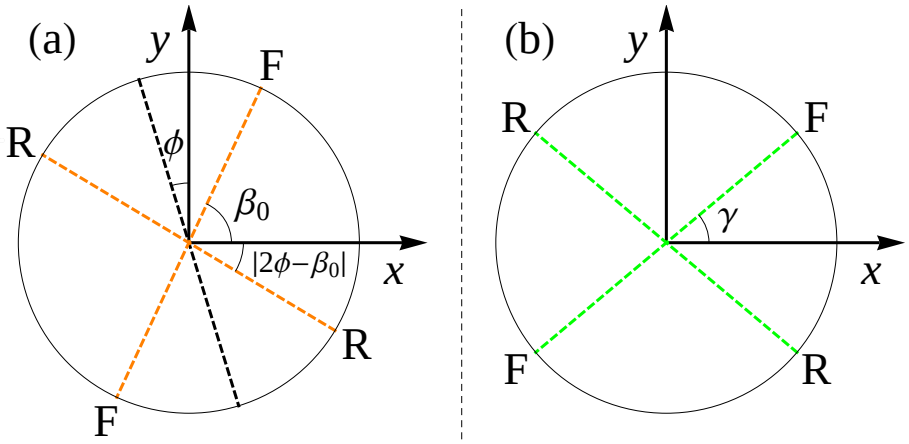

Figure 7.2: (a) Relative orientations of the retarder fast axis for cases 1 and 3 (F), and 2 and 4 (R), where β_0 denotes the angle of the fast axis relative to $\hat{\mathbf{x}}$ and ϕ denotes the offset of the front-to-back rotation axis of the retarder from that of the polarizer. (b) Relative positions of the polarizer transmission axis for cases 1 and 2 (F), and 3 and 4 (R), where γ denotes the angle of the transmission axis relative to $\hat{\mathbf{x}}$.

7.9 and 7.10 can be corrected by simply replacing β_i with $\beta_i + \beta_0$, however the efficiency of the calibration process can be improved by using the trigonometric sum–difference formulae to factor the dependence on β_0 out of the Fourier coefficients and absorbing them into equations 7.11–7.14. Reversing each optic about the vertical axis is equivalent to reflecting the optic axes in the horizontal reference axis such that $\{\beta_0, \gamma\} \rightarrow \{-\beta_0, -\gamma\}$. The horizontal reference axis, $\hat{\mathbf{x}}$, is defined to be perpendicular to both the beam axis, $\hat{\mathbf{z}}$, and the front-to-back rotation axis of the *polarizer* so the offset, ϕ, of the retarder's front-to-back rotation axis relative to that of the polarizer must be accounted for, such that in actual fact $\{\beta_0, \gamma\} \rightarrow \{2\phi - \beta_0, -\gamma\}$. Figure 7.2 depicts this process.

With the two polarimeter optics each used in both 'forward' (F) and 'reversed' (R) configurations, four cases have been defined, as listed for reference in table 7.1. The formulae for the Stokes parameters with both optics forward (case 1) and with

Table 7.1: Front-to-back orientations of the polarimeter optics for the four cases. The initial orientation is defined as 'forward' (F), while reversal about a vertical rotation axis corresponds to 'reversed' (R).

	Retarder	Polarizer
Case 1	F	F
Case 2	R	F
Case 3	F	R
Case 4	R	R

only the linear polarizer reversed (case 3) are,

$$S_0^{(1,3)} = \frac{a_0}{2} - \frac{1+\cos\Delta}{1-\cos\Delta}\left\{a_4\cos[4(\gamma \mp \beta_0)] \pm b_4\sin[4(\gamma \mp \beta_0)]\right\}, \tag{7.16}$$

$$S_1^{(1,3)} = \frac{2}{1-\cos\Delta}\left\{a_4\cos[2(\gamma \mp 2\beta_0)] \pm b_4\sin[2(\gamma \mp 2\beta_0)]\right\}, \tag{7.17}$$

$$S_2^{(1,3)} = \frac{2}{1-\cos\Delta}\left\{b_4\cos[2(\gamma \mp 2\beta_0)] \mp a_4\sin[2(\gamma \mp 2\beta_0)]\right\}, \tag{7.18}$$

$$S_3^{(1,3)} = \pm\frac{a_2}{\sin\Delta\sin[2(\gamma \mp \beta_0)]} = -\frac{b_2}{\sin\Delta\cos[2(\gamma \mp \beta_0)]}, \tag{7.19}$$

where the upper sign corresponds to case 1 and the lower sign to case 3. For the cases with *only* the retarder reversed (case 2) and with both optics reversed (case 4), the Stokes parameters are given by,

$$S_0^{(2,4)} = \frac{a_0}{2} - \frac{1+\cos\Delta}{1-\cos\Delta}\left\{a_4\cos[4(\gamma \pm \beta_0 \mp 2\phi)] \pm b_4\sin[4(\gamma \pm \beta_0 \mp 2\phi)]\right\}, \tag{7.20}$$

$$S_1^{(2,4)} = \frac{2}{1-\cos\Delta}\left\{a_4\cos[2(\gamma \pm 2\beta_0 \mp 4\phi)] \pm b_4\sin[2(\gamma \pm 2\beta_0 \mp 4\phi)]\right\}, \tag{7.21}$$

$$S_2^{(2,4)} = \frac{2}{1-\cos\Delta}\left\{b_4\cos[2(\gamma \pm 2\beta_0 \mp 4\phi)] \mp a_4\sin[2(\gamma \pm 2\beta_0 \mp 4\phi)]\right\}, \tag{7.22}$$

$$S_3^{(2,4)} = \pm\frac{a_2}{\sin\Delta\sin[2(\gamma \pm \beta_0 \mp 2\phi)]} = -\frac{b_2}{\sin\Delta\cos[2(\gamma \pm \beta_0 \mp 2\phi)]}, \tag{7.23}$$

where the upper sign corresponds to case 2 and the lower sign to case 4. Because the

dependence on β_0 has been entirely absorbed into equations 7.16–7.23, the Fourier coefficients a_0–b_4 need only be calculated once for any number of trial values of β_0.

The two expressions in each of equations 7.19 and 7.23 are both valid for all values of the polarimeter parameters, however, for values of β_0, γ and ϕ for which the denominator approaches zero, the calculated value of S_3 becomes extremely sensitive to the effects of experimental uncertainties on the values of a_2 and b_2. The two expressions can be combined to derive an additional expression valid for all four cases, with no explicit dependence on these polarimeter parameters at the expense of losing any knowledge of the sign of S_3 [149],

$$\left|S_3^{(1,2,3,4)}\right| = \frac{\sqrt{a_2^2 + b_2^2}}{\sin\Delta}. \tag{7.24}$$

Once the polarimeter parameters have been accurately determined, an appropriate choice can be made of which expression to use to calculate the full value of S_3 including the sign.

If the correct values of the four polarimeter parameters are used, the Stokes parameters calculated for the four cases will be consistent. This suggests a form for a figure-of-merit for trial values of the polarimeter parameters based on the variances of the Stokes parameters across the four cases. For the sake of simplicity, incident light with linear polarization is used and hence S_3 is excluded from the calculation. Placing an additional linear polarizer (LP') before the polarimeter with its transmission axis set to ±22.5° or ±67.5° results in comparable values of S_1 and S_2 such that consistency of both parameters can be determined well above experimental uncertainties.

Initial attempts at calibration based on this simple figure-of-merit met with mixed

success. Through simulations of various experimental results based on different chosen polarimeter parameters it was determined that coupling between ϕ and the other polarimeter parameters can lead to Stokes parameters for different values of ϕ that are, within experimental uncertainty, equally consistent across the four cases. The presence of LP' ensures that the incident light is fully polarized for all cases, suggesting a supplementary condition, $P^{(j)} = 1$ for all j [50]. The inclusion of this additional condition does indeed distinguish between different values of ϕ, giving an error parameter used in the calibration procedure,

$$\xi = \sum_{j=1}^{4} \left[\left(\frac{S_1^{(j)}}{S_0^{(j)}} - \left\langle \frac{S_1}{S_0} \right\rangle \right)^2 + \left(\frac{S_2^{(j)}}{S_0^{(j)}} - \left\langle \frac{S_2}{S_0} \right\rangle \right)^2 + (1 - P^{(j)})^2 \right], \tag{7.25}$$

where the summation is over the four cases and here the angle brackets denote the arithmetic mean.

An approximate way to visualize this optimization approach is to consider the minimization of the area of the quadrilateral formed in the S_1–S_2 plane through the Poincaré sphere [150], as illustrated in figure 7.3. This description assumes that it is the variance in P rather than the sum of the squared differences from unity that contributes to ξ, however for reasonable choices for the trial polarimeter parameters these values are likely to be very similar.

Experimental uncertainties notwithstanding, the minimum value of ξ occurs at the location in the four-dimensional parameter space, $\{\beta_0, \Delta, \gamma, \phi\}$, where these parameters take their true values.

Throughout this chapter it has been assumed that β_0 gives the initial angle of the *fast axis* of the retarder from $\hat{\mathbf{x}}$. The only difference in the Stokes parameters following an exchange of fast and slow axes (a 90° azimuthal rotation) is a change

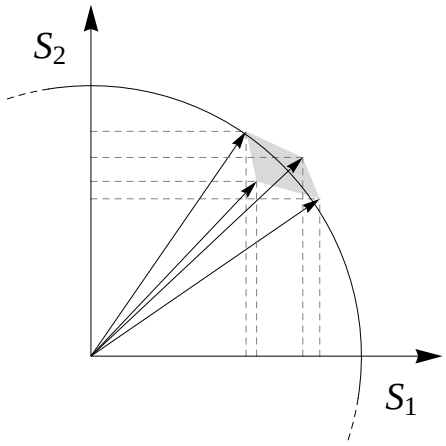

Figure 7.3: An approximate visual model of the error parameter, ξ. Increase in the scatter of S_1, S_2 and P increases the size of the quadrilateral formed by the end points of the Stokes vectors for the four cases anchored at the origin of the Poincaré sphere. Strictly it is deviation of P from unity that contributes to ξ but for reasonable trial polarimeter parameters this will be similar to the scatter.

in the sign of S_3 and so the calibration process, for which only the square of S_3 is included in ξ, is insensitive to this change. If the sign of S_3 is needed, an additional measurement may be made on light that has passed through a circular polarizer to resolve this ambiguity.

7.2.2 Experimental setup

As with all rotating quarter-wave plate polarimeters, the light under test must pass through a retarder in a rotatable mount followed by a linear polarizer and then a transducer of some kind to measure the transmitted intensity. Details of the experimental setup used in the current work are shown in figure 7.4. The beam under test is coupled into a single-mode optical fiber with the output beam-diameter increased by a factor of four using a beam expander consisting of a pair of plano-convex lenses with focal lengths of 2.5 cm and 10 cm, arranged with a common focal point.

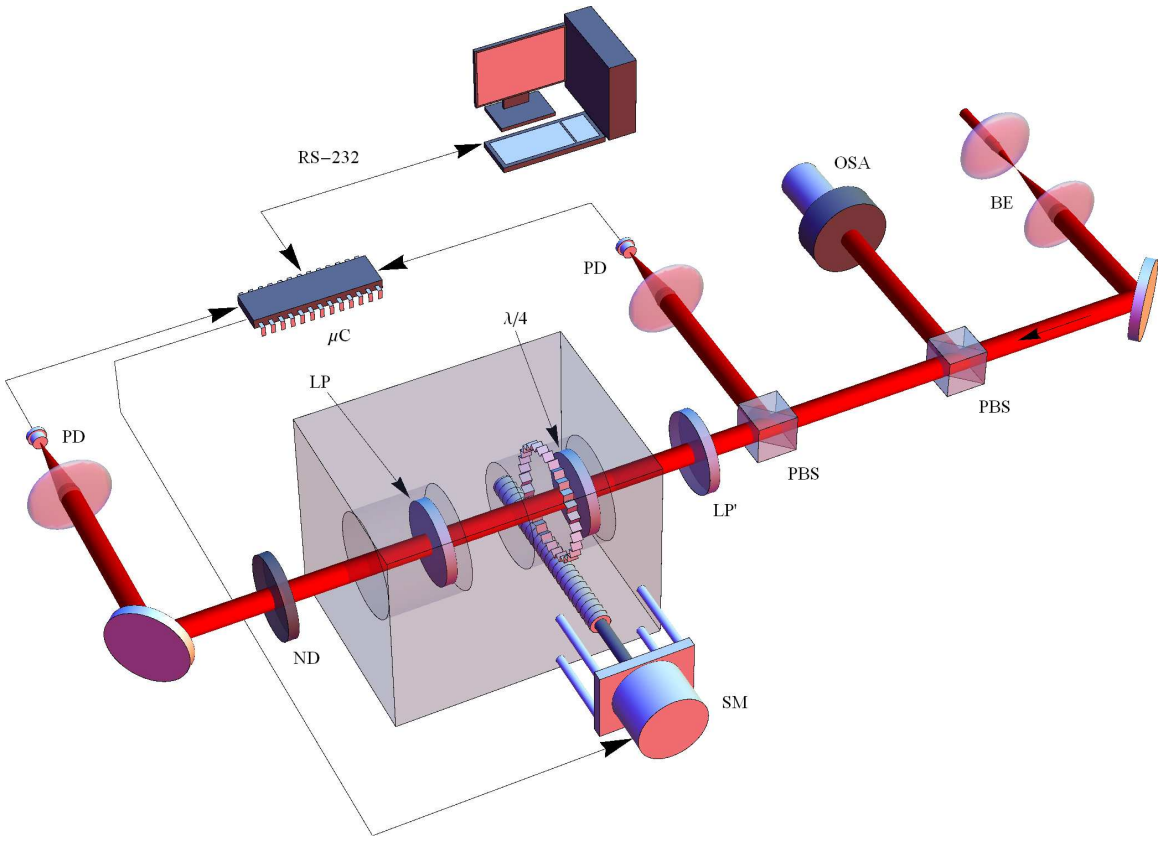

Figure 7.4: Schematic of the experimental polarimeter setup. The beam under test originates from a fiber-coupled external-cavity diode laser. A beam-expander (BE) increases the beam-width to ~ 8 mm. A pair of polarizing beam-splitters (PBS) produce a horizontally-polarized beam with which to test the calibration method. The first s-polarized reflection is sent to an optical spectrum analyzer (OSA), while the weak second reflection serves as a reference for power normalization. The polarimeter itself consists of a quarter-wave plate ($\lambda/4$) and linear polarizer (LP) in rotational mounts. The calibration method employs an additional linear polarizer (LP$'$) set to make $S_1 \approx S_2$ and is removed for regular beam analysis. The retarder is rotated via a worm gear by the stepper motor (SM) and the transmitted light is measured by a photodiode (PD) after attentuation by a neutral density filter (ND). The microcontroller (μC) controls the SM and records the PD voltages for transmission to a computer.

This arrangement ensures the incident beam is only slightly smaller than the polarimeter optics, hence averaging over spatial non-uniformities. A pair of polarizing beam-splitters (PBS) produce a horizontally polarized beam with which to test the calibration method, with the first vertically polarized reflection sent to an optical spectrum analyzer to monitor the mode-stability of the source laser, and the weak reflection from the second PBS focused onto a photodiode to monitor variations in the intensity of the light incident on the polarimeter optics. During the calibration process an additional linear polarizer (LP') is placed after the PBSs with its transmission axis at 22.5° as measured from $\hat{\mathbf{x}}$.

The polarimeter itself consists of a retarder and linear polarizer in rotational mounts, with the azimuthal orientation of the retarder controlled by a worm-gear for which one full rotation advanced the rotational mount by 3.6°. Both rotational mounts can sit in their respective positions in the polarimeter in either a forward or reversed configuration, permitting easy reversal of either optic. A stepper motor controls the worm-gear driving the retarder mount, with one step advancing the worm-gear by 1.8° and hence setting the azimuthal orientation of the retarder to a precision of $0.018° \approx 1$ minute of arc. The stepper motor was driven by a pair of UC3770AN stepper motor driver ICs controlled by a single PIC18LF2320 microcontroller [151].

Light having passed through the polarimeter optics was focused onto a photodiode after being attenuated by a neutral density filter chosen to maximize the dynamic range of the detected signal while avoiding saturating the detector. In addition to controlling the orientation of the retarder, the microcontroller also collects intensity readings from the photodiodes before and after the polarimeter using its 10-bit analog-to-digital conversion capability. A measurement process is initiated and the

resulting intensity data collected via a two-way RS-232 serial connection between the microcontroller and computer runnning MATLAB.

7.2.3 Calibration procedure

Before beginning a calibration measurement an optic axis of the retarder must be aligned parallel with $\hat{\mathbf{x}}$ by retroreflecting a horizontally polarized beam through the retarder and minimizing the vertically polarized component of the returning beam using a PBS. The calibration process is most robust with $|\beta_0 - \gamma| \approx (45° \bmod 90°)$; the transmission axis of the polarizer can be aligned at 45° to $\hat{\mathbf{x}}$ by placing a PBS after the polarizer and rotating it until there is equal power in the s- and p-polarized components.

The calibration process begins with the collection of the intensity data for each of the four cases. The experimental apparatus described in section 7.2.2 automates the process of obtaining the intensity data for each case, accelerating the process and reducing the chance of unwanted effects due to drifts in the properties of the light source, however this automation is not essential to the calibration technique. The requirement is simply a set of N relative intensity values (a constant scaling factor does not affect the normalized Stokes vector) at a set of equally spaced retarder angles, $\{\beta_i\}$. The minimum number of values for the Fourier analysis outlined above is $N = 5$, although it is advisable to use a minimum of $N = 10$ and for the results presented below a value of $N = 50$ was used. Recall that the incident polarization should be set to give comparable values of S_1 and S_2 (linearly polarized at ±22.5° or ±67.5°).

A computational analysis must be performed on the intensity data for the four

cases. Fourier coefficients for each of the four cases are calculated using equations 7.9 and 7.10. Stokes parameters and degrees-of-polarization are then obtained for the four cases using 11 trial values spaced by 0.02 radians for each of the four polarimeter parameters. The initial parameter ranges used are:

$$-0.1 \leq \beta_0 \leq +0.1, \tag{7.26}$$

$$\left(\frac{\lambda_{\pi/2}^{\text{nom}}}{\lambda_{\text{opt}}}\right)\frac{\pi}{2} - 0.1 \leq \Delta \leq \left(\frac{\lambda_{\pi/2}^{\text{nom}}}{\lambda_{\text{opt}}}\right)\frac{\pi}{2} + 0.1, \tag{7.27}$$

$$\frac{\pi}{4} - 0.1 \leq \gamma \leq \frac{\pi}{4} + 0.1, \tag{7.28}$$

$$-0.1 \leq \phi \leq +0.1. \tag{7.29}$$

These ranges should be sufficient to encompass the manufacturing and experimental uncertainties for most retarders in standard conditions and the experimental uncertainties in the various angles.

This process is continued iteratively, halving the spacing each time and using as the central values for the polarimeter parameter ranges that set of values that minimized ξ in the previous iteration. Convergence to a clear result should be achieved in no more than 8 iterations.

To summarize, the procedure for the calibration process is as follows:

1. Align an optic axis of the retarder with $\hat{\mathbf{x}}$
2. Align the polarizer transmission axis at 45° from $\hat{\mathbf{x}}$
3. Ensure incident light is linearly polarized at ±22.5° or ±67.5° to the horizontal reference axis
4. Case 1 (FF): Take a set of N intensity reading with the retarder oriented at N equally spaced angles between 0 and $(N-1)2\pi/N$

5. Case 2 (RF): Reverse the retarder mount by rotating about a vertical axis and repeat step 2
6. Case 4 (RR): Reverse the polarizer mount by rotating about a vertical axis and repeat step 2
7. Case 3 (FR): Reverse the retarder mount again and repeat step 2
8. Obtain Stokes parameters and degrees-of-polarization for the four cases using equations 7.16–7.19 and 7.20–7.23 for each of 11 values for the polarimeter parameters: β_0, Δ, γ and ϕ, spaced by 0.02 radians and centred at a 'best guess' value for each parameter
9. Repeat the search process with the spacing of trial parameter values halved (0.01 radians) and centred upon the set of polarimeter parameters associated with the minimum value of ξ as defined by equation 7.25
10. Continue the four dimensional search process iteratively to convergence, typically 8 iterations
11. Check that the final set of polarimeter parameters give Stokes parameters for the four cases consistent with one another and with the known incident polarization

7.2.4 Simulated analysis of the calibration

An analysis of the calibration technique was made by choosing specific values for the polarimeter parameters, $\{\beta_0, \Delta, \gamma, \phi\} = \{2°, 0.26 \times 2\pi \approx 93.6°, 44°, 1°\}$, and a Stokes vector for light linearly polarized at +67.5°, $\mathbf{S} = \{1, -1/\sqrt{2}, 1/\sqrt{2}, 0\}$, and generating simulated intensity data with a SNR of 40 (typical of the experimental data analyzed in section 7.2.5). Analysis of the simulated data yielded the results $\{\beta_0^{\text{calc}}, \Delta^{\text{calc}}, \gamma^{\text{calc}}, \phi^{\text{calc}}\} = \{1.91°, 93.56°, 43.93°, 0.92°\}$. As an illustration of how ξ varies with different trial polarimeter parameters, figure 7.5 shows the dependence of $\log_{10}[\xi(\beta_0, \Delta)]$ on β_0 and Δ using the calculated values, γ^{calc} and ϕ^{calc}. As expected

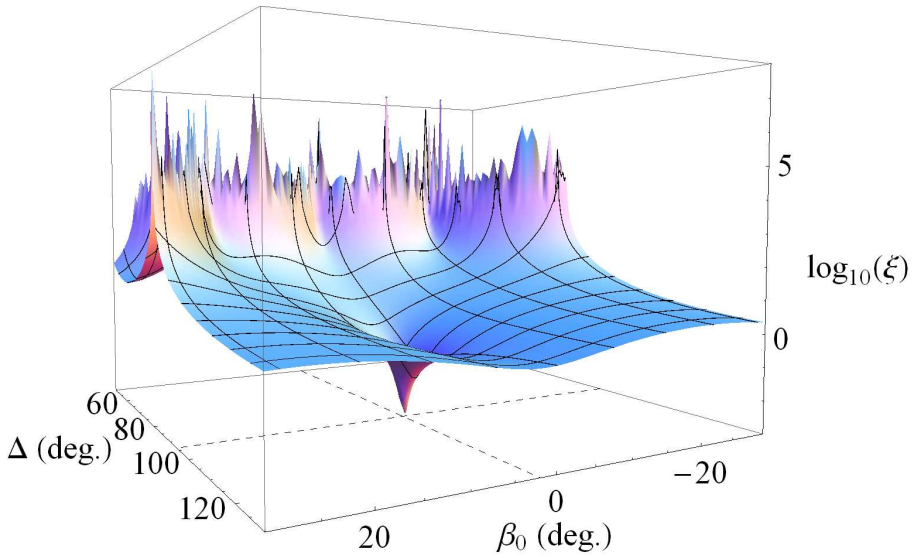

Figure 7.5: Global error surface showing the dependence of $\log_{10}[\xi(\beta_0, \Delta)]$ on β_0 and Δ. Data simulated using values, $\{\beta_0, \Delta, \gamma, \phi\} = \{2°, 0.26 \times 2\pi \approx 93.6°, 44°, 1°\}$ (correct β_0 and Δ values indicated by dashed lines), a Stokes vector for +67.5° linearly polarized light, and a SNR of 40. The values $\gamma = 43.93°$ and $\phi = 0.9221°$ were used having been obtained in the usual manner.

the surface has a global minimum at the correct values as indicated by the dashed lines.

The deleterious effect of the small misalignment between the front-to-back rotation axes of the retarder and polarizer, denoted ϕ, is illustrated in figure 7.6. Two error surfaces are plotted based on the same simulated data used for figure 7.5; the surface with a minimum indicated by dashed lines was calculated assuming $\phi = 0$, while the other surface used the calibrated value, $\phi = 0.92°$, with the result that the minimum falls very close to the correct values of β_0 and Δ.

As a test of the robustness of the calibration scheme to the presence of noise in the measured intensity data an analysis was made using different levels of random noise added to simulated data, determining the mean absolute differences between the calibrated polarimeter parameters and the corresponding chosen correct values.

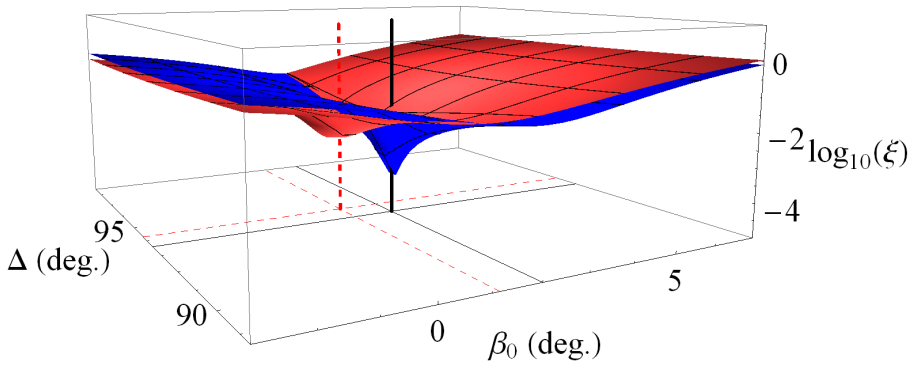

Figure 7.6: Local error surfaces showing the importance of including ϕ in the search. Simulated data identical to that used in figure 7.5. The red surface (minimum indicated by dashed lines) was calculated assuming $\phi = 0$, while the blue surface (minimum close to the correct values indicated by the solid lines) used the calibrated value, $\phi = 0.92°$.

The mean calibrated values were obtained from a set of 20 calibrations done at each of 41 different values of the SNR, using the same chosen parameter values that were used to produce figures 7.5 and 7.6. The results are shown in figure 7.7 indicating that a SNR of at least 7 should be sufficient to obtain the complete set of polarimeter parameters to better than 1°.

7.2.5 Experimental test of the calibration

A test of the calibration process was implemented using incident light at 672.7 nm from an AlGaInP diode laser, as discussed in section 6.1, along with three different mica zero-order quarter-wave retarders with design wavelengths, $\lambda_{\pi/2}^{\text{nom}} = \{670\,\text{nm}, 645\,\text{nm}, 548\,\text{nm}\}$. With knowledge of the birefringence of the material in question at $\lambda_{\pi/2}^{\text{nom}}$ and at the optical wavelength, these values can be converted into

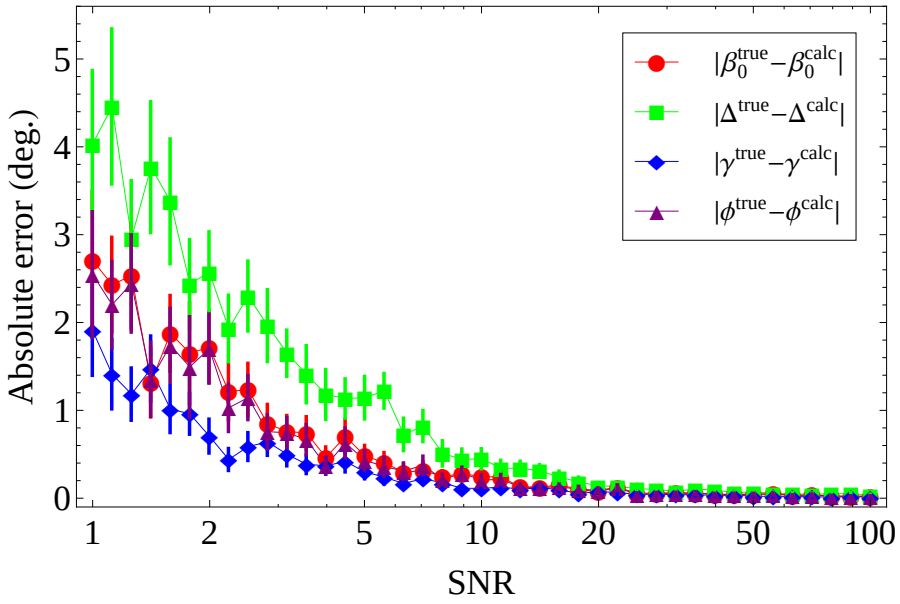

Figure 7.7: Calibration results for simulated data with random noise added. Each datum corresponds to the difference between the chosen correct parameter value and an average over 20 calibrations at the relevant value of the SNR. The data used to construct table 7.2 had SNR values in the range 40–61.

retarder phases at the optical wavelength, using equation 7.15 to obtain,

$$\Delta = \frac{\pi}{2} \frac{\lambda_{\pi/2}^{\mathrm{nom}} |\Delta n(\lambda_{\mathrm{opt}})|}{\lambda_{\mathrm{opt}} |\Delta n(\lambda_{\pi/2}^{\mathrm{nom}})|}. \tag{7.30}$$

Using data for the dispersion of birefringence with wavelength in mica [152] the calculated retardances are $\Delta = \{89.6°, 86.4°, 74.4°\}$. Note that inconsistencies in the published data for the dispersion of birefringence in mica make these values necessarily approximate [153].

In addition to the different retarders, three different intentional misalignments were chosen, corresponding to offsets between the front-to-back rotation axes of the polarizer and retarder of $\phi = \{-3.6°, 0°, +3.6°\}$, corresponding to $\{-1, 0, +1\}$ gear teeth on the rotational mount. The complete set of nine calibrations were taken with

Table 7.2: Experimental results for nine polarimeter calibrations using three different quarter-wave plates with design wavelengths denoted by $\lambda_{\pi/2}^{\mathrm{nom}}$, each with three different values of ϕ^{nom}.

ϕ^{nom}		$\lambda_{\pi/2}^{\mathrm{nom}}$ = 670 nm	$\lambda_{\pi/2}^{\mathrm{nom}}$ = 645 nm	$\lambda_{\pi/2}^{\mathrm{nom}}$ = 548 nm
+3.6°	β_0	3.34°	3.80°	1.16°
	Δ	90.47°	86.34°	75.12°
	γ	144.22°	144.31°	144.21°
	$\phi - \phi^{\mathrm{nom}}$	0.85°	0.82°	0.81°
0°	β_0	3.55°	3.79°	1.32°
	Δ	90.40°	86.28°	75.20°
	γ	144.29°	144.29°	144.22°
	$\phi - \phi^{\mathrm{nom}}$	0.94°	0.82°	0.85°
−3.6°	β_0	3.29°	3.78°	1.51°
	Δ	90.47°	86.30°	75.09°
	γ	144.22°	144.30°	144.17°
	$\phi - \phi^{\mathrm{nom}}$	0.77°	0.80°	0.87°
	$\langle\beta_0\rangle$	3.39(8)°	3.787(5)°	1.3(1)°
	$\langle\Delta\rangle$	90.45(2)°	86.31(2)°	75.13(3)°
	$\langle\gamma\rangle$		144.25(2)°	
	$\langle\phi - \phi^{\mathrm{nom}}\rangle$		0.84(2)°	

consistent linear incident polarization at 22.5° to give comparable values of S_1 and S_2, and in each case an additional set of intensity data was recorded using horizontally polarized light.

The results of the nine calibrations are presented in table 7.2. As expected the values of β_0 and Δ are consistent for a given retarder, while γ and $\phi - \phi^{\mathrm{nom}}$ remain consistent throughout the table. The systematic difference of ϕ from the nominally expected value can be ascribed to the fact that the starting position of the worm-gear controlling the azimuthal orientation of the retarder did not match that for the

polarizer and hence the retarder front-to-back rotation axis was not precisely 'vertical' as defined by the front-to-back rotation axis of the polarizer.

The retardance of commercial quarter-wave retarders is generally reported by giving $\lambda_{\pi/2}$, usually with a stated uncertainty of $\pm 0.01\lambda_{\pi/2}$. The retardances reported in table 7.2 can be converted into this form by finding the root of the equation,

$$\frac{\lambda_{\text{opt}}\Delta}{|\Delta n(\lambda_{\text{opt}})|} - \frac{\lambda_{\pi/2}(\pi/2)}{|\Delta n(\lambda_{\pi/2})|} = 0. \tag{7.31}$$

Using this method the actual wavelengths at which the three wave plates effect a quarter-wave retardance are $\lambda_{\pi/2} = \{676.2\,\text{nm}, 644.2\,\text{nm}, 554.6\,\text{nm}\}$.

As an additional test, the 670 nm wave plate was analyzed using light from an AlGaAs diode laser at 777.6 nm resulting in values $\beta_0 = 4.46°$, $\gamma = 144.15°$ and $\phi - \phi^{\text{nom}} = 1.88°$, all within 1° of the values obtained at 672.7 nm. The value $\Delta = 76.76°$ was obtained and is within 1° of the nominally expected value of $670/780 \times 90°$. The small variations observed may be attributed to the realignment required when changing the wavelength of light passed through the optical fiber.

To demonstrate the efficacy of the calibration technique for obtaining accurate Stokes parameters, an additional set of intensity data was taken with horizontally polarized incident light following each calibration set. The resulting normalized Stokes vectors are presented in table 7.3 showing highly consistent results across all nine calibrations. The mean values of the Stokes parameters and the derived degrees-of-polarization are given by

Table 7.3: Stokes vectors derived from measurements of horizontally polarized light using three different retarders and three intentional misalignments of the retarder vertical rotation axis using the nine calibrations presented in table 7.2.

ϕ^{nom}	$\lambda_{\pi/2}^{\text{nom}}$ = 670nm	$\lambda_{\pi/2}^{\text{nom}}$ = 645nm	$\lambda_{\pi/2}^{\text{nom}}$ = 548nm
+3.6°	$\begin{pmatrix} 1.000 \\ 0.992 \\ 0.120 \\ 0.016 \end{pmatrix}$	$\begin{pmatrix} 1.000 \\ 0.996 \\ 0.116 \\ 0.016 \end{pmatrix}$	$\begin{pmatrix} 1.000 \\ 0.990 \\ 0.128 \\ 0.015 \end{pmatrix}$
0°	$\begin{pmatrix} 1.000 \\ 0.998 \\ 0.128 \\ 0.016 \end{pmatrix}$	$\begin{pmatrix} 1.000 \\ 0.998 \\ 0.117 \\ 0.016 \end{pmatrix}$	$\begin{pmatrix} 1.000 \\ 0.992 \\ 0.122 \\ 0.014 \end{pmatrix}$
−3.6°	$\begin{pmatrix} 1.000 \\ 0.996 \\ 0.117 \\ 0.017 \end{pmatrix}$	$\begin{pmatrix} 1.000 \\ 1.001 \\ 0.115 \\ 0.017 \end{pmatrix}$	$\begin{pmatrix} 1.000 \\ 0.989 \\ 0.128 \\ 0.016 \end{pmatrix}$

$$\langle \mathbf{S} \rangle = \begin{pmatrix} 1 \\ 0.995 \pm 0.001 \\ 0.121 \pm 0.002 \\ 0.0158 \pm 0.0003 \end{pmatrix}, \tag{7.32}$$

and

$$\langle P \rangle = 1.002 \pm 0.001. \tag{7.33}$$

The non-zero value of S_3 indicates a consistent small ellipticity that may result from stress-induced birefringence in the PBS used to obtain horizontal polarization, while the values of S_1 and S_2 correspond to a $\sim 3^\circ$ misalignment between the PBS

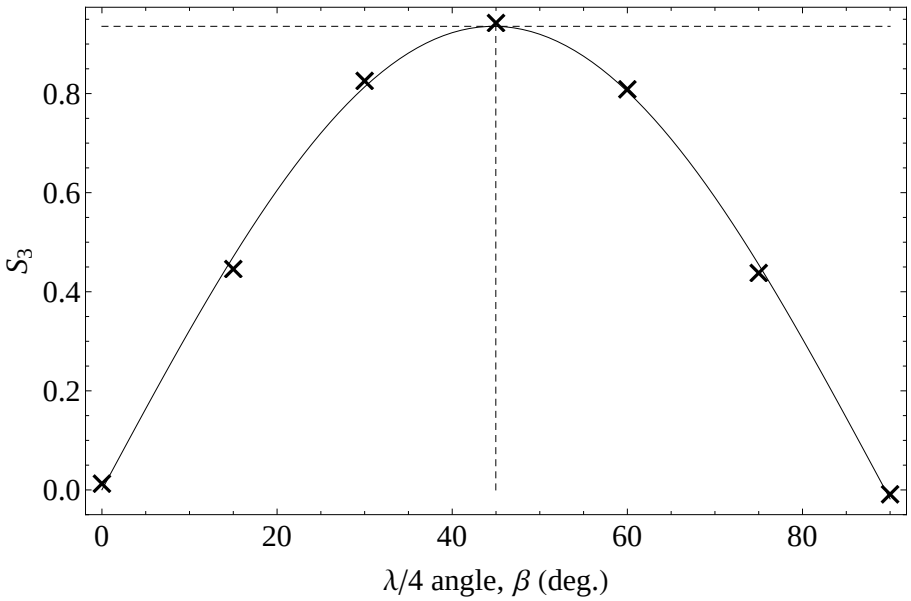

Figure 7.8: Variation in S_3 as a quarter-wave plate is rotated with incident horizontally polarized light. The solid line is a non-linear fit to the data, giving an optimal angle for maximizing S_3 of $\theta_{\text{opt}} = 45.0(9)^\circ$, with an optimized value of $S_3 = 0.94(1)$.

transmission axis and the horizontal reference axis, $\hat{\mathbf{x}}$. The mean value of P is approximately unity as expected for fully polarized light.

7.3 Application to the MOT experiment

The precise calibration technique described in this chapter will ensure that the effects of manufacturing tolerance and experimental errors can be minimized in all future polarization measurements made in the laboratory. An important application of this in the MOT experiment, described in chapter 6, is the obtaining of right-circular polarization ($S_3 = +1$) for the MOT beams to high precision.

Figure 7.8 shows a calibrated measurement of S_3 for an initially horizontally polarized beam after passing through a quarter-wave plate that was rotated through

90°, changing the output beam from horizontally polarized to right-circularly polarized and back to horizontal. Using a non-linear fit to the expected functional form the optimal angle that maximizes S_3 was obtained, $\theta_{\text{opt}} = 45.0(9)°$, with an optimized value of $S_3 = 0.94(1)$.

Chapter 8

Summary and Conclusions

Extensive theoretical and experimental work has demonstrated the fascinating behaviour and interactions exhibited by highly-excited molecular states and provided tools for their creation and investigation.

Analysis of high-resolution spectra of Rydberg states of HF demonstrated the effects of intramolecular perturbations on hyperfine structure and how these effects can be used to shed light on the underlying physics of the perturbations. A qualitative analysis showed how the amount of mixing between the C $^1\Pi$, $v = 0$ and B $^1\Sigma^+$, $v = 29$ vibronic levels varies with the rotational level, causing apparent variation in the a_F hyperfine parameter. A deperturbation analysis using the experimentally derived mixing fractions provided an unperturbed value, $a_F = 4132(25)$ MHz, from which the expectation value, $\langle r^{-3} \rangle_{1\pi} = 55.59$ Å^{-3}, was derived.

Anticipating future experimental studies of charge-exchange processes in collisions between ultracold alkali atoms, a theoretical investigation of ionic–covalent coupling energies was presented for all of the alkali–alkali systems for which the requisite anionic wave functions are available, including a large number of incoming collision

channels. The results, tabulated in appendix B, provide a basis for future calculations of cross-sections and rate-constants that will help to direct future experimental work.

The optical instrumentation required for magneto-optical trapping of ^{7}Li has been designed, constructed and tested in preparation for planned experiments. Systematic analysis of the different optical sub-systems has determined the optimal set of experimental parameters for operation of the system. These analyses included a novel scheme for systematic optimization of a peak-locking apparatus, a method for correcting an offset in the error-signal obtained using the side-of-filter offset-locking technique, and an analysis of the polarization characteristics of a 671 nm semiconductor tapered-amplifier used to obtain high power in the cooling and repumping beams to be used in the magneto-optical trap.

Given the critical nature of polarization at all stages in the optical setup for the magnetic-optical trap, the development of a calibrated polarimetry scheme permits further optimization of the apparatus, in addition to being a significant advance in its own right. This technique precisely corrects for a range of manufacturing and experimental uncertainties without requiring prior knowledge of most experimental parameters, and hence accounts for many of the systematics that can lead to inaccurate polarization measurements.

Bibliography

Introduction

[1] Bose–Einstein Condensation in a Gas of Sodium Atoms
K. B. Davis, M. -O. Mewes, M. R. Andrews, N. J. van Druten, D. S. Durfee, D. M. Kurn and W. Ketterle
Physical Review Letters **75** (22) 3969-3973 (1995)

[2] Evidence of Bose–Einstein Condensation in an Atomic Gas with Attractive Interactions
C. C. Bradley, C. A. Sackett, J. J. Tollett and R. G. Hulet
Physical Review Letters **75** (9) 1687-1690 (1995)

[3] Formation of Spatial Shell Structure in the Superfluid to Mott Insulator Transition
S. Fölling, A. Widera, T. Müller, F. Gerbier and I. Bloch
Physical Review Letters **97** (6) 060403 [4 pages] (2006)

[4] Observation of Fermi Pressure in a Gas of Trapped Atoms
A. G. Truscott, K. E. Strecker, W. I. McAlexander, G. B. Partridge and R. G. Hulet
Science **291** (5513) 2570–2572 (2001)

[5] Formation of Ultracold Polar Molecules in the Rovibrational Ground State
J. Deiglmayr, A. Grochola, M. Repp, K. Mörtlbauer, C. Glück, J. Lange, O. Dulieu, R. Wester and M. Weidemüller
Physical Review Letters **101** (13) 133004 [4 pages] (2008)

[6] Ultracold Chemistry
J. M. Hutson
Science **327** (5967) 788–789 (2010)

[7] The molecular electronic structure of the twenty-six lowest lying states of Li_2 at short and intermediate internuclear separations
D. D. Konowalow and J. L. Fish
Chemical Physics **84** (3) 463–475 (1984)

[8] Atomic Energy Levels
Charlotte E. Moore
National Bureau of Standards Circular 467 (1949)

[9] Magnetooptic trapping of lithium using semiconductor lasers
U. Schünemann, H. Engler, M. Zielonkowski, M. Weidemüller and R. Grimm
Optics Communications **158** 263-272 (1998)

Literature Review

[10] Rydberg Atoms
Thomas F. Gallagher
Oxford University Press, Oxford (1994)

[11] Peter M. Koch
Rydberg States of Atoms and Molecules
Cambridge University Press, Cambridge (1983)

[12] Realization of Localized Bohr-Like Wave Packets
J. J. Mestayer, B. Wyker, J. C. Lancaster, F. B. Dunning, C. O. Reinhold, S. Yoshida and J. Burgdörfer
Physical Review Letters **100** (24) 243004 [4 pages] (2008)

[13] Der stetige Übergang von der Mikro- zur Makro-mechanik
E. Schrödinger
Die Naturwissenschaften **14** (28) 664-666 (1926)

[14] Dipole blockade in a cold Rydberg atomic sample
D. Comparat and P. Pillet
Journal of the Optical Society of America B **27** (6) A208–A232 (2010)

[15] Entanglement of two ground state neutral atoms using Rydberg blockade
Y. Miroshnychenko, A. Browaeys, C. Evellin, A. Gaetan, T. Wilk, J. Wolter, P. Grangier, A. Chotia, D. Comparat, P. Pillet and M. Viteau
Optics and Spectroscopy **111** (4) 540–546 (2011)

[16] Observation of ultralong-range Rydberg molecules
V. Bendkowsky, B. Butscher, J. Nipper, J. Shaffer, R. Löw and T. Pfau
Nature **458** (7241) 1005–1008 (2009)

[17] Formation of heavy-Rydberg ion-pair states in collisions of K(np) Rydberg atoms with attaching targets
M. Cannon and F. B. Dunning
Journal of Chemical Physics **130** (4) 044304 [9 pages] (2009)

[18] Observation of a Rydberg Series in H^+–H^-: A Heavy Bohr Atom
M. O. Vieitez, T. I. Ivanov, E. Reinhold, C. A. de Lange and W. Ubachs
Physical Review Letters **101** (16) 163001 [4 pages] (2008)

[19] New observation of the $^6Li^7Li$ $3\,^3\Sigma_g^+$, $1\,^3\Delta_g$, and $2\,^3\Pi_g$ states and molecular constants with all $^6Li_2$, $^7Li_2$, and $^6Li^7Li$ data
D. Li, F. Xie, L. Li, A. Lazoudis and A. M. Lyyra
Journal of Molecular Spectroscopy **246** (2) 180–186 (2007)

[20] On the inverse Born–Oppenheimer separation for high Rydberg states of molecules
F. Remacle and R. D. Levine
International Journal of Quantum Chemistry **67** (2) 85-100 (1998)

[21] Observation of Na_2 Rydberg states and autoionization resonances by high resolution all-optical triple resonance spectroscopy
C. -C. Tsai, J. T. Bahns and W. C. Stwalley
Chemical Physics Letters **236** (6) 553–557 (1995)

[22] Rydberg states of the Li_2 molecule studied by polarization labelling spectroscopy
A. Grochola, P. Kowalczyk and W. Jastrzebski
Journal of Physics B: Atomic, Molecular and Optical Physics **43** (15) 1–5 (2010)

[23] High-resolution laser spectroscopy of ultracold ytterbium atoms using spin-forbidden electric quadrupole transition
S. Uetake, A. Yamaguchi, D. Hashimoto and Y. Takahashi
Applied Physics B **93** (2) 409–414 (2008)

[24] Coherent control of ultracold collisions with chirped light: Direction matters
M. J. Wright, J. A. Pechkis, J. L. Carini, S. Kallush, R. Kosloff and P. L. Gould
Physical Review A **75** (5) 051401 [4 pages] (2007)

[25] Diagnostics and loading of an atomic optical dipole trap
K. Brzozowski, L. Krzemien, J. Zachorowski and W. Gawlik
Optica Applicata **40** (3) 557–563 (2010)

[26] Rydberg atoms in magnetic quadrupole traps
I. Lesanovsky, J. Schmiedmayer and P. Schmelcher
Europhysics Letters **65** (4) 478–484 (2004)

[27] Bose-Einstein condensation in the alkali gases: Some fundamental concepts
A. J. Leggett
Reviews of Modern Physics **73** (2) 307–356 (2001)

[28] Cooling of gases by laser radiation
T. W. Hänsch and A. L. Schawlow
Optics Communications **13** (1) 68-69 (1975)

[29] Experimental investigation of the limit of Sisyphus cooling
J. Jersblad, H. Ellmann and A. Kastberg
Physical Review A **62** (5) 051401 [4 pages] (2000)

[30] Cooling Bose-Einstein Condensates Below 500 Picokelvin
A. E. Leanhardt, T. A. Pasquini, M. Saba, A. Schirotzek, Y. Shin, D. Kielpinski, D. E. Pritchard and W. Ketterle
Science **301** (5639) 1513–1515 (2003)

[31] Ultracold dipolar gases in optical lattices
C. Trefzger, C. Menotti, B. Capogrosso-Sansone and M. Lewenstein
Journal of Physics B: Atomic, Molecular and Optical Physics **44** (19) 193001 [31 pages] (2011)

[32] Bloch oscillations of cold atoms in two-dimensional optical lattices
A. R. Kolovsky and H. J. Korsch
Physical Review A **67** (6) 063601 [9 pages] (2003)

[33] Quantum phase transition from a superfluid to a Mott insulator in a gas of ultracold atoms
M. Greiner, O. Mandel, T. Esslinger, T. W. Hänsch and I. Bloch
Nature **415** (6867) 39-44 (2002)

[34] Precision Measurements on a Tunable Mott Insulator of Ultracold Atoms
M. J. Mark, E. Haller, K. Lauber, J. G. Danzl, A. J. Daley and H. -C. Nägerl
Physical Reviews Letters **107** (17) 175301 [5 pages] (2011)

[35] Many-body physics with ultracold gases
I. Bloch, J. Dalibard and W. Zwerger
Reviews of Modern Physics **80** (3) 885-964 (2008)

[36] Fermi-Hubbard Physics with Atoms in an Optical Lattice
T. Esslinger
Annual Review of Condensed Matter Physics **1** (1) 129–152 (2010)

[37] Formation of ultracold Rb_2 molecules in the $v'' = 0$ level of the $a\,^3\Sigma_u^+$ state via blue-detuned photoassociation to the $1\,^3\Pi_g$ state
M. A. Bellos, D. Rahmlow, R. Carollo, J. Banerjee, O. Dulieu, A. Gerdes, E. E. Eyler, P. L. Gould and W. C. Stwalley
Physical Chemistry Chemical Physics **13** (42) 18880–18886 (2011)

[38] Stark deceleration and trapping of OH radicals
S. Y. T. van de Meerakker, N. Vanhaecke and G. Meijer
Annual Review of Physical Chemistry **57** 159–190 (2006)

[39] Buffer-gas cooling of atomic and molecular beams
D. Egorov, T. Lahaye, W. Schöllkopf, B. Friedrich and J. M. Doyle
Physical Review A **66** (4) 043401 [8 pages] (2002)

[40] Laser cooling of a diatomic molecule
E. S. Shuman, J. F. Barry and D. DeMille
Nature **467** (7317) 820–823 (2010)

[41] Cold and ultracold molecules: science, technology and applications
L. D. Carr, D. DeMille, R. V. Krems and J. Ye
New Journal of Physics **11** (5) 1–87 (2009)

[42] Grating efficiency theory as it applies to blazed and holographic gratings
E. G. Loewen, M. Neviére and D. Maystre
Applied Optics **16** (10) 2711–2721 (1977)

[43] A compact grating-stabilized diode laser system for atomic physics
L. Riccia, M. Weidemüller, T. Esslinger, A. Hemmerich, C. Zimmermann, V. Vuletic, W. König and T. W. Hänsch
Optics Communications **117** (5) 541–549 (1995)

[44] A simple extended-cavity diode laser
A. S. Arnold, J. S. Wilson and M. G. Boshier
Review of Scientific Instruments **69** (3) 1236–1239 (1998)

[45] Compact external-cavity diode laser with a novel transmission geometry
M. Merimaaa, H. Talvitie, P. Laakkonen, M. Kuittinen, I. Tittonen and E. Ikonen
Optics Communications **174** (1) 175–180 (2000)

[46] High-resolution grazing incidence plane grating monochromator for undulator radiation
M. Koike and T. Namioka
Review of Scientific Instruments **66** (2) 2144–2146 (1995)

[47] Spectrally narrow pulsed dye laser without beam expander
M. G. Littman and H. J. Metcalf
Applied Optics **17** (14) 2224–2227 (1978)

[48] External-cavity diode laser using a grazing-incidence diffraction grating
K. C. Harvey and C. J. Myatt
Optics Letters **16** (12) 910–912 (1991)

[49] Self-Aligned Extended-Cavity Diode Laser Stabilized by the Zeeman Effect on the Cesium D2 Line
S. Lecomte, E. Fretel, G. Mileti and P. Thomann
Applied Optics **39** (9) 1426–1429 (2000)

[50] Rotating-Wave-Plate Stokes Polarimeter for Differential Group Delay Measurements of Polarization-Mode Dispersion
P. A. Williams
Applied Optics **38** (31) 6508–6515 (1999)

[51] Error Analysis of a Rotating Quarter-Wave Plate Stokes' Polarimeter
C. Flueraru, S. Latoui, J. Besse and P. Legendre
IEEE Transactions on Instrumentation and Measurement **57** (4) 731–735 (2008)

[52] Optimizing imaging polarimeters constructed with imperfect optics
J. S. Tyo and H. Wei
Applied Optics **45** (22) 5497–5503 (2006)

Molecular Rydberg state perturbations

[53] Rotational Spectroscopy of Diatomic Molecules
John Brown and Alan Carrington
Cambridge University Press, Cambridge (2003)

[54] Perturbations in the Spectra of Diatomic Molecules
Hélène Lefebvre-Brion and Robert W. Field
Academic Press, Inc., Orlando (1986)

[55] The HF and DF B $^1\Sigma^+$–X $^1\Sigma^+$ and C $^1\Pi$–X $^1\Sigma^+$ band systems studied by 1 XUV + 1 UV resonance enhanced multiphoton ionization
L. M. Tashiro, W. Ubachs and R. N. Zare
Journal of Molecular Spectroscopy **138** (1) 89–101 (1989)

[56] Narrow-band tunable extreme-ultraviolet laser source for lifetime measurements and precision spectroscopy
W. Ubachs, K. S. E. Eikema, W. Hogervorst and P. C. Cacciani
Journal of the Optical Society of America B **14** (10) 2469–2476 (1997)

[57] Observation of molecular hyperfine structure in the extreme ultraviolet: The HF C–X spectrum
J. N. Philippson, R. C. Shiell, E. Reinhold and W. Ubachs
Journal of Chemical Physics **129** (17) 174310 [6 pages] (2008)

[58] Quantum Mechanics
Albert Messiah
Dover Publications, Inc., New York (1999)

[59] Elementary Atomic Structure
Gordon K. Woodgate
Oxford University Press, Oxford (1999)

[60] Classical Electrodynamics, 3$^{\text{rd}}$ Edition
John D. Jackson
John Wiley & Sons, Inc., New York (1999)

[61] Magnetic Hyperfine Structure in Diatomic Molecules
R. A. Frosch and H. M. Foley
Physical Review **88** (6) 1337-1349 (1952)

[62] Magnetic Hyperfine Effects and Electronic Structure of NO
G. C. Dousmanis
Physical Review **97** (4) 967-970 (1955)

[63] Many-body calculations of hyperfine constants in diatomic molecules. II. First-row hydrides
P. Kristiansen and L. Veseth
Journal of Chemical Physics **84** (11) 6336–6344 (1986)

[64] Experimental and theoretical studies of the valence-shell dipole excitation spectrum and absolute photoabsorption cross section of hydrogen fluoride
A. P. Hitchcock, G. R. J. Williams, C. E. Brion and P. W. Langhoff
Chemical Physics **88** (1) 65–80 (1984)

[65] The E, F $^1\Sigma_g^+$ double-minimum state of hydrogen: two-photon excitation of inner and outer wells
E. E. Marinero, R. Vasudev, and R. N. Zare
Journal of Chemical Physics **78** (2) 692–699 (1983)

[66] A critical comparison of theoretical and experimental electronic spectrum and potential energy curves of HF molecule and its positive and negative ions
R. K. Chaudhuri, K. F. Freed, S. A. Abrash and D. M. Potts
Journal of Molecular Structure (Theochem) **547** (1) 83–96 (2001)

[67] The low-lying states of hydrogen fluoride: Potential energy curves for the X $^1\Sigma^+$, $^3\Sigma^+$, $^3\Pi$, and $^1\Pi$ states
T. H. Dunning
Journal of Chemical Physics **65** (10) 3854–3862 (1976)

[68] The Electronic Spectrum of HF. I. The B $^1\Sigma^+$-X $^1\Sigma^+$ Band System
G. Di Lonardo and A. E. Douglas
Canadian Journal of Physics **51** (4) 434–445 (1973)

[69] Ab-initio CI calculation of the effects of Rydberg-valence mixing in the electronic spectrum of the HF molecule
M. Bettendorff, R. J. Buenker, S. D. Peyerimhoff and J. Römelt
Zeitschrift für Physik A: Hadrons and Nuclei **304** (2) 125–135 (1982)

[70] Stark Effect and Hyperfine Structure of Hydrogen Fluoride
R. Weiss
Physical Review **131** (2) 659–665 (1963)

[71] The labeling of parity doublet levels in linear molecules
J. M. Brown, J. T. Hougen, K. -P. Huber, J. W. C. Johns, I. Kopp, H. Lefebvre-Brion, A. J. Merer, D. A. Ramsay, J. Rostas and R. N. Zare
Journal of Molecular Spectroscopy **55** (1) 500–503 (1975)

[72] Rotational Energy Levels and Rotational Line Intensities in Diatomic Molecules
J.T. Hougen
National Institute of Standards and Technology, Gaithersburg, MD (2001)
`http://physics.nist.gov/DiatomicCalculations`
Retrieved 2011/09/13

[73] Spectra of Atoms and Molecules, 2nd Edition
Peter F. Bernath
Oxford University Press, Oxford (2005)

[74] The electronic spectra of HCl and HF
A. E. Douglas and F. R. Greening
Canadian Journal of Physics **57** (10) 1650–1661 (1979)

[75] CRC, *Handbook of Chemistry and Physics*, 91st Ed.
Editor: D. Lide
CRC Press, Cleveland (2010)

[76] Sub-Doppler direct infrared laser absorption spectroscopy in fast ion beams: The fluorine hyperfine structure of HF^+
J. V. Coe, J. C. Owrutsky, E. R. Keim, N. V. Agman, D. C. Hovde and R. J. Saykally
Journal of Chemical Physics **90** (8) 3893–3902 (1989)

[77] Part of the far-infrared laser magnetic resonance spectrum of the HF^+ free radical
M. D. Allen, K. M. Evenson and J. M. Brown
Journal of Molecular Spectroscopy **227** (1) 13–22 (2004)

[78] The X $^2\Pi$ and A $^2\Sigma^+$ states of FH^+, ClH^+ and BrH^+: theoretical study of their g-factors and fine/hyperfine structures
P. J. Bruna and F. Grein
Molecular Physics **104** (3) 429–446 (2006)

[79] Atomic Hyperfine Structure. IV Positive and Negative First-Row Ions
H. F. Schaefer, III and R. A. Klemm
Physical Review A **1** (4) 1063-1069 (1970)

[80] $^{19}F^+$ atom in its ground ^3P state: The $J = 0 \leftarrow 1$ fine-structure interval
J. M. Brown, L. R. Zink and K. M. Evenson
Physical Review A **57** (4) 2507-2510 (1998)

Ionic–Covalent Coupling in Alkali–Alkali Collisions

[81] Dissociation Energy and Long-Range Potential of Diatomic Molecules from Vibrational Spacings of Higher Levels
R. J. LeRoy and R. B. Bernstein
Journal of Chemical Physics **52** (8) 3869–3879 (1970)

[82] The noncrossing rule and spurious avoided crossings
G. J. Hatton
Physical Review A **14** (3) 901-910 (1976)

[83] Experimental and theoretical study of the ion-ion mutual neutralization reactions $Ar^+ + SF_n^-$ ($n = 6$, 5, and 4)
J.C. Bopp, T.M. Miller, A.A. Viggiano and J. Troe
Journal of Chemical Physics **129** (7) 074308 [9 pages] (2008)

[84] Collisional quenching of $CO^+(A\,^2\Pi_{3/2}, v = 1)$ by Ne
J. Lemaire, R. Marx, D. C. Parent and M. Chevrier
Journal of Chemical Physics **92** (3) 1653–1656 (1990)

[85] Chemi-ionization in alkali–heteronuclear halogen collisions: Role of excited molecular ion states
D.J. Auerbach, M.M. Hubers, A.P.M. Baede and J. Los
Chemical Physics **2** (1) 107–118 (1973)

[86] Charge-transfer induced particle emission in gas surface reactions
T. Greber
Surface Science Reports **28** (1) 1–64 (1997)

[87] IUPAC Gold Book – Atomic Units
`http://goldbook.iupac.org/A00504.html`
Retrieved 2011/12/02

[88] Non-Adiabatic Crossing of Energy Levels
C. Zener
Proceedings of the Royal Society of London. Series A **137** (833) 696–702 (1932)

[89] Double Stern-Gerlach Experiment and Related Collision Phenomena
N. Rosen and C. Zener
Physical Review **40** (4) 502–507 (1932)

[90] NONADIABATIC TRANSITIONS: What We Learned from Old Masters and How Much We Owe Them
E.E. Nikitin
Annual Reviews of Physical Chemistry **50** 1–21 (1999)

[91] Long-range configuration interaction of ionic and covalent states
R. Grice and D. R. Herschbach
Molecular Physics **27** (1) 159–175 (1974)

[92] The Theory of Atomic Structure and Spectra
Robert D. Cowan
University of California Press, Berkeley (1981)

[93] Alkali Atom Reactive Scattering and the Electron-Jump Model
Roger Grice
Ph.D. Thesis, Harvard University (1968)

[94] Analytical Hartree–Fock Wave Functions Subject to Cusp and Asymptotic Constraints: He to Xe, Li^+ to Cs^+, H^- to I^-
T. Koga, K. Kanayama, S. Watanabe and A. J. Thakkar
International Journal of Quantum Chemistry **71** (6) 491–497 (1999)

[95] A. Thakkar downloads webpage
`http://www.unb.ca/fredericton/science/chem/ajit/f_download.htm`
Retrieved 2011/11/15

[96] New Developments in Molecular Orbital Theory
C. C. J. Roothaan
Reviews of Modern Physics **23** (2) 69–89 (1951)

[97] The Calculation of the absolute strengths of spectral lines
D. R. Bates and A. Damgaard
Philosophical Transactions of the Royal Society of London A **242** (842) 101–122 (1949)

[98] The Wave Mechanics of an Atom with a Non-Coulomb Central Field. Part I. Theory and Methods
D. R. Hartree
Mathematical Proceedings of the Cambridge Philosophical Society **24** (1) 89–110 (1928)

[99] NIST Atomic Spectra Database v4, NIST Standard Reference Database #78
`http://www.nist.gov/pml/data/asd.cfm`
Retrieved 2011/10/19

[100] Molecular Spectra and Molecular Structure: Volume 1 - Spectra of Diatomic Molecules
Gerhard Herzberg
Krieger Publishing Company, Malabar FL (1989)

[101] Estimation of the Coupling Matrix Elements for One-Electron Transfer Systems
R. E. Olson, F. T. Smith and E. Bauer
Applied Optics **10** (8) 1848–1855 (1971)

[102] Collisional ion-pair formation in an excited alkali-metal vapor
L. Barbier, M. T. Djerad, and M. Chéret
Physical Review A **34** (4) 2710-2718 (1986)

The magneto-optical trap – Theory

[103] Laser cooling and trapping of neutral atoms
W. D. Phillips
Reviews of Modern Physics **70** (3) 721-741 (1998)

[104] The semiclassical theory of laser cooling
S. Stenholm
Reviews of Modern Physics **58** (3) 699-739 (1986)

[105] Power broadening revisited: theory and experiment
N. V. Vitanov, B. W. Shore, L. Yatsenko, K. Böhmer, T. Halfmann, T. Rickes and K. Bergmann
Optics Communications **199** (1) 117-126 (2001)

[106] Optical molasses
P. D. Lett, W. D. Phillips, S. L. Rolston, C. E. Tanner, R. N. Watts and C. I. Westbrook
Journal of the Optical Society of America B **6** (11) 2084-2107 (1986)

[107] Decay Rate Measurement of Lithium in a MagnetoOptical Trap
J. Kawanaka, K. Shimizu and H. Takuma
Applied Physics B **57** (2) 113-118 (1993)

[108] Radiative lifetimes of excited Li I states
W. Hansen
Journal of Physics B: Atomic and Molecular Physics **16** (6) 933-936 (1983)

[109] Reference Data on Atoms, Molecules, and Ions
Aleksandr A. Radzig and Boris M. Smirnov
Springer–Verlag, Berlin (1985)

[110] Laser-cooled and trapped atoms as a precision target for heavy ion beams
U. Schünemann, I. Manek, R. Grimm, D. Habs and D. Schwalm
Hyperfine Interactions **99** (1) 127–133 (1996)

The magneto-optical trap – Experiment

[111] Opnext HL6714G datasheet
`http://www.opnext.com/products/pdf/ode2_043_hl6714g.pdf`
Retrieved 2011/11/27

[112] Linewidths below 100 kHz with external cavity diode lasers
S. D. Saliba and R. E. Scholten
Applied Optics **48** (36) 6961–6966 (2009)

[113] Richardson Gratings homepage
`http://www.gratinglab.com/home.asp`
Retrieved 2011/11/27

[114] Littrow configuration tunable external cavity diode laser with fixed direction output beam
C. J. Hawthorn, K. P. Weber and R. E. Scholten
Review of Scientific Instruments **72** (12) 4477–4479 (2001)

[115] Measurement of diode laser characteristics affecting tunability with an external grating
G. -Y. Yan and A. L. Schawlow
Journal of the Optical Society of America B **9** (11) 2122–2127 (1992)

[116] Microcontroller-based wavemeter using compression locking of an internal mirror reference laser
M. Ugray, J. E. Atfield, T. G. McCarthy and R. C. Shiell
Review of Scientific Instruments **77** (11) 113109 [5 pages] (2006)

[117] Laser wavemeter with solid Fizeau wedge interferometer
C. Reiser and R. B. Lopert
Applied Optics **27** (17) 3656–3660 (1988)

[118] Frequency-Stabilized Diode Laser with the Zeeman Shift in an Atomic Vapor
K. L. Corwin, Z. -T. Lu, C. F. Hand, R. J. Epstein and C. E. Wieman
Applied Optics **37** (15) 3295–3298 (1998)

[119] A visible extended cavity diode laser for the undergraduate laboratory
R. S. Conroy, A. Carleton, A. Carruthers, B. D. Sinclair, C. F. Rae and K. Dholakia
American Journal of Physics **68** (10) 925–931 (2000)

[120] Laser Spectroscopy
W. Demtroder
Springer-Verlag, New York, 1981

[121] Feedback for physicists: A tutorial essay on control
J. Bechhoefer
Reviews of Modern Physics **77** (3) 783-836 (2005)

[122] Simple scheme for tunable frequency offset locking of two lasers
U. Schünemann, H. Engler, R. Grimm, M. Weidemüller, M. Zielonkowski
Review of Scientific Instruments **70** (1) 242–243 (1999)

[123] Laser frequency offset locking using a side of filter technique
G. Ritt, G. Cennini, C. Geckeler and M. Weitz
Applied Physics B: Lasers and Optics **79** (3) 363–365 (2004)

[124] Injection locking of microwave solid-state oscillators
K. Kurokawa
Proceedings of the IEEE **61** (10) 1386–1410 (1973)

[125] Frequency and intensity noise in injection-locked semiconductor lasers: Theory and experiments
P. Spano, S. Piazzolla and M. Tamburrini
IEEE Journal of Quantum Electronics **22** (3) 427–435 (1986)

[126] Narrow-Linewidth Master-Oscillator Power Amplifier Based on a Semiconductor Tapered Amplifier
A. C. Wilson, J. C. Sharpe, C. R. McKenzie, P. J. Manson and D. M. Warrington
Applied Optics **37** (21) 4871–4875 (1998)

[127] High-power multiple-frequency narrow-linewidth laser source based on a semiconductor tapered amplifier
G. Ferrari, M. -O. Mewes, F. Schreck and C. Salomon
Optics Letters **24** (3) 151–153 (1999)

[128] Compact angle-resolved optical spectrum analyzer using a programmable microcontroller approach
J. N. Philippson, M. Ugray, T. J. Toai and R. C. Shiell
Journal of Optics A: Pure and Applied Optics **9** (11) 1024–1029 (2007)

[129] Microcontroller-based imaging system utilizing a CMOS image sensor array
R. C. Shiell, **J. N. Philippson** and M. D. R. Ugray
United States Patent 7,990,544 (August 2, 2011)

[130] The Optics of Semiconductor Diode Lasers
M. Mansuripur and E. M. Wright
Optics & Photonics News **13** (7) 57–61 (2002)

[131] Design and characteristics of a tapered amplifier diode system by seeding with continuous-wave and mode-locked external cavity diode laser
Y. Xiong, S. Murphy and J. L. Carlsten
Optical Engineering **45** (12) 124205 [5 pages] (2006)

Polarization Measurement and Control

[132] Information and resolution in electromagnetic optical systems
M. R. Foreman and P. Török
Physical Review A **82** (4) 043835 [9 pages] (2010)

[133] Polarization imaging for industrial inspection
F. Meriaudeau, M. Ferraton, C. Stolz, O.Morel and L. Bigue
Image Processing: Machine Vision Applications, K. S. Niel and D. Fofi, ed.
Proceedings of the SPIE **6813** 681308 [10 pages] (2008)

[134] Observations of solar scattering polarization at high spatial resolution
F. Snik, A. G. de Wijn, K. Ichimoto, C. E. Fischer, C. U. Keller and B. W. Lites
Astronomy and Astrophysics **519** A18 [9 pages] (2010)

[135] Mueller matrix dual-rotating retarder polarimeter
D. H. Goldstein
Applied Optics **31** (31) 6676–6683 (1992)

[136] High-speed transmission limitations due to Polarization Mode Dispersion
R. Randhawa and R. S. Kaler
Optik **121** (16) 1450–1454 (2010)

[137] Optimizing precision of rotating compensator ellipsometry
L. Broch and L. Johann
Physica Status Solidi (C) **5** (5) 1036-1040 (2008)

[138] Review of passive imaging polarimetry for remote sensing applications
J. S. Tyo, D. L. Goldstein, D. B. Chenault and J. A. Shaw
Applied Optics **45** (22) 5453–5469 (2006)

[139] Composition and resolution of streams of polarized light from multiple sources
G. G. Stokes
Transactions of the Cambridge Philosophical Society **9** 399-416 (1852)
Reprinted in *Mathematical and Physical Papers*, Vol. 3, Cambridge University (1901)

[140] Memorandum on the polarization optics of the photoelastic shutter
H. Mueller
Report No. 2 of the OSRD project OEMsr-576, (1943)

[141] Optics
Eugene Hecht
Addison–Wesley, Boston (2002)

[142] Achromatic retarders using quartz and mica
P. Hariharan
Measurement Science and Technology **6** (7) 1078–1079 (1995)

[143] Experimental research of temperature influence on retardance in crystal quartz for deep ultraviolet range of wavelength
E. Rabinovich and J. Lewis
Optical Engineering **46** (2) 026501 [5 pages] (2007)

[144] Stress Birefringence in Polyethylene
S. M. Crawford and H. Kolsky
Proceedings of the Physical Society B **64** (2) 119–125 (1951)

[145] Optical Properties of Solids
Mark Fox
Oxford University Press, Oxford (2010)

[146] Polarization measurements of HeI singlet transitions following beam–tilted-foil excitation
R. L. Brooks and E. H. Pinnington
Physical Review A **18** (4) 1454–1458 (1978)

[147] Polarization studies using beam foil spectroscopy
R. L. Brooks
Ph.D. thesis, University of Alberta (1979)

[148] Calibration method using a single retarder to simultaneously measure polarization and fully characterize a polarimeter over a broad range of wavelengths
M. J. Romerein, **J. N. Philippson**, R. L. Brooks and R. C. Shiell
Applied Optics **50** (28) 5382–5389 (2011)

[149] Analysis of a method for measuring polarization characteristics with a Stokes polarimeter having a rotating phase plate
V. A. Dlugunovich, V. N. Snopko and O. V. Tsaryuk
Journal of Optical Technology **68** (4) 269–273 (2001)

[150] Principles of Optics
Max Born and Emil Wolf
Cambridge University Press, Cambridge (1999)

[151] PIC Microcontrollers
Milan Verle
Mikro-Elektronika, Belgrade (2008)

[152] Handbook of optics
Michael Bass
McGraw Hill Professional, Columbus (1994)

[153] Birefringence of muscovite mica
M. S. El-Bahrawi, N. N. Nagib, S. A. Khodier and H. M. Sidki
Optics & Laser Technology **30** (6–7) 411–415 (1998)

Deriving matrix elements for HF

[154] Angular momentum
Richard N. Zare
John Wiley & Sons, Inc., New York (1988)

[155] Electron Resonance of Gaseous Diatomic Molecules
Alan Carrington, Donald H. Levy and Terry A. Miller
Defense Technical Information Center (1968)

[156] Theoretical Aspects of High–Resolution Molecular Spectra
E. Hirota
??? (1985)

[157] High–Resolution Spectroscopy on the $C\,^1\Pi \leftrightarrow A\,^1\Delta$ Transition in NH
W. Ubachs, G. Meyer, J.J. ter Meulen and A. Dymanus
Journal of Molecular Spectroscopy **115** (1) 88–104 (1986)

Appendix A

Deriving Matrix Elements for HF

The following derivations make use of the notation of *irreducible spherical tensors*, denoted $T^k(\hat{\mathbf{X}})$ for a rank-k tensor operator, $\hat{\mathbf{X}}$, and $T^k_p(\hat{\mathbf{X}})$ for the p^{th} of its $2k+1$ components. Irreducible spherical tensors, often just referred to as spherical tensors, transform in a similar manner to spherical harmonics under rotations and often simplify problems by making use of molecular symmetries [53].

The Wigner–Eckart theorem and the processes for decoupling the various angular momenta to successively simplify the matrix elements make use of Racah algebra. Details of equations used along with expressions for the various 3-j and 6-j symbols and properties of the Wigner rotation matrices can be found in reference [154].

A.1 The hyperfine Hamiltonian

The effective hyperfine Hamiltonian for HF is composed of two terms, corresponding to the coupling of each of the nuclear spins to the electronic orbital angular momentum, and is given by,

$$\hat{H}_{\rm hfs} = \hat{a}_{\rm F} T^1(\hat{\mathbf{I}}_{\rm F}) \cdot T^1(\hat{\mathbf{L}}) + \hat{a}_{\rm H} T^1(\hat{\mathbf{I}}_{\rm H}) \cdot T^1(\hat{\mathbf{L}}), \tag{A.1}$$

where the operators $\hat{a}_{\rm F}$ and $\hat{a}_{\rm H}$ are radial functions which, for diagonal matrix elements, become the magnetic dipole hyperfine coupling constants for fluorine and hydrogen respectively. The matrix elements of the fluorine and hydrogen terms of $\hat{H}_{\rm hfs}$ are labelled $ME_{\rm F}$ and $ME_{\rm H}$ respectively.

A.1.1 Deriving $ME_{\rm F}$

The derivation of $ME_{\rm F}$ starts with the application of the Wigner–Eckart theorem, factoring out any dependence on M_F, which depends on the orientation of the total angular momentum,

$$\begin{aligned} ME_{\rm F} &= \langle \gamma' \, \Lambda' \, S \, \Sigma \, J' \, I_{\rm F} \, F_1' \, I_{\rm H} \, F' \, M_F' | \hat{a}_{\rm F} T^1(\hat{\mathbf{I}}_{\rm F}) \cdot T^1(\hat{\mathbf{L}}) | \gamma \, \Lambda \, S \, \Sigma \, J \, I_{\rm F} \, F_1 \, I_{\rm H} \, F \, M_F \rangle \\ &= (-1)^{F'-M_F'} \begin{pmatrix} F' & 0 & F \\ -M_F' & 0 & M_F \end{pmatrix} \\ &\times \langle \gamma' \, \Lambda' \, S \, \Sigma \, J' \, I_{\rm F} \, F_1' \, I_{\rm H} \, F' \| \hat{a}_{\rm F} T^1(\hat{\mathbf{I}}_{\rm F}) \cdot T^1(\hat{\mathbf{L}}) \| \gamma \, \Lambda \, S \, \Sigma \, J \, I_{\rm F} \, F_1 \, I_{\rm H} \, F \rangle. \end{aligned} \tag{A.2}$$

For a non-zero 3-j symbol the projections must sum to zero, so $M_F' = M_F$, and the triangle condition requires that $F' = F$. Using the equations of Racah algebra to

decouple the 'outermost' angular momentum, a simplified form of the reduced matrix element is obtained[1],

$$\begin{aligned} ME_{\mathrm{F}} = {} & \delta_{M_F M_F'} \delta_{FF'} (-1)^{F-M_F} \begin{pmatrix} F & 0 & F \\ -M_F & 0 & M_F \end{pmatrix} \\ & \times (-1)^{F_1'+I_{\mathrm{H}}+F} (2F+1) \begin{Bmatrix} F_1' & F & I_{\mathrm{H}} \\ F & F_1 & 0 \end{Bmatrix} \\ & \times \langle \gamma' \, \Lambda' \, S \, \Sigma \, J' \, I_{\mathrm{F}} \, F_1' \| \hat{a}_{\mathrm{F}} T^1(\hat{\mathbf{I}}_{\mathrm{F}}) \cdot T^1(\hat{\mathbf{L}}) \| \gamma \, \Lambda \, S \, \Sigma \, J \, I_{\mathrm{F}} \, F_1 \rangle \end{aligned} \tag{A.3}$$

The triangle conditions for a non-zero 6-j symbol require that $F_1' = F_1$. For this case both the 3-j and 6-j symbols take simple algebraic forms,

$$\begin{Bmatrix} F_1 & F & I_{\mathrm{H}} \\ F & F_1 & 0 \end{Bmatrix} = (-1)^{F_1+F+I_{\mathrm{H}}} \left[(2F_1+1)(2F+1) \right]^{-\frac{1}{2}} \tag{A.4}$$

and

$$\begin{pmatrix} F & 0 & F \\ -M_F & 0 & M_F \end{pmatrix} = (-1)^{F-M_F} (2F+1)^{-\frac{1}{2}}. \tag{A.5}$$

Substituting in these results in addition to cancelling $(-1)^{4F+2F_1+2I_{\mathrm{H}}-2M_F} = 1$ gives,

$$\begin{aligned} ME_{\mathrm{F}} = {} & \delta_{M_F M_F'} \delta_{FF'} \delta_{F_1 F_1'} (2F_1+1)^{-\frac{1}{2}} \\ & \times \langle \gamma' \, \Lambda' \, S \, \Sigma \, J' \, I_{\mathrm{F}} \, F_1' \| \hat{a}_{\mathrm{F}} T^1(\hat{\mathbf{I}}_{\mathrm{F}}) \cdot T^1(\hat{\mathbf{L}}) \| \gamma \, \Lambda \, S \, \Sigma \, J \, I_{\mathrm{F}} \, F_1 \rangle. \end{aligned} \tag{A.6}$$

Using the algebric form for a reduced matrix element of a scalar product of two operators that act on different parts of the system in terms of the product of the

[1] See ref. [154], p.195.

reduced matrix elements for each individual operator results in,

$$ME_{\mathrm{F}} = \delta_{M_F M_F'}\delta_{FF'}\delta_{F_1 F_1'}(-1)^{J+I_{\mathrm{F}}+F_1}\begin{Bmatrix} J' & I_{\mathrm{F}} & F_1 \\ I_{\mathrm{F}} & J & 1 \end{Bmatrix} \times \langle \gamma\,\Lambda\,S\,\Sigma\,I_{\mathrm{F}}||T^1(\hat{\mathbf{I}}_{\mathrm{F}})||\gamma\,\Lambda\,S\,\Sigma\,I_{\mathrm{F}}\rangle\langle\gamma'\,\Lambda'\,S\,\Sigma\,J'\|\hat{a}_{\mathrm{F}}T^1(\hat{\mathbf{L}})\|\gamma\,\Lambda\,S\,\Sigma\,J\rangle. \quad \text{(A.7)}$$

Note that although these are vector operators the reduced matrix element is, by definition, independent of orientation, and hence a scalar. The first reduced matrix element takes a simple form,

$$\langle \gamma\,\Lambda\,S\,\Sigma\,I_{\mathrm{F}}||T^1(\hat{\mathbf{I}}_{\mathrm{F}})||\gamma\,\Lambda\,S\,\Sigma\,I_{\mathrm{F}}\rangle = \sqrt{(2I_{\mathrm{F}}+1)(I_{\mathrm{F}}+1)I_{\mathrm{F}}}. \quad \text{(A.8)}$$

For Hund's case (a) molecules L is not a good quantum number so the projection onto the internuclear axis, Λ, is used, which is a good quantum number in the molecule-fixed frame. The Wigner rotation matrix, $\mathcal{D}^{(1)}$, is used in the transformation into the molecule-fixed frame,

$$T^1_p(\hat{\mathbf{L}}) = \sum_q \mathcal{D}^{(1)}_{pq}(\omega)^* T^1_q(\hat{\mathbf{L}}), \quad \text{(A.9)}$$

where p is an index for the space-fixed coordinates, q represents the molecule-fixed coordinates, and $\omega = (\phi, \theta, \chi)$ represents the Euler angles.

We now have,

$$ME_{\rm F} = \delta_{M_F M'_F}\delta_{FF'}\delta_{F_1F'_1}(-1)^{J+I_F+F_1}\left\{\begin{array}{ccc} J' & I_{\rm F} & F_1 \\ I_{\rm F} & J & 1 \end{array}\right\}\sqrt{(2I_{\rm F}+1)(I_{\rm F}+1)I_{\rm F}}$$
$$\times \langle \gamma'\,\Lambda'\,S\,\Sigma\,J'||\hat{a}_{\rm F}\sum_q \mathcal{D}^1_{\cdot q}(\omega)^* L^1_q||\gamma\,\Lambda\,S\,\Sigma\,J\rangle, \tag{A.10}$$

where that dot signifies the fact that the matrix element is reduced with respect to the space fixed coordinates (it is a factor common to all components in the space-fixed frame).

The electron spin component (assumed to be normalized) is factored out and the rotation matrix and angular momentum operator are separated in each term of the summation,

$$ME_{\rm F} = \delta_{M_F M'_F}\delta_{FF'}\delta_{F_1F'_1}(-1)^{F_1+I_{\rm F}+J}\sqrt{(2I_{\rm F}+1)(I_{\rm F}+1)I_{\rm F}}\left\{\begin{array}{ccc} J' & I_{\rm F} & F_1 \\ I_{\rm F} & J & 1 \end{array}\right\}$$
$$\times \langle S\,\Sigma|S\,\Sigma\rangle\sum_q \langle \gamma'\,\Lambda'\,J'||\mathcal{D}^1_{\cdot q}(\omega)^*||\gamma\,\Lambda\,J\rangle\langle\gamma'\,\Lambda'|\hat{a}_{\rm F}T^1_q(\hat{\mathbf{L}})|\gamma\,\Lambda\rangle. \tag{A.11}$$

The eigenfunctions of the symmetric top rotational Hamiltonian are proportional to the complex conjugate of the rotation matrix element $\mathcal{D}^{(k)}_{pq}(\omega)$ giving a functional form[2],

$$\psi_{J\Omega M} = \sqrt{\frac{2J+1}{8\pi^2}}\mathcal{D}^{(J)}_{M\Omega}(\omega)^*. \tag{A.12}$$

[2]See ref. [53], p.167.

Thus we can derive the relations,

$$\langle J'\,\Omega'\,M'|\mathcal{D}^{(k)}_{pq}(\omega)^*|J\,\Omega\,M\rangle$$

$$= \frac{\sqrt{(2J+1)(2J'+1)}}{8\pi^2}\int \mathcal{D}^{(J')}_{M'\Omega'}(\omega)^*\mathcal{D}^{(k)}_{pq}(\omega)^*\mathcal{D}^{(J)}_{M\Omega}(\omega)^* d\omega \tag{A.13}$$

$$= (-1)^{M-\Omega}\sqrt{(2J+1)(2J'+1)}\begin{pmatrix} J' & k & J \\ -\Omega' & q & \Omega \end{pmatrix}\begin{pmatrix} J' & k & J \\ -M' & p & M \end{pmatrix}, \tag{A.14}$$

making use of the identity,

$$\int \mathcal{D}^{(j_1)}_{m'_1 m_1}(\omega)\mathcal{D}^{(j_2)}_{m'_2 m_2}(\omega)\mathcal{D}^{(j_3)}_{m'_3 m_3}(\omega)d\omega = 8\pi^2\begin{pmatrix} j_1 & j_2 & j_3 \\ m'_1 & m'_2 & m'_3 \end{pmatrix}\begin{pmatrix} j_1 & j_2 & j_3 \\ m_1 & m_2 & m_3 \end{pmatrix}, \tag{A.15}$$

along with the relationship,

$$\mathcal{D}^{(k)}_{pq}(\omega)^* = (-1)^{p-q}\mathcal{D}^{(k)}_{-p,-q}. \tag{A.16}$$

Applying the Wigner–Eckart theorem and recognizing that in the case of no spin $\Omega = \Lambda$ gives,

$$\langle \gamma'\,\Lambda'\,J'||\mathcal{D}^1_{\cdot q}(\omega)^*||\gamma\,\Lambda\,J\rangle = (-1)^{J'-\Lambda'}\sqrt{(2J'+1)(2J+1)}\begin{pmatrix} J' & 1 & J \\ -\Lambda' & q & \Lambda \end{pmatrix}, \tag{A.17}$$

assuming that γ and γ' do not feature in the matrix of $\mathcal{D}^{(1)}_{pq}(\omega)^*$, in accordance with Brown and Carrington[3].

[3]See ref. [53], p.518.

Substituting this last result into equation A.11 we have the final result for ME_{F},

$$\begin{aligned} ME_{\mathrm{F}} &= \delta_{M_F M_F'} \delta_{FF'} \delta_{F_1 F_1'} (-1)^{F_1+I_{\mathrm{F}}+J+J'-\Lambda'} \\ &\times \sqrt{(2J'+1)(2J+1)(2I_{\mathrm{F}}+1)(I_{\mathrm{F}}+1)I_{\mathrm{F}}} \begin{Bmatrix} J' & I_{\mathrm{F}} & F_1 \\ I_{\mathrm{F}} & J & 1 \end{Bmatrix} \\ &\times \sum_q \begin{pmatrix} J' & 1 & J \\ -\Lambda' & q & \Lambda \end{pmatrix} \langle \gamma' \Lambda' | \hat{a}_{\mathrm{F}} T^1_q(\hat{\mathbf{L}}) | \gamma \Lambda \rangle. \end{aligned} \tag{A.18}$$

Often we are only interested in a given electronic state, hence $\Lambda = \Lambda' \Rightarrow q = 0$, $\gamma = \gamma'$, and a_{F} is the fluorine magnetic hyperfine coupling constant,

$$\begin{aligned} ME_{\mathrm{F}} &= \delta_{M_F M_F'} \delta_{FF'} \delta_{F_1 F_1'} a_{\mathrm{F}} \Lambda (-1)^{F_1+I_{\mathrm{F}}+J+J'-\Lambda} \\ &\times \sqrt{(2J'+1)(2J+1)(2I_{\mathrm{F}}+1)(I_{\mathrm{F}}+1)I_{\mathrm{F}}} \\ &\times \begin{Bmatrix} J' & I_{\mathrm{F}} & F_1 \\ I_{\mathrm{F}} & J & 1 \end{Bmatrix} \begin{pmatrix} J' & 1 & J \\ -\Lambda & 0 & \Lambda \end{pmatrix}. \end{aligned} \tag{A.19}$$

A.1.2 Deriving ME_{H}

The matrix elements of $\hat{a}_{\mathrm{H}} T^1(\hat{\mathbf{I}}_{\mathrm{H}}) \cdot T^1(\hat{\mathbf{L}})$, ME_{H}, are given by

$$ME_{\mathrm{H}} = \langle \gamma' \, \Lambda' \, S \, \Sigma \, J' \, I_{\mathrm{F}} \, F_1' \, I_{\mathrm{H}} \, F' \, M_F' | \hat{a}_{\mathrm{H}} T^1(\hat{\mathbf{I}}_{\mathrm{H}}) \cdot T^1(\hat{\mathbf{L}}) | \gamma \, \Lambda \, S \, \Sigma \, J \, I_{\mathrm{F}} \, F_1 \, I_{\mathrm{H}} \, F \, M_F \rangle. \quad \text{(A.20)}$$

Splitting up the product gives,

$$\begin{aligned} ME_{\mathrm{H}} = {} & \delta_{M_F M_F'} \delta_{FF'} (-1)^{F_1 + I_{\mathrm{H}} + F'} \left\{ \begin{array}{ccc} F_1' & I_{\mathrm{H}} & F' \\ I_{\mathrm{H}} & F_1 & 1 \end{array} \right\} \\ & \times \langle \gamma' \, \Lambda' \, S \, \Sigma \, J' \, I_{\mathrm{F}} \, I_{\mathrm{H}} || T^1(\hat{\mathbf{I}}_{\mathrm{H}}) || \gamma' \, \Lambda' \, S \, \Sigma \, J' \, I_{\mathrm{F}} \, I_{\mathrm{H}} \rangle \\ & \times \langle \gamma' \, \Lambda' \, S \, \Sigma \, J' \, I_{\mathrm{F}} \, F_1' || \hat{a}_{\mathrm{H}} T^1(\hat{\mathbf{L}}) || \gamma \, \Lambda \, S \, \Sigma \, J \, I_{\mathrm{F}} \, F_1 \rangle. \end{aligned} \quad \text{(A.21)}$$

The reduced matrix element of $T^1(\hat{\mathbf{I}}_{\mathrm{H}})$ has a simple functional form,

$$\begin{aligned} ME_{\mathrm{H}} = {} & \delta_{M_F M_F'} \delta_{FF'} (-1)^{F_1 + I_{\mathrm{H}} + F} \left\{ \begin{array}{ccc} F_1' & I_{\mathrm{H}} & F \\ I_{\mathrm{H}} & F_1 & 1 \end{array} \right\} \sqrt{(2I_{\mathrm{H}} + 1)(I_{\mathrm{H}} + 1) I_{\mathrm{H}}} \\ & \times \langle \gamma' \, \Lambda' \, S \, \Sigma \, J' \, I_{\mathrm{F}} \, F_1' || \hat{a}_{\mathrm{H}} T^1(\hat{\mathbf{L}}) || \gamma \, \Lambda \, S \, \Sigma \, J \, I_{\mathrm{F}} \, F_1 \rangle. \end{aligned} \quad \text{(A.22)}$$

The remaining reduced matrix element can by simplified by decoupling I_{F},

$$\begin{aligned} ME_{\mathrm{H}} = {} & \delta_{M_F M_F'} \delta_{FF'} (-1)^{F_1 + I_{\mathrm{H}} + F + J' + I_{\mathrm{F}} + F_1 + 1} \left\{ \begin{array}{ccc} F_1' & I_{\mathrm{H}} & F \\ I_{\mathrm{H}} & F_1 & 1 \end{array} \right\} \left\{ \begin{array}{ccc} J' & F_1' & I_{\mathrm{F}} \\ F_1 & J & 1 \end{array} \right\} \\ & \times \sqrt{(2F_1' + 1)(2F_1 + 1)(2I_{\mathrm{H}} + 1)(I_{\mathrm{H}} + 1) I_{\mathrm{H}}} \\ & \times \langle \gamma' \, \Lambda' \, S \, \Sigma \, J' || \hat{a}_{\mathrm{H}} T^1(\hat{\mathbf{L}}) || \gamma \, \Lambda \, S \, \Sigma \, J \rangle. \end{aligned} \quad \text{(A.23)}$$

Following the same procedure as in the previous section, the operator $T^1(\hat{\mathbf{L}})$ is expressed in terms of its components in the molecule fixed frame, giving,

$$ME_{\rm H} = \delta_{M_F M'_F}\delta_{FF'}(-1)^{2F_1+I_{\rm H}+F+J'+I_{\rm F}+1}\left\{\begin{array}{ccc} F'_1 & I_{\rm H} & F \\ I_{\rm H} & F_1 & 1 \end{array}\right\}\left\{\begin{array}{ccc} J' & F'_1 & I_{\rm F} \\ F_1 & J & 1 \end{array}\right\}$$
$$\times\sqrt{(2F'_1+1)(2F_1+1)(2I_{\rm H}+1)(I_{\rm H}+1)I_{\rm H}}$$
$$\times\sum_q\langle\gamma'\,\Lambda'\,J'||\mathcal{D}^1_{\cdot q}(\omega)^*||\gamma\,\Lambda\,J\rangle\langle\gamma'\,\Lambda'|\hat{a}_{\rm H}T^1_q(\mathbf{L})|\gamma\,\Lambda\rangle. \qquad \text{(A.24)}$$

Making use of the identity given in equation A.17, the final result for $ME_{\rm H}$ is obtained,

$$ME_{\rm H} = \delta_{M_F M'_F}\delta_{FF'}(-1)^{F+2F_1+I_{\rm H}+2J'+I_{\rm F}+1-\Lambda'}\left\{\begin{array}{ccc} F'_1 & I_{\rm H} & F \\ I_{\rm H} & F_1 & 1 \end{array}\right\}\left\{\begin{array}{ccc} J' & F'_1 & I_{\rm F} \\ F_1 & J & 1 \end{array}\right\}$$
$$\times\sqrt{(2J'+1)(2J+1)(2F'_1+1)(2F_1+1)(2I_{\rm H}+1)(I_{\rm H}+1)I_{\rm H}}$$
$$\times\sum_q\left(\begin{array}{ccc} J' & 1 & J \\ -\Lambda' & q & \Lambda \end{array}\right)\langle\gamma'\,\Lambda'|\hat{a}_{\rm H}T^1_q(\mathbf{L})|\gamma\,\Lambda\rangle. \qquad \text{(A.25)}$$

For a given electronic state this gives the result,

$$ME_{\rm H} = \delta_{M_F M'_F}\delta_{FF'}\hat{a}_{\rm H}\Lambda(-1)^{F+2F_1+I_{\rm H}+2J'+I_{\rm F}+1-\Lambda}\left\{\begin{array}{ccc} F'_1 & I_{\rm H} & F \\ I_{\rm H} & F_1 & 1 \end{array}\right\}\left\{\begin{array}{ccc} J' & F'_1 & I_{\rm F} \\ F_1 & J & 1 \end{array}\right\}$$
$$\times\sqrt{(2J'+1)(2J+1)(2F'_1+1)(2F_1+1)(2I_{\rm H}+1)(I_{\rm H}+1)I_{\rm H}}$$
$$\times\left(\begin{array}{ccc} J' & 1 & J \\ -\Lambda & 0 & \Lambda \end{array}\right). \qquad \text{(A.26)}$$

A.1.3 Comparing matrix elements with the literature

The following is a comparison of the derivations given above with equivalent formulae given in the literature. For the diagonal case, $J = J'$, and singlet excited states, $S = 0$, all authors are in agreement with equations A.19 and A.26.

ME_{F}

Carrington, Levy and Miller[4] (CLM),

$$ME_{\mathrm{F}}^{\mathrm{CLM}} = (-1)^{J'+J} ME_{\mathrm{F}}. \tag{A.27}$$

Hirota[5] (H),

$$ME_{\mathrm{F}}^{\mathrm{H}} = (-1)^{J'-J} ME_{\mathrm{F}}. \tag{A.28}$$

Ubachs and Meyer[6] (UM). The (UM) result includes both parts of $\hat{H}_{\mathrm{hfs}}$, as well as an electric quadrupole term; the first term is related to equation A.19 by,

$$ME_{\mathrm{F}}^{\mathrm{UM}} = (-1)^{J'+J} ME_{\mathrm{F}}. \tag{A.29}$$

Brown and Carrington[7] (BC). The (BC) result is identical to equation A.19 for all cases,

$$ME_{\mathrm{F}}^{\mathrm{BC}} = ME_{\mathrm{F}}. \tag{A.30}$$

[4]See reference [155], equation 3.67, page 197.
[5]See reference [156], equation 2.3.66, page 36.
[6]See reference [157], equation 3, page 90.
[7]See reference [53], equation 8.372, page 518.

ME_{H}

Only two of the publications covered in section A.1.3 include results for a second nuclear spin.

Hirota (H). Comparison with the (H) result is non–trivial because no explicit expression is given for the matrix elements of $\hat{H}_{\mathrm{hfs}}$ with two nuclear spins. However, it is stated that, "the matrix elements for the second nucleus are obtained by multiplying the relevant matrix elements by the factor

$$(-1)^{J'+F_1+I_1+k}[(2F_1'+1)(2F_1+1)]^{\frac{1}{2}} \begin{Bmatrix} J' & F_1' & I_1 \\ F_1 & J & k \end{Bmatrix}, \tag{A.31}$$

where k = 1 and 2 for the magnetic and nuclear electric quadrupole hyperfine interactions, respectively."[8]

To apply the relevant equation to the second nucleus, the appropriate changes are[9],

$$\begin{aligned} I &\rightarrow I_{\mathrm{H}}, \\ J &\rightarrow F_1, \\ F &\rightarrow F, \end{aligned}$$

noting that these changes do not apply to the last line of equation 2.3.66, which is simply the identity for the reduced matrix elements of the rotation matrix given in equation A.17 above. Multiplying by the factor, A.31, produces an identical result to that given in equation A.25.

[8] See reference [156], section 2.3.10, page 41.
[9] See reference [156], equation 2.3.66, page 36.

Ubachs and Meyer (UM). The matrix element given in equation 3 of (UM) is diagonal in J; in this case, equation A.26 differs by a phase,

$$ME_{\mathrm{H}}^{\mathrm{UM}} = (-1)^{2F_1+2I_{\mathrm{F}}} ME_{\mathrm{H}}. \tag{A.32}$$

For the singlet case $ME_{\mathrm{H}}^{\mathrm{UM}} = ME_{\mathrm{H}}$ necessarily.

A.2 The transition dipole moment

The interaction Hamiltonian is given by

$$\hat{\mathcal{H}}_{\mathrm{I}} = -T^1(\mathbf{d}) \cdot T^1(\mathbf{E}). \tag{A.33}$$

For linearly polarized light and a quantization axis, $\hat{\mathbf{z}}$, chosen to be parallel with the optical polarization,

$$\hat{\mathcal{H}}_{\mathrm{I}} = -T_0^1(\mathbf{d}) T_0^1(\mathbf{E}). \tag{A.34}$$

This leads to a matrix element,

$$\langle \Psi' | \hat{\mathcal{H}}_{\mathrm{I}} | \Psi \rangle = -\langle \gamma' \, \Lambda' \, S \, \Sigma \, J' \, I_{\mathrm{F}} \, F_1' \, I_{\mathrm{H}} \, F' \, M_F' | T_0^1(\mathbf{d}) | \gamma \, \Lambda \, S \, \Sigma \, J \, I_{\mathrm{F}} \, F_1 \, I_{\mathrm{H}} \, F \, M_F \rangle T_0^1(\mathbf{E}). \tag{A.35}$$

Applying the Wigner–Eckart theorem to factor out the angular dependence of the

matrix element, we have,

$$\langle \Psi' | \hat{\mathcal{H}}_{\rm I} | \Psi \rangle = (-1)^{F'-M'_F+1} \begin{pmatrix} F' & 1 & F \\ -M'_F & 0 & M_F \end{pmatrix} \times \langle \gamma' \, \Lambda' \, S \, \Sigma \, J' \, I_{\rm F} \, F'_1 \, I_{\rm H} \, F' \| T^1_0(\mathbf{d}) \| \gamma \, \Lambda \, S \, \Sigma \, J \, I_{\rm F} \, F_1 \, I_{\rm H} \, F \rangle T^1_0(\mathbf{E}). \quad \text{(A.36)}$$

Factoring out the dependence on the 'outermost' angular momentum, gives,

$$\langle \Psi' | \hat{\mathcal{H}}_{\rm I} | \Psi \rangle = (-1)^{F+F'+F'_1+I_{\rm H}-M'_F} \sqrt{(2F+1)(2F'+1)} \begin{pmatrix} F' & 1 & F \\ -M'_F & 0 & M_F \end{pmatrix} \begin{Bmatrix} F'_1 & F' & I_{\rm H} \\ F & F_1 & 1 \end{Bmatrix} \times \langle \gamma' \, \Lambda' \, S \, \Sigma \, J' \, I_{\rm F} \, F'_1 \| T^1_0(\mathbf{d}) \| \gamma \, \Lambda \, S \, \Sigma \, J \, I_{\rm F} \, F_1 \rangle T^1_0(\mathbf{E}). \quad \text{(A.37)}$$

The process is repeated, factoring the remaining dependence on the initial and final hyperfine state out of the reduced matrix element,

$$\langle \Psi' | \hat{\mathcal{H}}_{\rm I} | \Psi \rangle = (-1)^{F+F'+F_1+F'_1+J'-M'_F} \sqrt{(2F+1)(2F'+1)(2F_1+1)(2F'_1+1)} \times \begin{pmatrix} F' & 1 & F \\ -M'_F & 0 & M_F \end{pmatrix} \begin{Bmatrix} F'_1 & F' & I_{\rm H} \\ F & F_1 & 1 \end{Bmatrix} \begin{Bmatrix} J' & F'_1 & I_{\rm F} \\ F_1 & J & 1 \end{Bmatrix} \times \langle \gamma' \, \Lambda' \, S \, \Sigma \, J' \| T^1_0(\mathbf{d}) \| \gamma \, \Lambda \, S \, \Sigma \, J \rangle T^1_0(\mathbf{E}). \quad \text{(A.38)}$$

The *relative* intensity, S, for hyperfine transitions within a ro-vibronic line under

the absorption of linearly polarized light is thus given by,

$$\begin{aligned} S =& (2F+1)(2F'+1)(2F_1+1)(2F_1'+1) \\ &\times \left[\begin{pmatrix} F' & 1 & F \\ -M_F' & 0 & M_F \end{pmatrix} \begin{Bmatrix} F' & F_1' & I_{\mathrm{H}} \\ F_1 & F & 1 \end{Bmatrix} \begin{Bmatrix} F_1' & J' & I_{\mathrm{F}} \\ J & F_1 & 1 \end{Bmatrix} \right]^2 . \end{aligned} \tag{A.39}$$

Appendix B

Ionic–Covalent Coupling Calculations – Tables

The matrix elements of the diabatic Hamiltonian between the ion-pair and covalent states calculated in chapter 4 are listed in the tables below. The values are all given in Hartrees in abbreviated scientific notation with the mantissa first, followed by the exponent in brackets.

B.1 Alkali-halides

The comparison of values for alkali-halide systems shown in with the earlier values of Grice and Herschbach [91, 101] used the splitting of the adiabatic potential energy curves in place of $H_{\rm ic}$. For alkali-halide systems, the parameter $|\langle\psi_{\rm i}|\psi_{\rm c}\rangle|^2$ is close to unity, and hence $\Delta V(R_{\rm c}) \approx 2H_{\rm ic}$.

Table B.1 lists all coupling energies fores, $H_{\rm ic}$, for collision of a ground-state alkali (donor) with a ground-state halogen (acceptor).

Table B.1: Calculated alkali-halide diabatic coupling energies, $H_{\rm ic}$, for the reaction M+X $\rightarrow$ M^++X^- for $M \equiv \{Li, Na, K, Rb, Cs\}$ and $X \equiv \{F, Cl, Br, I\}$.

A	F^-	Cl^-	Br^-	I^-
Li^+	6.801(-4)	7.770(-4)	2.831(-3)	9.702(-3)
Na^+	2.449(-4)	2.249(-4)	1.148(-3)	5.110(-3)
K^+	2.917(-7)	1.955(-8)	3.428(-6)	1.410(-4)
Rb^+	3.541(-8)	2.812(-10)	5.073(-7)	5.619(-5)
Cs^+	6.527(-13)	4.591(-21)	8.063(-11)	1.183(-6)

B.2 Alkali–alkali

The ionic–covalent coupling energies fores for alkali–alkali systems are listed in tables B.2–B.6, one for each *donor* atom, with each row representing a different $n\ell$ state of the donor, and each column representing a different *acceptor*.

Table B.2: Calculated diabatic coupling energies for the reaction $\mathrm{Li}(n\ell)+\mathrm{M} \rightarrow \mathrm{Li}^+ + \mathrm{M}^-$ for $\mathrm{M} \equiv \{\mathrm{Li}, \mathrm{Na}, \mathrm{K}, \mathrm{Rb}\}$.

$n\ell$	Li^-	Na^-	K^-	Rb^-
2s	3.030(-1)	3.104(-1)	3.029(-1)	2.956(-1)
2p	1.091(-1)	1.137(-1)	1.081(-1)	1.038(-1)
3s	2.577(-2)	3.297(-2)	4.394(-2)	4.774(-2)
3p	8.335(-3)	1.323(-2)	2.030(-2)	2.294(-2)
3d	4.399(-3)	7.297(-3)	1.116(-2)	1.260(-2)
4s	4.875(-5)	2.868(-4)	9.826(-4)	1.407(-3)
4p	6.347(-8)	5.997(-6)	6.926(-5)	1.419(-4)
4d	1.223(-8)	2.255(-6)	3.281(-5)	7.351(-5)
4f	5.568(-9)	1.070(-6)	1.543(-5)	3.323(-5)
5s	5.545(-95)	4.037(-21)	1.790(-12)	1.758(-10)

Table B.3: Calculated diabatic coupling energies for the reaction $\mathrm{Na}(n\ell)+\mathrm{M} \rightarrow \mathrm{Na}^+ + \mathrm{M}^-$ for $\mathrm{M} \equiv \{\mathrm{Li}, \mathrm{Na}, \mathrm{K}, \mathrm{Rb}\}$.

$n\ell$	Li^-	Na^-	K^-	Rb^-
3s	2.826(-1)	2.912(-1)	2.885(-1)	2.832(-1)
3p	8.784(-2)	9.509(-2)	9.775(-2)	9.684(-2)
4s	2.212(-2)	2.888(-2)	3.920(-2)	4.282(-2)
3d	4.568(-3)	7.512(-3)	1.141(-2)	1.285(-2)
4p	3.428(-3)	6.571(-3)	1.157(-2)	1.358(-2)
5s	2.526(-5)	1.856(-4)	7.153(-4)	1.057(-3)
4d	1.757(-8)	2.706(-6)	3.737(-5)	8.139(-5)
4f	5.909(-9)	1.104(-6)	1.577(-5)	3.392(-5)
5p	2.193(-11)	1.528(-7)	6.521(-6)	2.057(-5)
6s	1.335(-215)	4.367(-25)	5.251(-14)	1.185(-11)

Table B.4: Calculated diabatic coupling energies for the reaction K($n\ell$)+M → K^++M^- for M ≡ {Li, Na, K, Rb}.

$n\ell$	Li^-	Na^-	K^-	Rb^-
4s	2.130(-1)	2.243(-1)	2.335(-1)	2.337(-1)
4p	7.146(-2)	7.975(-2)	8.627(-2)	8.713(-2)
5s	1.254(-2)	1.783(-2)	2.597(-2)	2.897(-2)
3d	7.597(-3)	1.113(-2)	1.538(-2)	1.681(-2)
5p	1.511(-3)	3.526(-3)	7.069(-3)	8.602(-3)
4d	2.182(-6)	4.097(-5)	2.411(-4)	3.907(-4)
6s	1.604(-6)	3.308(-5)	2.062(-4)	3.546(-4)
4f	7.146(-9)	1.218(-6)	1.682(-5)	3.608(-5)
6p	1.907(-16)	2.125(-9)	5.913(-7)	3.164(-6)
5d	6.454(-118)	1.812(-42)	3.460(-19)	1.896(-15)

Table B.5: Calculated diabatic coupling energies for the reaction Rb($n\ell$)+M → Rb^++M^- for M ≡ {Li, Na, K, Rb}.

$n\ell$	Li^-	Na^-	K^-	Rb^-
5s	1.984(-1)	2.087(-1)	2.180(-1)	2.186(-1)
5p	6.439(-2)	7.294(-2)	8.068(-2)	8.214(-2)
4d	9.929(-3)	1.371(-2)	1.793(-2)	1.926(-2)
6s	1.091(-2)	1.589(-2)	2.352(-2)	2.637(-2)
6p	9.855(-4)	2.570(-3)	5.520(-3)	6.846(-3)
5d	1.087(-5)	1.105(-4)	4.798(-4)	7.178(-4)
7s	6.125(-7)	1.892(-5)	1.381(-4)	2.516(-4)
4f	8.383(-9)	1.322(-6)	1.778(-5)	3.804(-5)
7p	4.295(-20)	1.396(-10)	1.496(-7)	1.136(-6)
6d	×	1.537(-28)	3.655(-15)	1.679(-12)

Table B.6: Calculated diabatic coupling energies for the reaction Cs($n\ell$)+M → Cs^++M^- for M ≡ {Li, Na, K, Rb}.

$n\ell$	Li^-	Na^-	K^-	Rb^-
6s	1.724(-1)	1.842(-1)	1.974(-1)	1.996(-1)
6p	5.802(-2)	6.680(-2)	7.555(-2)	7.754(-2)
5d	1.352(-2)	1.674(-2)	1.956(-2)	2.020(-2)
7s	7.735(-3)	1.196(-2)	1.856(-2)	2.111(-2)
7p	5.809(-4)	1.752(-3)	4.106(-3)	5.214(-3)
6d	9.827(-5)	4.581(-4)	1.362(-3)	1.820(-3)
8s	8.254(-8)	5.997(-6)	6.302(-5)	1.273(-4)
4f	1.166(-8)	1.567(-6)	2.004(-5)	4.248(-5)
8p	3.194(-26)	2.650(-12)	2.085(-8)	2.614(-7)
7d	2.156(-51)	4.308(-17)	1.039(-10)	4.257(-9)

Table B.7: Calculated adiabatic curve splittings for the reaction $\mathrm{Li}(n\ell)+\mathrm{M} \rightarrow \mathrm{Li}^+ + \mathrm{M}^-$ for $\mathrm{M} \equiv \{\mathrm{Li}, \mathrm{Na}, \mathrm{K}, \mathrm{Rb}\}$.

$n\ell$	Li^-	Na^-	K^-	Rb^-
2s	2.041(-1)	2.093(-1)	1.845(-1)	1.677(-1)
2p	4.906(-2)	5.059(-2)	4.764(-2)	4.524(-2)
3s	8.616(-3)	1.037(-2)	1.403(-2)	1.532(-2)
3p	3.381(-3)	5.055(-3)	7.999(-3)	9.131(-3)
3d	1.887(-3)	2.969(-3)	4.674(-3)	5.330(-3)
4s	2.487(-5)	1.293(-4)	4.408(-4)	6.316(-4)
4p	4.275(-8)	3.354(-6)	3.772(-5)	7.802(-5)
4d	8.613(-9)	1.327(-6)	1.825(-5)	4.458(-5)
4f	3.989(-9)	6.387(-7)	8.437(-6)	1.898(-5)
5s	4.011(-96)	1.221(-21)	8.861(-13)	1.037(-10)

Table B.8: Calculated adiabatic curve splittings for the reaction $\mathrm{Na}(n\ell)+\mathrm{M} \rightarrow \mathrm{Na}^+ + \mathrm{M}^-$ for $\mathrm{M} \equiv \{\mathrm{Li}, \mathrm{Na}, \mathrm{K}, \mathrm{Rb}\}$.

$n\ell$	Li^-	Na^-	K^-	Rb^-
3s	1.829(-1)	1.904(-1)	1.763(-1)	1.632(-1)
3p	3.924(-2)	4.241(-2)	4.456(-2)	4.413(-2)
4s	7.476(-3)	9.151(-3)	1.256(-2)	1.377(-2)
3d	1.956(-3)	3.053(-3)	4.775(-3)	5.434(-3)
4p	1.448(-3)	2.565(-3)	4.593(-3)	5.412(-3)
5s	1.320(-5)	8.503(-5)	3.315(-4)	4.879(-4)
4d	1.231(-8)	1.563(-6)	2.090(-5)	4.889(-5)
4f	4.228(-9)	6.583(-7)	8.605(-6)	1.943(-5)
5p	1.314(-11)	1.009(-7)	4.121(-6)	1.344(-5)
6s	4.276(-217)	1.110(-25)	2.317(-14)	6.293(-12)

Table B.9: Calculated adiabatic curve splittings for the reaction $\mathrm{K}(n\ell)+\mathrm{M} \rightarrow \mathrm{K}^+ + \mathrm{M}^-$ for $\mathrm{M} \equiv \{\mathrm{Li}, \mathrm{Na}, \mathrm{K}, \mathrm{Rb}\}$.

$n\ell$	Li^-	Na^-	K^-	Rb^-
4s	1.162(-1)	1.254(-1)	1.350(-1)	1.329(-1)
4p	3.123(-2)	3.487(-2)	3.932(-2)	3.999(-2)
5s	4.473(-3)	5.908(-3)	8.635(-3)	9.640(-3)
3d	3.169(-3)	4.459(-3)	6.357(-3)	7.032(-3)
5p	6.653(-4)	1.415(-3)	2.867(-3)	3.485(-3)
4d	1.273(-6)	2.038(-5)	1.226(-4)	1.984(-4)
6s	9.383(-7)	1.660(-5)	1.039(-4)	1.818(-4)
4f	5.103(-9)	7.231(-7)	9.142(-6)	2.092(-5)
6p	8.002(-17)	1.373(-9)	4.170(-7)	2.356(-6)
5d	4.706(-116)	2.714(-43)	1.112(-19)	7.593(-16)

Table B.10: Calculated adiabatic curve splittings for the reaction $Rb(n\ell)+M \rightarrow Rb^+ + M^-$ for $M \equiv \{Li, Na, K, Rb\}$.

$n\ell$	Li^-	Na^-	K^-	Rb^-
5s	5.425(-2)	5.412(-2)	5.187(-2)	4.792(-2)
5p	2.781(-2)	3.150(-2)	3.657(-2)	3.760(-2)
4d	4.079(-3)	5.436(-3)	7.349(-3)	7.985(-3)
6s	3.833(-3)	5.166(-3)	7.665(-3)	8.594(-3)
6p	4.436(-4)	1.048(-3)	2.269(-3)	2.807(-3)
5d	6.075(-6)	5.382(-5)	2.292(-4)	3.417(-4)
7s	3.742(-7)	9.937(-6)	7.026(-5)	1.315(-4)
4f	5.971(-9)	7.809(-7)	9.642(-6)	2.231(-5)
7p	1.470(-20)	8.232(-11)	1.079(-7)	8.939(-7)
6d	×	3.426(-29)	1.486(-15)	8.299(-13)

Table B.11: Calculated adiabatic curve splittings for the reaction $Cs(n\ell)+M \rightarrow Cs^+ + M^-$ for $M \equiv \{Li, Na, K, Rb\}$.

$n\ell$	Li^-	Na^-	K^-	Rb^-
6s	7.808(-2)	8.488(-2)	9.680(-2)	9.792(-2)
6p	2.423(-2)	2.786(-2)	3.328(-2)	3.459(-2)
5d	5.633(-3)	6.789(-3)	8.146(-3)	8.488(-3)
7s	2.891(-3)	4.130(-3)	6.425(-3)	7.306(-3)
7p	2.673(-4)	7.265(-4)	1.713(-3)	2.166(-3)
6d	5.009(-5)	2.096(-4)	6.436(-4)	8.423(-4)
8s	5.414(-8)	3.293(-6)	3.405(-5)	6.922(-5)
4f	8.239(-9)	9.118(-7)	1.086(-5)	2.536(-5)
8p	8.350(-27)	1.363(-12)	1.444(-8)	2.055(-7)
7d	2.896(-52)	1.625(-17)	6.004(-11)	2.898(-9)

Appendix C

Polarimeter Code

C.1 Mathematica calibration code

```
t0 = TimeUsed[];                    (* Begin timing *)

n = 50;                             (* 50 retarder angles*)
beta = Table[i*2 pi/n, {i, n}];     (* Create vector of retarder angles*)

imax = 8;                           (* Use 8 search iterations *)

nbeta0 = 11;                        (* 11 trial values for each parameter *)
ngamma = 11;
nDelta = 11;
nphi = 11;

Deltaguess = {550/670, 645/670, 1}*pi/2.;   (* lambda_nom for each retarder *)
phiguess = {-3.6 Degree, 0, 3.6 Degree};    (* phi_nom *)

data = {};                          (* Empty matrix to store output *)
Do[

 beta0cent = 0;                     (* Central values and grid spacings *)
 dbeta0 = 0.02;                     (* - updated on each iteration - *)

 gammacent = 15/100*2 pi + pi/2.;
 dgamma = 0.02;
```

```
Deltacent = Deltaguess[[j]];
dDelta = 0.02;

phicent = phiguess[[k]];
dphi = 0.02;

                                    (* Define Fourier coeffs *)
a0[Ii_] := 2/Length[Ii] Sum[Ii[[i]], {i, Length[Ii]}];
a2[Ii_, betai_] :=
 4/Length[Ii] Sum[Ii[[i]] Cos[2 betai[[i]]], {i, Length[Ii]}];
b2[Ii_, betai_] :=
 4/Length[Ii] Sum[Ii[[i]] Sin[2 betai[[i]]], {i, Length[Ii]}];
a4[Ii_, betai_] :=
 4/Length[Ii] Sum[Ii[[i]] Cos [4 betai[[i]]], {i, Length[Ii]}];
b4[Ii_, betai_] :=
 4/Length[Ii] Sum[Ii[[i]] Sin [4 betai[[i]]], {i, Length[Ii]}];

                                    (* Calculate Fourier coeffs - 4 cases *)
a0list = Table[a0[volts[[k, j, i]]], {i, 4}];
a2list = Table[a2[volts[[k, j, i]], beta], {i, 4}];
b2list = Table[b2[volts[[k, j, i]], beta], {i, 4}];
a4list = Table[a4[volts[[k, j, i]], beta], {i, 4}];
b4list = Table[b4[volts[[k, j, i]], beta], {i, 4}];

Do[

 results =                          (* Results matrix for single iteration *)
  Table[0, {i, nbeta0*ngamma*nDelta*nphi}];

 q = 0;
 Do[q = q + 1;

  (* Stokes and poln - case 1 *)
  S0c1 =
   a0list[[1]] - (1 + Cos[Delta])/(
     1 - Cos[Delta]) (a4list[[1]] Cos[
         4 (gamma - beta0)] +
      b4list[[1]] Sin[4 (gamma - beta0)]);
  S1c1 =
   2/(1 - Cos[Delta]) (a4list[[1]] Cos[
        2 (gamma - 2 beta0)] +
     b4list[[1]] Sin[2 (gamma - 2 beta0)]);
  S2c1 =
   2/(1 - Cos[Delta]) (b4list[[1]] Cos[
        2 (gamma - 2 beta0)] -
     a4list[[1]] Sin[2 (gamma - 2 beta0)]);
  S3c1 = Sqrt[a2list[[1]]^2 + b2list[[1]]^2]/Sin[Delta];
  {S0c1, S1c1, S2c1, S3c1} = {S0c1, S1c1, S2c1, S3c1}/S0c1;
```

```
P1 = Sqrt[S1c1^2 + S2c1^2 + S3c1^2];

(* Stokes and poln - case 2 *)
S0c2 =
 a0list[[2]] - (1 + Cos[Delta])/(
   1 - Cos[Delta]) (a4list[[2]] Cos[
       4 (gamma + beta0 - 2 phi)] +
     b4list[[2]] Sin[4 (gamma + beta0 - 2 phi)]);
S1c2 =
 2/(1 - Cos[Delta]) (a4list[[2]] Cos[
      2 (gamma + 2 beta0 - 4 phi)] +
    b4list[[2]] Sin[2 (gamma + 2 beta0 - 4 phi)]);
S2c2 =
 2/(1 - Cos[Delta]) (b4list[[2]] Cos[
      2 (gamma + 2 beta0 - 4 phi)] -
    a4list[[2]] Sin[2 (gamma + 2 beta0 - 4 phi)]);
S3c2 = Sqrt[a2list[[2]]^2 + b2list[[2]]^2]/Sin[Delta];
{S0c2, S1c2, S2c2, S3c2} = {S0c2, S1c2, S2c2, S3c2}/S0c2;
P2 = Sqrt[S1c2^2 + S2c2^2 + S3c2^2];

(* Stokes and poln - case 3 *)
S0c3 =
 a0list[[3]] - (1 + Cos[Delta])/(
   1 - Cos[Delta]) (a4list[[3]] Cos[
       4 (gamma + beta0)] -
     b4list[[3]] Sin[4 (gamma + beta0)]);
S1c3 =
 2/(1 - Cos[Delta]) (a4list[[3]] Cos[
      2 (gamma + 2 beta0)] -
    b4list[[3]] Sin[2 (gamma + 2 beta0)]);
S2c3 =
 2/(1 - Cos[Delta]) (b4list[[3]] Cos[
      2 (gamma + 2 beta0)] +
    a4list[[3]] Sin[2 (gamma + 2 beta0)]);
S3c3 = Sqrt[a2list[[3]]^2 + b2list[[3]]^2]/Sin[Delta];
{S0c3, S1c3, S2c3, S3c3} = {S0c3, S1c3, S2c3, S3c3}/S0c3;
P3 = Sqrt[S1c3^2 + S2c3^2 + S3c3^2];

(* Stokes and poln - case 4 *)
S0c4 =
 a0list[[4]] - (1 + Cos[Delta])/(
   1 - Cos[Delta]) (a4list[[4]] Cos[
       4 (gamma - beta0 + 2 phi)] -
     b4list[[4]] Sin[4 (gamma - beta0 + 2 phi)]);
S1c4 =
 2/(1 - Cos[Delta]) (a4list[[4]] Cos[
      2 (gamma - 2 beta0 + 4 phi)] -
    b4list[[4]] Sin[2 (gamma - 2 beta0 + 4 phi)]);
```

```
  S2c4 =
   2/(1 - Cos[Delta]) (b4list[[4]] Cos[
        2 (gamma - 2 beta0 + 4 phi)] +
      a4list[[4]] Sin[2 (gamma - 2 beta0 + 4 phi)]);
  S3c4 = Sqrt[a2list[[4]]^2 + b2list[[4]]^2]/Sin[Delta];
  {S0c4, S1c4, S2c4, S3c4} = {S0c4, S1c4, S2c4, S3c4}/S0c4;
  P4 = Sqrt[S1c4^2 + S2c4^2 + S3c4^2];

  (* Calculate error (xi) *)
  avgS1 = (S1c1 + S1c2 + S1c3 + S1c4)/4;
  avgS2 = (S2c1 + S2c2 + S2c3 + S2c4)/4;
  diffS1 = (S1c1 - avgS1)^2 + (S1c2 - avgS1)^2
         + (S1c3 - avgS1)^2 + (S1c4 - avgS1)^2;
  diffS2 = (S2c1 - avgS2)^2 + (S2c2 - avgS2)^2
         + (S2c3 - avgS2)^2 + (S2c4 - avgS2)^2;
  error = diffS1 + diffS2 + (1-P1)^2 + (1-P2)^2 + (1-P3)^2 + (1-P4)^2;

  (* Store current values in results matrix *)
  results[[q]] = {beta0, gamma, Delta, phi, error};

  (* 4D search limits *)
  , {gamma, gammacent - (ngamma - 1)/2*dgamma,
            gammacent + (ngamma - 1)/2*dgamma, dgamma}
  , {Delta, Deltacent - (nDelta - 1)/2*dDelta,
            Deltacent + (nDelta - 1)/2*dDelta, dDelta}
  , {beta0, beta0cent - (nbeta0 - 1)/2*dbeta0,
            beta0cent + (nbeta0 - 1)/2*dbeta0, dbeta0}
  , {phi, phicent - (nphi - 1)/2*dphi,
          phicent + (nphi - 1)/2*dphi, dphi}];

  (* Redefine central values to current optimum *)
  {beta0cent, gammacent, Deltacent, phicent} =
   results[[Ordering[results[[All, 5]]]]][[1, 1 ;; 4]];

  (* Halve search grid spacings *)
  {dbeta0, dgamma, dDelta, dphi} = {dbeta0, dgamma, dDelta, dphi}/2;

  (* Print current optimum values *)
  Print[results[[Ordering[results[[All, 5]]]]][[1]]];

 , {i, imax}];                    (* Advance to next iteration *)

(* Store final optimum values for current waveplate/alignment *)
dataresc = Join[dataresc, {results[[Ordering[results[[All, 5]]]]][[1]]}];
Print["-----"];
Print[TableForm[{results[[Ordering[results[[All, 5]]]]][[1]]}]];
Print["-----"];
```

```
 , {j, 3}, {k, 3}]                  (* Advance to next waveplate/alignment *)

Print["Time used = ", TimeUsed[] - t0, " s"]
```

C.2 Polarimeter microcontroller assembly code

```
Title "ADC_PIC18F2320"
;;;;;;;;;;;;;;;;;;;;;;;;;;;;;;;;;;;;;;;;;;;;;;;;;;;;;;;;;;;;
;;                                                        ;;
;;  Taking 50 datapoints, long pause for voltage reading  ;;
;;              Longer A/D acquisition time               ;;
;;                                                        ;;
;;;;;;;;;;;;;;;;;;;;;;;;;;;;;;;;;;;;;;;;;;;;;;;;;;;;;;;;;;;;
;Define Configuration Settings
 __CONFIG 0x300001, b'00001001'      ;Internal External Switch Over mode disabled
                                     ;Fail-Safe Clock Monitor disabled
                                     ;Int osc, CLKO on RA6, PORT fn on RA7
 __CONFIG 0x300002, b'00000000'      ;Power-up Timer enabled (18LF2320)
                                     ;Brown-out reset disabled, brn-out = 4.5V
 __CONFIG 0x300003, b'00000000'      ;Watchdog Timer disabled - Postscale bits 1:1
 __CONFIG 0x300005, b'10000001'      ;Not Masterclear pin enabled
                                     ;PORTB<4:0> pins are configured as dig I/O
                                     ;CCP2 input/output is multiplexed with RC1
 __CONFIG 0x300006, b'10000000'      ;Debugger disabled - RB6 and RB7 are I/O pins
                                     ;Low-voltage ICSP disabled
                                     ;Stack overflow will not cause reset
 __CONFIG 0x300008, b'00001111'      ;No code protection for CP0-CP3
 __CONFIG 0x300009, b'11000000'      ;Data EEPROM not code-protected
                                     ;Boot block not code-protected
 __CONFIG 0x30000A, b'00001111'      ;No write protection for WRT0-WRT3
 __CONFIG 0x30000B, b'11100000'      ;Data EEPROM not write-protected
                                     ;Boot block not write-protected
                                     ;Configuration registers not write-protected
 __CONFIG 0x30000C, b'00001111'      ;No table read protection for EBTR0-EBTR3
 __CONFIG 0x30000D, b'01000000'      ;Boot block not protected from table reads

;Define Registers
TRISA       EQU             0x92
TRISB       EQU             0x93
TRISC       EQU             0x94
PORTA       EQU             0x80
PORTB       EQU             0x81
PORTC       EQU             0x82
```

```
OSCCON      EQU             0xD3

FSR0        EQU             0x00
POSTINC0    EQU             0xEE
FSR1        EQU             0x01
POSTINC1    EQU             0xE6

ADRESH      EQU             0xC4
ADRESL      EQU             0xC3
ADCON0      EQU             0xC2
ADCON1      EQU             0xC1
ADCON2      EQU             0xC0

SPBRG       EQU             0xAF
RCREG       EQU             0xAE
TXREG       EQU             0xAD
TXSTA       EQU             0xAC
RCSTA       EQU             0xAB
PIR1        EQU             0x9E

DATA1       EQU             0x21
DATA2       EQU             0x22
DCOUNT      EQU             0x23
SCOUNT1     EQU             0x24
SCOUNT2     EQU             0x25
TCOUNT      EQU             0x26

DELAY1      EQU             0x27
DELAY2      EQU             0x28
DELAY3      EQU             0x29

GO_DONE     EQU             1
ADON        EQU             0

;Define bits within PIR1 register:
RCIF        EQU             5
TXIF        EQU             4

;Define bits within RCSTA and TXSTA registers:
CREN        EQU             4           ;Disables/Enables receiver
TXEN        EQU             5           ;Transmit disabled/enabled

; Assign auxillary values
A           EQU             0           ;when a=0, access bank is used

;;;;;;;;;;;;;;;;;
; Start Program ;
;;;;;;;;;;;;;;;;;
```

```
            ORG 0x00

            BSF             OSCCON, 4, A            ;Internal oscillator -> 8 MHz
            BSF             OSCCON, 5, A
            BSF             OSCCON, 6, A

            CALL            SHORTDELAY

            MOVLW           B'11111111'
            MOVWF           TRISA, A                ;Set PORTA pins as inputs
            MOVLW           B'11111110'
            MOVWF           TRISB, A                ;Set PORTB pin0 as output
            MOVLW           B'10111110'
            MOVWF           TRISC, A                ;Set PORTC pins0,6 as outputs

;;;;;;;;;;;;;;;;;;;;;;;;;;;;
; Initialize RS-232 module ;
;;;;;;;;;;;;;;;;;;;;;;;;;;;;

            MOVLW           B'00000100'
            MOVWF           TXSTA, A                ;8bit, transmit disabled
                                                    ;Asynchronous mode
                                                    ;TransShiftReg status-bit=empt

            MOVLW           B'10000000'
            MOVWF           RCSTA, A                ;Enab serial port, 8bit recptn
                                                    ;Receiver disabled
                                                    ;No framing or overrun error
            BSF             TXSTA, 2, A
            MOVLW           D'51'
            MOVWF           SPBRG, A                ;Set the baud rate generator
                                                    ;(8MHz clk, 9600k, high speed)

            BSF             RCSTA, CREN, A          ;Enable Receiver
            BSF             TXSTA, TXEN, A          ;Enable Transmitter

;;;;;;;;;;;;;
; Take data ;
;;;;;;;;;;;;;

RECWAIT     BTFSS           PIR1, RCIF, A           ;Receipt complete? If so, skip
            GOTO            RECWAIT

            MOVF            RCREG, 0, A             ;Read RCREG to clear RCIF

            MOVLW           D'50'
            MOVWF           DCOUNT, A               ;Data count
```

```
            LFSR        FSR0, 0x100
            LFSR        FSR1, 0x170

            CALL        ANALOG0             ;Take zero-point reading

            MOVF        DATA1, 0, A         ;Store, indirect addressing
            MOVWF       POSTINC0, A
            MOVF        DATA2, 0, A
            MOVWF       POSTINC0, A

            CALL        ANALOG1             ;Take zero-point reading

            MOVF        DATA1, 0, A         ;Store, indirect addressing
            MOVWF       POSTINC1, A
            MOVF        DATA2, 0, A
            MOVWF       POSTINC1, A

DSTART      MOVLW       D'100'              ;400*1.8deg between readings
            MOVWF       SCOUNT1, A          ;=> 2*3.6deg steps of lambda/4

CYCLE       BCF         PORTC, 0, A         ;Rotate lambda/4
            CALL        SHORTDELAY
            BCF         PORTB, 0, A
            CALL        SHORTDELAY
            BSF         PORTC, 0, A
            CALL        SHORTDELAY
            BSF         PORTB, 0, A
            CALL        SHORTDELAY
            DECFSZ      SCOUNT1, 1, A
            GOTO        CYCLE

            CALL        LONGDELAY

            CALL        ANALOG0             ;Read power-meter

            MOVF        DATA1, 0, A         ;Store, indirect addressing
            MOVWF       POSTINC0, A
            MOVF        DATA2, 0, A
            MOVWF       POSTINC0, A

            CALL        ANALOG1             ;Read power-meter

            MOVF        DATA1, 0, A         ;Store, indirect addressing
            MOVWF       POSTINC1, A
            MOVF        DATA2, 0, A
            MOVWF       POSTINC1, A

            DECFSZ      DCOUNT, 1, A
```

```
            GOTO            DSTART

;;;;;;;;;;;;;;;;;
; Transmit data ;
;;;;;;;;;;;;;;;;;

            MOVLW           D'102'                  ;Must be 2*DCOUNT
            MOVWF           TCOUNT, A               ;Transmit counter
            LFSR            FSR0, 0x100

READ0       MOVF            POSTINC0, 0, A
            MOVWF           TXREG, A                ;Transmit data

TRANSWAIT0  BTFSS           PIR1, TXIF, A           ;Trans complete? If so, skip
            GOTO            TRANSWAIT0
            CALL            SHORTDELAY
            DECFSZ          TCOUNT, 1, A
            GOTO            READ0

            MOVLW           D'102'                  ;Must be 2*DCOUNT
            MOVWF           TCOUNT, A               ;Transmit counter
            LFSR            FSR1, 0x170

READ1       MOVF            POSTINC1, 0, A
            MOVWF           TXREG, A                ;Transmit data

TRANSWAIT1  BTFSS           PIR1, TXIF, A           ;Trans complete? If so, skip
            GOTO            TRANSWAIT1
            CALL            SHORTDELAY
            DECFSZ          TCOUNT, 1, A
            GOTO            READ1

            GOTO            RECWAIT

;;;;;;;;;;;;;;;;;;;;;;;;;;;;;
; A2D and delay subroutines ;
;;;;;;;;;;;;;;;;;;;;;;;;;;;;;

ANALOG0     MOVLW           B'00000111'
            MOVWF           ADCON1, A               ;Vref: AVSS and AVDD
            MOVLW           B'00000000'
            MOVWF           ADCON0, A               ;AN0 selected - A/D module off
            MOVLW           B'10111110'
            MOVWF           ADCON2, A               ;right justified, 8TAD, Fosc/4
            BSF             ADCON0, ADON, A         ;Turn on A/D module
            CALL            ADELAY                  ;Wait required acq time
            BSF             ADCON0, GO_DONE, A      ;A/D conversion in progress
ADCOV0      BTFSC           ADCON0, GO_DONE, A      ;Test to see if GO bit is DONE
```

```
            GOTO            ADCOV0
            MOVF            ADRESL, 0, A            ;Store low-byte in DATA1
            MOVWF           DATA1, A
            MOVF            ADRESH, 0, A            ;Store low-byte in DATA2
            MOVWF           DATA2, A
            RETURN

ANALOG1     MOVLW           B'00000111'
            MOVWF           ADCON1, A               ;Vref: AVSS and AVDD
            MOVLW           B'00000100'
            MOVWF           ADCON0, A               ;AN1 selected - A/D module off
            MOVLW           B'10111110'
            MOVWF           ADCON2, A               ;right justified, 8TAD, Fosc/4
            BSF             ADCON0, ADON, A         ;Turn on A/D module
            CALL            ADELAY                  ;Wait required acq time
            BSF             ADCON0, GO_DONE, A      ;A/D conversion in progress
ADCOV1      BTFSC           ADCON0, GO_DONE, A      ;Test to see if GO bit is DONE
            GOTO            ADCOV1
            MOVF            ADRESL, 0, A            ;Store low-byte in DATA1
            MOVWF           DATA1, A
            MOVF            ADRESH, 0, A            ;Store low-byte in DATA2
            MOVWF           DATA2, A
            RETURN

ADELAY      CLRF            DELAY1, A               ;~200,000 instruction cycles
            CLRF            DELAY2, A               ;=> ~100 msec for 8 MHz clock
DELAYA      DECFSZ          DELAY1, 1, A
            GOTO            DELAYA
            DECFSZ          DELAY2, 1, A
            GOTO            DELAYA
            RETURN

LONGDELAY   CLRF            DELAY1, A               ;~2,000,000 instruc cycles
            CLRF            DELAY2, A               ;=> ~1 sec for 8 MHz clock
            MOVLW           D'5'
            MOVWF           DELAY3, A
DELAYL      DECFSZ          DELAY1, 1, A
            GOTO            DELAYL
            DECFSZ          DELAY2, 1, A
            GOTO            DELAYL
            DECFSZ          DELAY3, 1, A
            GOTO            DELAYL
            RETURN

SHORTDELAY  CLRF            DELAY1, A               ;~50,000 instruction cycles
            MOVLW           D'10'                   ;=> ~25 msec for 8 MHz clock
            MOVWF           DELAY2, A
DELAYS      DECFSZ          DELAY1, 1, A
```

```
GOTO            DELAYS
DECFSZ          DELAY2, 1, A
GOTO            DELAYS
RETURN

END
```